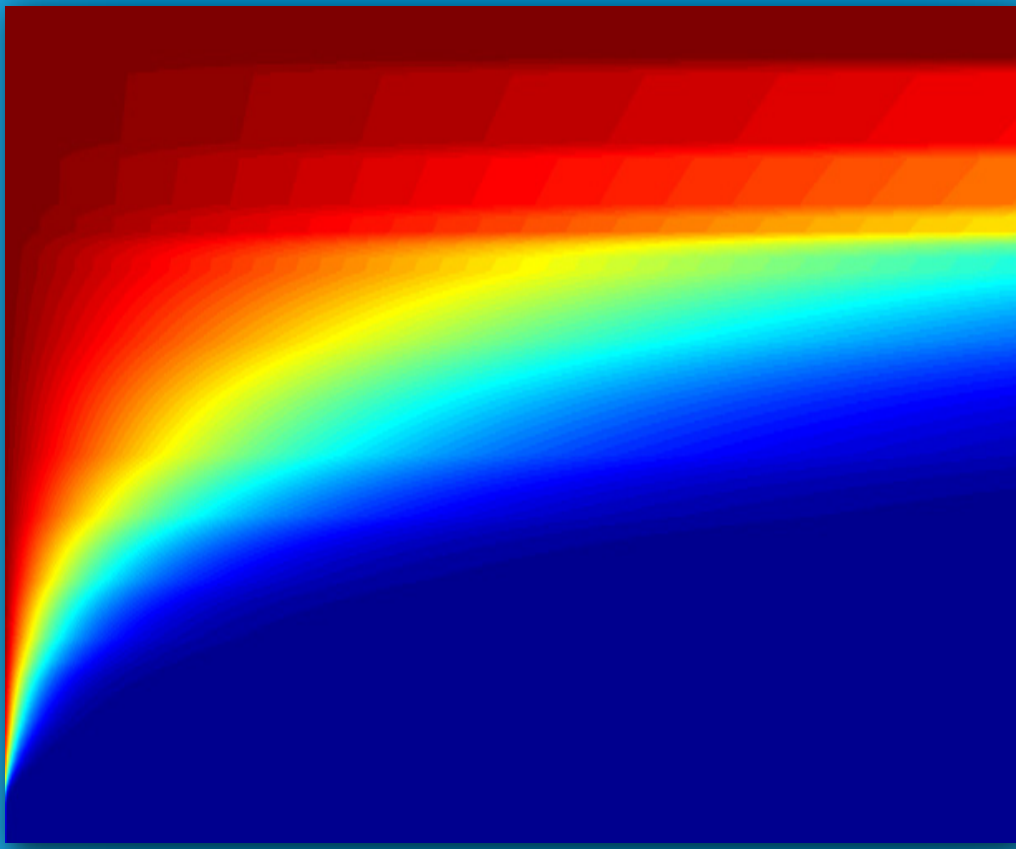


Aalborg University
Department of Physics and Nanotechnology

Fabrication and Characterization of Polycrystalline Silicon Solar Cells



Kenneth Bech Skovgaard & Kim Thomsen
Master Thesis



Department of Physics and Nanotechnology

Skjernvej 4A

9220 Aalborg Øst

Phone: +45 9940 9215

<http://www.nano.aau.dk>

Title:

Fabrication and Characterization of
Polycrystalline Silicon Solar Cells

Theme:

Master thesis

Project Period:

P9-P10 Semesters,
September 2nd, 2010 to
June 23rd, 2011

Project Group:

NFM4-5.219A

Group Members:

Kenneth Bech Skovgaard
Kim Thomsen

Supervisor:

Kjeld Pedersen

Number of Copies: 5

Number of Pages: 110

Number of Appendices: 2

Total Number of Pages: 118

Finished June 23rd 2011

Abstract

With the ongoing climate debate of trying to implement more green energy sources to reduce the CO₂ pollution of the atmosphere the field of silicon based solar cells is receiving a lot of attention. The technology is non-polluting and can rather easily be implemented at sites where the power demand is needed.

Based on this, a method for fabricating polycrystalline silicon solar cells is sought and a thorough examination of the mechanisms of converting solar energy into electrical energy is examined. The central problem statement of this thesis is thus: "How can a basic solar cell with rectifying diode behavior be fabricated, and how can the specific characteristics of the solar cell be enhanced?". Generally the thesis is separated into three parts, introductory theory, solar cell fabrication, and finally characterization of fabricated solar cells utilizing their I-V characteristics obtained.

The introductory theory provides knowledge needed to understand the physics of semiconductors and the diffusion mechanisms when a dopant is introduced to a silicon substrate. The absorption of electromagnetic radiation is also treated to investigate the optimum depth of the formation of the pn-junction from the silicon substrate surface. Furthermore a thorough examination of the limiting factors decreasing the efficiency of a solar cell is made.

Solar cells are fabricated using spin-on and a screen printing of two types of phosphorus dopants on polycrystalline substrates. To gain a working diode within the solar cell several means are necessary to avoid the solar cell from leaking current at the edges of the wafer. RIE-etching of the edges of the n-side surface layer is utilized as a means.

The phosphorus doped silicon substrate, using the spin-on method, yielded a solar cell with a maximum efficiency of 5.1%. The open circuit voltage was 0.56V and the short circuit current 46.6mA. The maximum efficiency achieved using phosphorus screen printing paste was 4.05%.

Rectifying diode behavior was found for several of the fabricated solar cells. This is seen to be an imperative feature to gain a functional solar cell.

Preface

This master's thesis is composed by group NFM4-5.219A in the 9th and 10th semesters at the Institute of Physics and Nanotechnology at Aalborg University, in the period from September 2nd 2010 to June 23rd 2011. The target audience of this thesis are of an educational level corresponding to candidat students in the field of nanophysics and -materials.

The main report consists of six theoretical chapters, 3, 4, 5, 6, 7, and 8. Chapter 3 describes the basic physical properties of electrons and holes in semiconductor bands to analyze the concept of diffusion in chapter 4, which can be utilized to determine the dopant concentration. Chapter 5 and 6 describe the statistics of a semiconductor and a thorough evaluation of the junctions formed within a solar cell. Chapter 7 and 8 concern the absorption of electromagnetic radiation in a solar cell and the limiting factors that affect the efficiency when converting solar radiation into electrical energy.

Finally chapter 9 contains the methods utilized to fabricate the silicon based solar cells and chapter 10 describes the characterization methods used in the analysis of the results in chapter 11.

References are displayed in square brackets []. References placed at the end of a section refer to the whole section, and if placed elsewhere, it refers to that specific statement. Figures without references are produced by the group itself. The notation used in the report displays vectors as \vec{A} . Abbreviations of keywords are defined in normal brackets the first time and used afterwards.

The following deserve a special thanks for their contribution to the project:

- Christian Uhrenfeldt, for guidance concerning analysis of solar cell characterization
- Pia Bomholt Jensen, for guidance concerning the fabrication of solar cells

Kenneth Bech Skovgaard

Kim Thomsen

Contents

1	Introduction	11
1.1	The photovoltaic effect	12
1.2	Plasmons	13
2	Problem Statement	15
3	Electrons and Holes in Energy Bands	17
3.1	Electron and hole motion in semiconductor bands	17
3.2	Semiconductor impurities	23
4	Diffusion	27
4.1	Fick's diffusion equation	27
4.2	Profile analysis	31
5	Semiconductor Statistics	35
5.1	Intrinsic semiconductors	35
5.2	Extrinsic semiconductors	40
6	Junctions in Semiconductors at Thermal Equilibrium	43
6.1	Space charge region	43
6.2	Charge density variation	45
6.3	Diffusion potential	46
6.4	Build-in electric field	47
6.5	Energy bands in space charge region	49
6.6	Solar cells	50
6.7	Metal-semiconductor junctions	50
7	Absorption of Electromagnetic Radiation	53

7.1	Absorption coefficient	53
7.2	Photogeneration	61
7.3	Recombination processes	63
8	Solar Cell Characteristics	67
8.1	Detailed balance	67
8.2	Characteristics of a solar cell	70
8.3	Efficiency	74
9	Solar Cell Fabrication	79
9.1	pn-junction formation	79
9.2	Contacts	82
10	Characterization Methods	85
10.1	Sheet resistance	85
10.2	Diode characterization	86
10.3	I-V characterization and cell efficiency	86
11	Results	91
11.1	Drive-in atmosphere	91
11.2	Sheet resistance vs. paste thickness	96
11.3	Contact annealing	96
11.4	RIE-etching	98
12	Perspectives	105
13	Conclusion	107
A	Electromagnetic Respons	111
A.1	Maxwell's equations	111
B	Specifics of Fabricated Solar Cells	117

Chapter 1

Introduction

In 2008 fossil fuels provided the world with 81% of the average global power consumption of 15TW. [14] The burning of fossil fuels leads to emission of CO₂, which increases the greenhouse effect. By signing the Kyoto Protocol of 1997 several countries agreed to reduce the emission of greenhouse gasses by a certain percentage before 2012. [13] Among other reasons this started the focus on production of sustainable energy e.g. by wind power, hydropower, and solar energy.

To enhance the implementation of silicon solar cells the cost per watt compared to that of fossil fuels must be lowered from \$4 to about \$1 to be competitive. [4] During the fabrication process nearly 70% of the costs lie in the processed solar cell. Therefore it is imperative to reduce the amount of material used to produce the solar cells as well as the processing costs. Furthermore the enhancement of the solar cells efficiency will yield a reduction in cost per watt.

Photovoltaic devices have insignificantly low impact on the environment compared to any other power generating technology. It does not pollute nor does it create any form of toxic waste, opposed to the burning of fossil fuels which emits CO₂. In addition once the solar panels have been deployed the photovoltaic devices do not require any hazardous materials to function. They only depend on sunlight which is costless to gain and is vastly abundant thus making this energy source very interesting.

Furthermore the application of solar cells does not require a lot of infrastructural changes in order to be deployed as opposed to e.g. wind turbines. The solar panels can to a large extent be established at buildings where the power is needed whether it is for private or commercial need. The Danish Climate Commission (DCC) has not determined a specific technology to favor and thus Dansk Solcelle Forening (DSF) recognizes the potential that lies within the field of solar cells even though biomass and wind technology receive more attention. DCC aims ambitiously to have a fossil fuel independent Denmark in the year 2050. Naturally from a Danish point of view wind and biomass will receive a lot of attention, but DSF notice that no specific technology is determined and the DCC emphasizes on flexibility and is open minded on new technologies.

Solar cell technology is mature and is capable of contributing to a fossil independent Denmark. The production of solar cells has been multiplied greatly over

the last few years and the cost has been lowered as a direct consequence - in 2009 by 30% alone. The potential of solar cells is also enhanced by the fact that the solar cell industry is growing exponentially by 40-50% a year. Therefore the solar cell industry is the industry experiencing most growth. With market demands rising the price on solar cell power is resultingly expected to be lowered combined with an extensive research in enhancing the efficiency of the solar cells. The development for solar cells looks promising giving the numbers above and arguments are for investing in the technology.[11]

Despite all the advantages of solar cells their success still relies on the fact of making them more efficient in order to compete with the present energy sources of fossil fuels. Electricity gained from solar cells is 5-10 times more costly than that from burning of fossil fuels.[12, p. 4-5] The reason is found in the relatively low efficiency of e.g. commercial cells made of silicon where a high conversion efficiency lies at around 22%.[1, p. 368]

1.1 The photovoltaic effect

The generation of electrical energy from light energy occurs due to the photovoltaic effect. Light with energies, $h\nu$, higher or equal to that of the band gap, E_g , of the material interacting, can excite an electron from the valence band to the conduction band, where the electrons are free to move. Although being free to move the electron will quickly relax to the ground state in the valence band unless a built-in electric field pulls the electron away. If separated the electrons can be fed to an external circuit, this is illustrated in figure 1.1 [9, p. 1]

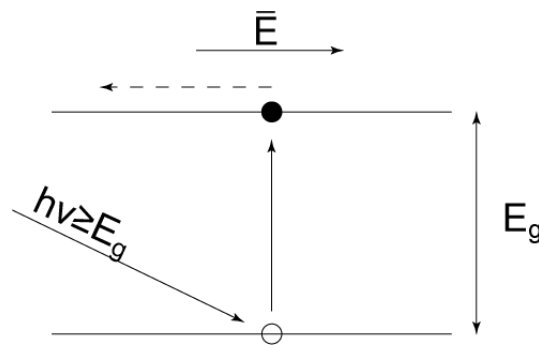


Figure 1.1: Illustrates the photovoltaic effect. Light with energy higher than the band gap energy excites an electron from the valence band to the conduction band, where it is separated from the hole left in the valence band by a built-in electric field.

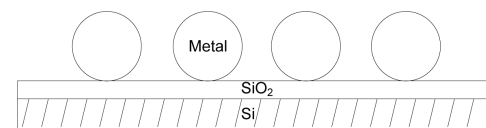
The efficiency of the solar cell depends on the material used. The optimum band gap for a solar cell material lies at 1.4eV which suggests the use of materials such as indium phosphide or gallium arsenide. Silicon, which has a band gap of 1.17eV [1, p. 68], is cheaper and more easily available giving it a definite advantage for practical applications. Cells made from cheap polycrystalline materials have shown

yields of 10% efficiency.[1, p. 368]

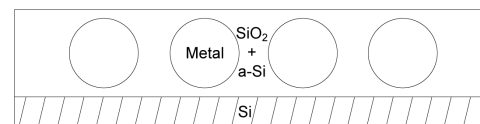
Even though silicon has a band gap of 1.17eV, this is not a direct band gap. In order for incident photons with energies lower than that of silicon's direct band gap at 3.45eV [1, p. 68] to contribute to the excitation of electrons, the light must be assisted by lattice vibrations called phonons.

1.2 Plasmons

A means to decrease the cost of silicon solar cells is to reduce the amount of silicon used. This could be done by reducing the thickness of the solar cell. However, as the thickness of the solar cell is decreased more and more light penetrates the cell and is not exploited to create electron hole pairs. In order to absorb the light which would pass through the cell at a given thickness, the path length of the light in the material is sought to be elongated by placing metal nanoparticles at the surface of the silicon solar cell, which will scatter the light due to localized surface plasmons.



(a) Nanoparticles on top of a silicon substrate.



(b) Nanoparticles embedded in SiO_2 and amorphous silicon (a-Si). Inspired from [3].

Figure 1.2: Two possible methods of using metal nanoparticles to create localized surface plasmons.

Figure 1.2 shows two possible methods of using metal nanoparticles to create localized surface plasmons. In figure 1.2(a) metal nanoparticles are placed on top of the silicon substrate with a layer of SiO_2 separating the silicon and metal. As the metal nanoparticles cannot have an oxide shell, silver and gold are suitable materials due to their inertness as well as their resonances in the visible light region. However, a disadvantage of using silver and gold in a combination with silicon is the risk of introducing metallic defects to the silicon lattice. These defects would yield mid-gap energy states which can act as undesirable recombination sites, where an electron or a hole can be captured and if not released by thermal activation the trap can capture a carrier of opposite polarity, which will complete the recombination. An example of complete electron-hole recombination is illustrated in figure 1.3.[9, p. 106-107][3]

To avoid metal induced recombination sites an electrically neutral metal such as

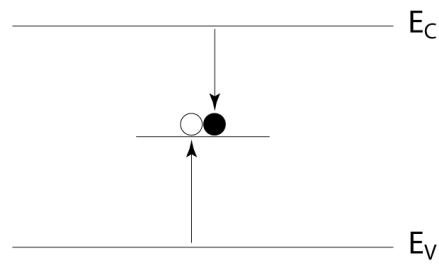


Figure 1.3: An example of complete electron-hole recombination. Inspired from [9, p. 112].

tin can be chosen. A disadvantage of using tin is its oxidation when in contact with air. This can be avoided by embedding the tin nanoparticles in a host material such as SiO_2 combined with amorphous silicon. As the Si-O bonding enthalpy is much larger than that of Sn-O, the oxidation of tin nanoparticles embedded in SiO_2 , due to oxygen inter diffusion, is not likely. This scenario is shown in figure 1.2(b).[3]

Chapter 2

Problem Statement

As mentioned in Chapter 1, solar cells' competitiveness to other energy sources is highly dependent on their efficiency. To be able to improve the efficiency of solar cells it is important to understand the influence of certain limiting factors. The focus of this thesis is to fabricate a functional solar cell using phosphorus as dopant on polycrystalline p-type silicon substrates. Furthermore the aim is to investigate the enhancement of the cell efficiency through various optimizing fabrication techniques. Based on this the following initiating problem is the foundation of the thesis:

"How can a basic solar cell with rectifying diode behavior be fabricated, and how can the specific characteristics of the solar cell be enhanced?"

Chapter 3

Electrons and Holes in Energy Bands

This chapter deals with the dynamics and kinematics of electrons and holes in energy bands. The similarity of the properties of electrons and holes are investigated. Furthermore the concept of impurities in a semiconductor crystal is described.

3.1 Electron and hole motion in semiconductor bands

Semiconductors differ from metals due to the fact that charge carriers can include not only electrons in the conduction band but also empty electron states or holes in the valence band. When an external source of applied electrical or magnetic field interacts with the current carriers the behavior is strongly dependent on the energy band structure of the semiconductor and is characterized by their effective mass and charge.[1, p.74]

The electrons in the semiconductor are described by Bloch states or waves within the regime of a periodic potential. The corresponding wave functions to the Bloch states are wave-like and non-localized. To describe electron motion from one point in the band to another it is represented by a localized wave packet in order to assign a particular coordinate at a particular time. The wave packet, also called envelope function, is created by a superposition of linear time-dependent Bloch functions of various wave vectors \vec{k} and coefficients $a_{n\vec{k}}$ with maximum at a particular value \vec{k}_0 :

$$f_{n\vec{k}_0}(\vec{r}, t) = \int d^3k a_{n\vec{k}} \Psi_{n\vec{k}}(\vec{r}, t). \quad (3.1)$$

The time dependent Bloch functions are written as

$$\Psi_{n\vec{k}}(\vec{r}, t) = e^{i\vec{k}\cdot\vec{r}} u_{n\vec{k}}(\vec{r}) e^{-i(E_{n\vec{k}}/\hbar)t}, \quad (3.2)$$

which is a product of two plane wave functions, spatial and time dependent, and a periodic Bloch function $u_{n\vec{k}}(\vec{r})$. $E_{n\vec{k}}$ is the energy eigenvalue of the Bloch state.

Due to the nature of $a_{n\vec{k}}$ \vec{k} can be written as its \vec{k}_0 value and a spread $\Delta\vec{k}$. This is utilized to expand in powers of $\Delta\vec{k}$:

$$E_{n\vec{k}} = E_{n\vec{k}_0} + \Delta\vec{k} \cdot \nabla_{\vec{k}_0} E_{n\vec{k}_0} + \dots, \quad (3.3)$$

$$u_{n\vec{k}}(\vec{r}) = u_{n\vec{k}_0}(\vec{r}) + \Delta\vec{k} \cdot \nabla_{\vec{k}_0} u_{n\vec{k}_0}(\vec{r}) + \dots \quad (3.4)$$

As $a_{n\vec{k}}$ varies rapidly it is paramount to retain its full dependence on $\Delta\vec{k}$ so that

$$a_{n\vec{k}} = a_{n\Delta\vec{k}}. \quad (3.5)$$

If equations (3.2), (3.3), (3.4), and (3.5) are substituted into equation (3.1) it yields the following for $f_{n\vec{k}_0}(\vec{r}, t)$

$$f_{n\vec{k}_0}(\vec{r}, t) = e^{i\vec{k}_0 \cdot \vec{r}} u_{n\vec{k}_0}(\vec{r}) e^{-i(E_{n\vec{k}_0}/\hbar)t} \times \int d^3\Delta k a_{n\Delta\vec{k}} e^{i\Delta\vec{k} \cdot [\vec{r} - (\nabla_{\vec{k}_0} E_{n\vec{k}_0}/\hbar)t]}. \quad (3.6)$$

The expression obtained for $f_{n\vec{k}_0}(\vec{r}, t)$ represents a Bloch function of wave vector \vec{k}_0 which is modulated by an integral over $\Delta\vec{k}$ called the envelope function. Studying the value of the envelope function it is seen for giving values of \vec{r} and t the envelope function has the same value if all \vec{r} and t satisfy the equality

$$\vec{r} - (\nabla_{\vec{k}_0} E_{n\vec{k}_0}/\hbar)t = \text{const.}$$

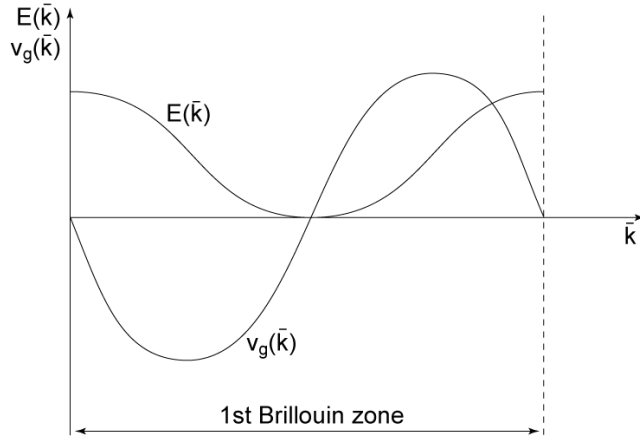
Looking at equation (3.6) the term $\nabla_{\vec{k}_0} E_{n\vec{k}_0}/\hbar$ must account for a velocity and is in fact known as the group velocity of the electron wave packet,

$$\vec{v}_g = \frac{1}{\hbar} \nabla_{\vec{k}_0} E_{n\vec{k}_0}. \quad (3.7)$$

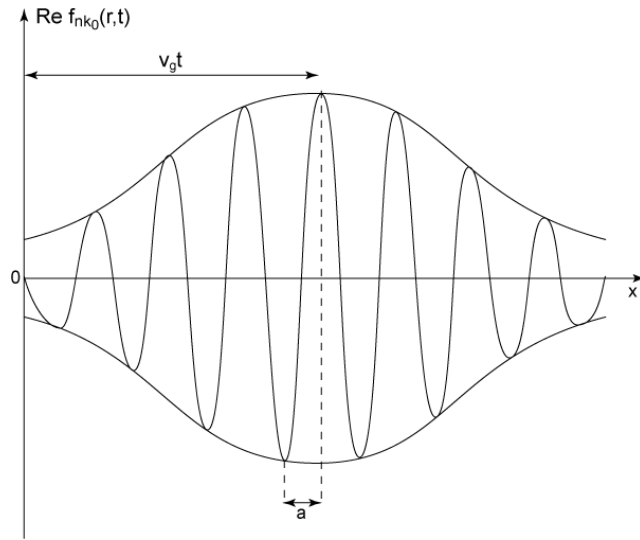
Equation (3.6) therefore represents the motion of the electron wave packet characterized by the group velocity in equation (3.7).

\vec{v}_0 is proportional to the \vec{k} -gradient of the Bloch state energy $E_{n\vec{k}}$. If a plot is constructed of $E_{n\vec{k}}$ versus \vec{k} then it can be determined by the slope of the curve, seen in figure 3.1(a) illustrating \vec{v}_g as a function of \vec{k} .

Furthermore a representation of the wave packet of an electron in the conduction band in real space is shown in figure 3.1(b).



(a) The energy as a function of the wavevector \vec{k} and the group velocity as a function of \vec{k} .



(b) Representation of a wave packet of the electron in the conduction band.

Figure 3.1: Inspired from [1, p.75].

3.1.1 Effective mass

The wave packet describing the motion of the electron can be regarded as a semi-classical description and thus several analogies concerning velocity, force and energy can be used from a classical point of view. First the time derivative is taken of the group velocity \vec{v}_g yielding the acceleration:

$$\frac{d\vec{v}_g}{dt} = \frac{d}{dt} \left(\frac{1}{\hbar} \nabla_{\vec{k}} E_{n\vec{k}} \right) = \frac{1}{\hbar} \nabla_{\vec{k}} \frac{dE_{n\vec{k}}}{dt}.$$

From classical mechanics the time derivative of the energy is related to the force acting on the particle

$$\frac{dE}{dt} = \vec{F} \cdot \vec{v}_g. \quad (3.8)$$

Equation (3.8) can be rewritten as

$$\frac{d\vec{v}_g}{dt} = \frac{1}{\hbar} (\nabla_{\vec{k}} \vec{v}_g) \cdot \vec{F}. \quad (3.9)$$

It is assumed that \vec{F} is independent on \vec{k} here.

On the right hand side of equation (3.9) \vec{v}_g is replaced by its definition in equation (3.7) yielding

$$\frac{d\vec{v}_g}{dt} = \frac{1}{\hbar^2} (\nabla_{\vec{k}} \nabla_{\vec{k}} E_{n\vec{k}}) \cdot \vec{F}. \quad (3.10)$$

The left hand side in equation (3.10) contains the acceleration and by comparison to Newton's second law of motion the quantity $\hbar^2 \nabla_{\vec{k}} \nabla_{\vec{k}} E_{n\vec{k}}$ must have the dimension of inverse mass. Hence, for a simple parabolic band, the inverse effective mass tensor is

$$\frac{1}{m_n^*} = \frac{1}{\hbar^2} \frac{\partial^2 E_{n\vec{k}}}{\partial k^2}. \quad (3.11)$$

Conclusively it seen that the curvature of the energy band is proportional to the inverse effective mass. If the curvature is increased the effective mass decreases accordingly.

3.1.2 Dynamics of electrons and holes

From equation (3.8) the chain rule is applied to the derivative of E yielding

$$\frac{d\vec{k}}{dt} \cdot \nabla_{\vec{k}} E_{n\vec{k}} = \vec{F} \cdot \vec{v}_g.$$

The gradient of the band energy is replaced with the aid of equation (3.7) and by cancellation of the group velocity on each side the equation becomes

$$\vec{F} = \hbar \frac{d\vec{k}}{dt}. \quad (3.12)$$

If the expression for the force \vec{F} in equation (3.12) is compared to the classical relation

$$\vec{F} = \frac{d\vec{p}}{dt},$$

the quantity $\hbar \vec{k}$ is identified as \vec{p} , the so-called crystal momentum of the electron in the crystal lattice.

To describe the dynamics of electrons in the crystal an external force of an applied field \vec{E} is examined. The force becomes

$$\vec{F} = -e\vec{E} \quad (3.13)$$

and thus

$$\hbar \frac{d\vec{k}}{dt} = -e\vec{E}. \quad (3.14)$$

By applying an electrical field the wave vector \vec{k} changes over time as a direct consequence. Combining equation (3.10) and (3.13) yields

$$\frac{d\vec{v}_g}{dt} = \frac{1}{m^*} \cdot \vec{F} \Leftrightarrow \frac{d\vec{v}_g}{dt} = -e \left(\frac{1}{m^*} \right) \vec{E},$$

showing that the electron wave packet is in fact accelerated by the applied electrical field yielding a current.

The electrical conduction described in the above is only valid for a partially filled energy band. When an external field is applied an electron of wave vector \vec{k} can make a transition in the band if there is an empty state available of different wave vector nearby. On the other hand if the band is completely filled the electron cannot undergo any transition as there are no available states. Thus the conductivity of a filled band is zero.

A distinction between insulators and conductors can then be stated. The former has all bands including a certain band completely filled with electrons at 0K. All bands above are completely empty and an energy gap separate the two by an amount $E_g \gg k_B T_r$, where T_r is the room temperature. The latter has at least one partially filled band and if the present electrons excite due to thermal excitation across a normally forbidden energy gap from a filled band, it is defined to be a semiconductor. If one or more bands continue to be partially filled at 0K the material is a metal or semi metal. [1, p. 74-77]

3.1.3 Holes

When an electron is excited from a filled energy band to an unfilled energy band the empty state left is called a hole state. The holes lying near the band edge of the valence band are of great importance in the semiconductor as they contribute to the current. To study the properties of a hole its wave vector is examined firstly.

The total wave vector of the electrons in the filled band is zero, $\sum \vec{k} = 0$, summing over all states in the Brillouin zone. If the band is filled all pairs of \vec{k} and $-\vec{k}$ are filled resulting in a total wave vector of zero. In the case of a missing electron of wave vector \vec{k}_e the total wavevector of the system is changed to $-\vec{k}_e$ obtained by the hole. The hole wave vector is not that of the missing electron but the negative of it.

The energy of the hole is deduced in the following. The excited electron experiences an increase in $|\vec{k}_e|$ resulting in a decrease of the vacant state energy by the amount $E_e(\vec{k}_e)$. The vacant state moves lower into the valence band, from a higher energy state to a lower energy state. However, the total energy of the electrons in the band increases by an equal amount as an occupied state makes the reverse transition. Conclusively the energy of the hole, $E_h(\vec{k}_h)$, is defined to

$$E_h(\vec{k}_h) = -E_e(\vec{k}_e).$$

Furthermore due to $\vec{k}_h = -\vec{k}_e$ it follows that,

$$E_h(\vec{k}_h) = -E_e(-\vec{k}_h).$$

As stated in the above it follows that for every state \vec{k} there is another state of equal energy with wave vector $-\vec{k}$ ¹, thus

$$E_h(\vec{k}_h) = -E_e(\vec{k}_h). \quad (3.15)$$

It is seen that E_e is a decreasing function of its argument and E_h is an increasing function of its argument.

If it is assumed that the valence band is spherical parabolic the energy dispersion is

$$E_e(\vec{k}_e) = E_V + \frac{\hbar^2 k_e^2}{2m_e^*}, \quad (3.16)$$

where E_V is the energy of the valence band edge and m_e^* is the negative effective mass. The hole energy is thus

$$E_h(\vec{k}_h) = -E_V - \frac{\hbar^2 k_h^2}{2m_e^*}.$$

The result is rewritten as

$$E_h(\vec{k}_h) = -E_V + \frac{\hbar^2 k_h^2}{2m_h^*}, \quad (3.17)$$

where m_h^* is the mass of the hole. It follows from equation (3.11) that the effective mass is inversely proportional to the curvature of the energy band. Since the dispersion for the electron follows the relation in equation (3.16), and according to equation (3.17), it is clear that $m_h^* = -m_e^*$. Since m_e^* is negative, m_h^* is positive [1, p. 77-78]. The dispersion for the missing electron and hole energies versus wave vector are shown in figure 3.2.

Lastly the group velocity and the charge of the hole are studied. The group velocity is given by

$$\vec{v}_{gh} = \frac{1}{\hbar} \nabla_{\vec{k}_h} E_h(\vec{k}_h),$$

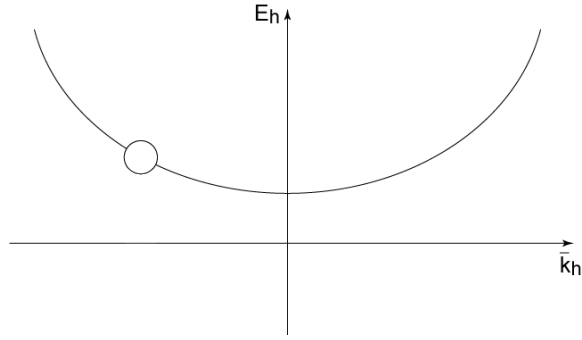
and for the electron missing in the valence band

$$\vec{v}_{ge} = \frac{1}{\hbar} \nabla_{\vec{k}_e} E_e(\vec{k}_e).$$

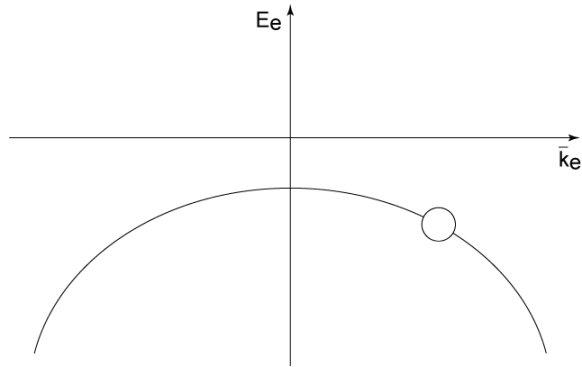
With $\vec{k}_e = -\vec{k}_h$ it becomes

$$\vec{v}_{ge} = -\frac{1}{\hbar} \nabla_{\vec{k}_h} E_e(-\vec{k}_h) = -\frac{1}{\hbar} \nabla_{\vec{k}_h} E_e(\vec{k}_h).$$

¹This has its origins in the fact that the bands are always symmetric under the inversion of $\vec{k} \rightarrow -\vec{k}$. [6, p.195]



(a) Missing electron band



(b) Hole band

Figure 3.2: (a) The hole energy E_h versus wave vector and (b) missing electron energy E_e versus wave vector. The circles represent a pair of missing electron and hole. Inspired from [1, p.78].

Using equation (3.15) yields

$$\vec{v}_{ge} = \frac{1}{\hbar} \nabla_{\vec{k}_h} E_h(\vec{k}_h) = \vec{v}_{gh}.$$

Conclusively the group velocity of the hole and the missing electron are identical.

Finally the charge of the hole can be found by utilizing the equation of motion, (3.14), to the missing electron

$$\hbar \frac{d\vec{k}_e}{dt} = -e\vec{E}.$$

Using $\vec{k}_e = -\vec{k}_h$ the equation of motion for the hole is

$$\hbar \frac{d\vec{k}_h}{dt} = e_h \vec{E},$$

It is seen that the charge of the hole is positive, $e_h = +e$.

3.2 Semiconductor impurities

Silicon doped with phosphorus introduces impurities in the structure of the semiconductor and this has several effects. Silicon is a group IV element that enables

it to form four bindings to another element. Phosphorous is a group V element that can contribute with five electrons. Introduced to Si it can enter substitutionally in the crystal structure and form four electron pairs from four neighboring silicon atoms. The excessive fifth electron is bound to the P^+ ion at sufficiently low temperatures, but at higher T it is thermally excited to the conduction band and not bound to the P^+ ion. This is illustrated in figure 3.3.

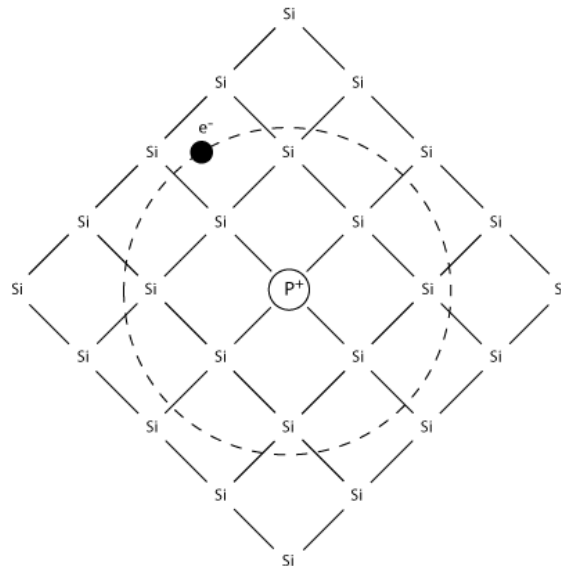


Figure 3.3: Phosphorous atom introduced in the silicon lattice as substitute thereby forming a donor state P^+ . Inspired from [1, p.90]

Phosphorous acts like a donor creating a donor impurity because it donates an electron to the conduction band. The current carriers provided by phosphorous are negatively charged conduction electrons and hence silicon doped with P is known as n-type silicon. Other elements behave much similar to phosphorus such arsenic and antimony.

A group III element such as boron of the periodic table can also enter into the lattice of silicon. Boron lacks one electron to form four electron pair bonds with the four nearest silicon atoms. The missing electron of boron can be regarded as hole and thereby add to the conduction. At sufficiently low temperatures the hole cannot escape and is bound to the boron atom. At sufficient temperatures an electron from a far away electron pair bond can transfer to the boron atom and together with the three electrons form four electron pair bonds with nearest neighboring silicon atoms. In this process the hole is transferred from the boron atom to the far away electron pair and thus no longer bound to the boron atom. During this the boron atom has become negatively charged due to the extra electron.

Boron is called an acceptor as it accepts an electron from the crystal lattice of silicon. Therefore silicon doped with boron is called p-typed as the current carriers from boron are positively charged holes. Similar to boron are group III elements such as aluminum or gallium.

Elements in group VI, sulfur or selenium e.g., also posses interesting features when doping due to the donation of two electrons to the conduction band. Dop-

ing with a group II element would as a result lead to a double acceptor state.[1, p. 89-90]

Chapter 4

Diffusion

This chapter aims to describe the physics of diffusing impurities into a opposite doped substrate and the methods utilized to measure the dopant concentration achieved.

4.1 Fick's diffusion equation

A material which is free to move and introduced to a dopant will experience a net redistribution of the impurity atoms away from the concentration maximum. This movement away from the concentration maximum will cause the gradient of the concentration to decrease. This is one of the basic laws of diffusion. Illustrated later in 4.1(a).

In one dimension Fick's first law takes the form

$$J = -D \frac{\partial C(x,t)}{\partial x}, \quad (4.1)$$

where J is the flux of material, D is the coefficient of diffusion, and C is the impurity concentration. The negative sign is due to the before mentioned fact, that there is net movement away from the concentration maximum.

As the diffusing material is usually not easily measured, Fick's second law has been developed involving more easily measured quantities. If a differential volume element of length dx in a long bar of material with a uniform cross section is considered, then

$$\frac{J_2 - J_1}{dx} = \frac{\partial J}{\partial x},$$

where J_1 and J_2 is the flux entering and leaving the volume, respectively. If these two fluxes are not equal the concentration of the diffusing species has changed. The continuity equation is then

4.1 Fick's diffusion equation

$$\frac{dN}{dt} = A dx \frac{\partial C}{\partial t} = -A(J_2 - J - 1) = -A dx \frac{\partial J}{\partial x}, \quad (4.2)$$

where N is the number of impurities in the volume element and A is the cross-sectional area. Equation (4.2) can be reduced to

$$\frac{\partial C(x,t)}{\partial t} = -\frac{\partial J}{\partial x}. \quad (4.3)$$

If equation (4.3) is inserted in equation (4.1) one has

$$\frac{\partial C(x,t)}{\partial t} = \frac{\partial}{\partial x} \left(D \frac{\partial C}{\partial x} \right), \quad (4.4)$$

which is the most general form of Fick's second law. If it is assumed that the diffusion coefficient is independent of position equation (4.4) reduces to

$$\frac{\partial C(z,t)}{\partial t} = D \frac{\partial^2 C(z,t)}{\partial z^2},$$

where z is the direction into the wafer. Fick's second law in three dimensions for an isotropic medium is then

$$\frac{\partial C}{\partial t} = D \nabla^2 C. \quad (4.5)$$

Equation (4.5) is a differential equation, which is first order in time and second order in position. To solve this differential equation at least two independent boundary conditions are required. The diffusion coefficient in equation (4.5) can be found by means of atomistic models, but for now the diffusion coefficient will be assumed to be constant. [2, p. 43-45]

The concentration is found for the predeposition- and drive-in diffusion situations. The predeposition diffusion situation requires a constant surface concentration. Thus the boundary conditions are

$$\begin{aligned} C(z, 0) &= 0 \\ C(\infty, t) &= 0 \\ C(0, t) &= C_s, \end{aligned}$$

which yields the solution

$$C(z,t) = C_s \operatorname{erfc}\left(\frac{z}{2\sqrt{Dt}}\right), \quad t > 0. \quad (4.6)$$

In equation (4.6) C_s is the fixed surface concentration, erfc is the complementary error function and \sqrt{Dt} is the characteristic diffusion length.

The dose diffused into the substrate varies with the time of diffusion and can be derived by integrating the profile of the concentration

$$\begin{aligned} Q_T(t) &= \int_0^\infty C(z,t) dz \\ &= \frac{2}{\sqrt{\pi}} C_s \sqrt{Dt}. \end{aligned}$$

The dose increase as the square root of the time and is measured in units of impurities per unit area.

For the drive-in diffusion situation the source of diffusing impurity atoms is limited to Q_T . For a diffusion length much larger than the width of the initial profile, the initial profile can be approximated to be a delta function, meaning that the initial impurity atoms are only present at the surface. This gives the boundary conditions

$$\begin{aligned} C(z,0) &= 0, \quad z \neq 0 \\ C(\infty,t) &= 0 \\ \frac{dC(0,t)}{dz} &= 0 \\ Q_T(t) &= \int_0^\infty C(z,t) dz = \text{constant}. \end{aligned}$$

The solution for these boundary conditions is a Gaussian with center at $z = 0$

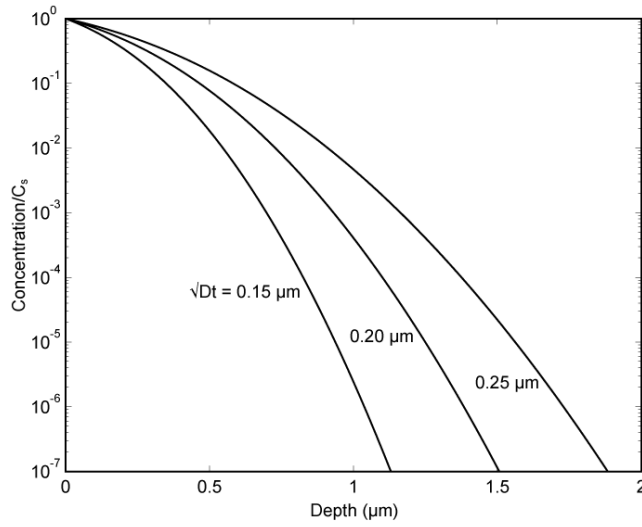
$$C(z,t) = \frac{Q_T}{\sqrt{\pi Dt}} e^{-\frac{z^2}{4Dt}}, \quad t > 0. \quad (4.7)$$

As the source of diffusing impurity atoms is limited the surface concentration decreases with time as

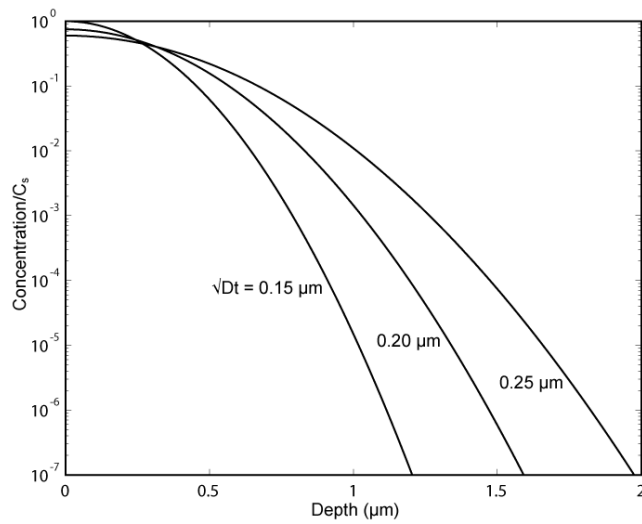
$$C_s = C(0,t) = \frac{Q_T}{\sqrt{\pi Dt}}.$$

Figure 4.1(a) and 4.1(b) illustrates the predeposition and drive-in diffusion, respectively.

4.1 Fick's diffusion equation



(a) Predeposition diffusion.



(b) Drive-in diffusion

Figure 4.1: Illustrates the concentration profiles for predeposition- and drive-in diffusion for three different characteristic diffusion lengths.

Assuming that phosphorus is diffusing into a silicon substrate with a uniform concentration of boron, C_B , and that $C_s \gg C_B$, a pn-junction will form at a certain depth, where the concentration of phosphorus cancels out the concentration of boron, as boron and phosphorus in silicon are p- and n-type dopants, respectively. From equation (4.7) the junction depth x_j can be shown to be

$$x_j = \sqrt{4Dt \ln \left[\frac{Q_T}{C_B \sqrt{\pi Dt}} \right]}$$

in case of drive-in diffusion. And from equation (4.6) in case of predeposition diffusion to be

$$x_j = 2\sqrt{Dt} \operatorname{erfc}^{-1} \left[\frac{C_B}{C_s} \right],$$

see figure 4.2.

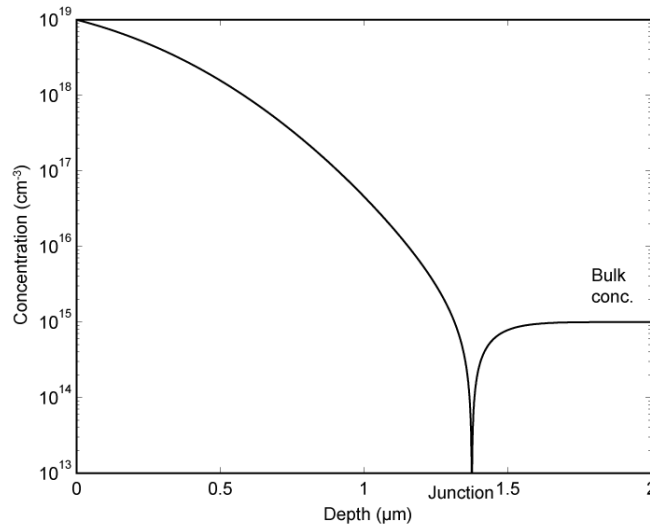


Figure 4.2: Illustrates a typical concentration plot of impurities as a function of depth. At the junction depth the bulk impurities succeed the diffused impurities.

4.2 Profile analysis

When the impurity ions have been diffused, it is desirable to obtain the concentration of the impurities as a function of depth. This can be done by measuring the sheet resistance

$$R_S = [q \int \mu(C) C_e(z) dz]^{-1}, \quad R_S = \left[\frac{\Omega}{\text{square}} \right]$$

where $C_e(z)$ is the carrier concentration, $\mu(C)$ the concentration dependent mobility, and q is the charge.

The sheet resistance can be measured in several ways, where the simplest is by using a four-point probe. Four-point probe measurements can be conducted in several ways itself. The most common is the collinear approach, see figure 4.3(a), where current is passed through the sample between two outer probes and the voltage is measured between the inner pair of probes. The sheet resistance is found by

the ratio between the measured voltage drop and the forced current. The result must be multiplied by a correction factor, which depends on the probe geometry and the ratio between the probe spacing and the thickness of the diffusion. However, for probe spacings much larger than the junction depth, the correction factor is 4.5325 in the collinear approach. For this method to be reliable the underlying substrate must be of much higher resistance than the layer to be measured or the layer to be measured must form a reverse-biased diode with the substrate. In the latter case, the force of the probe to the surface should not be too large or the probes could penetrate very shallow junctions and the sheet resistance measurements would include the effect of the depleted region near the junction.

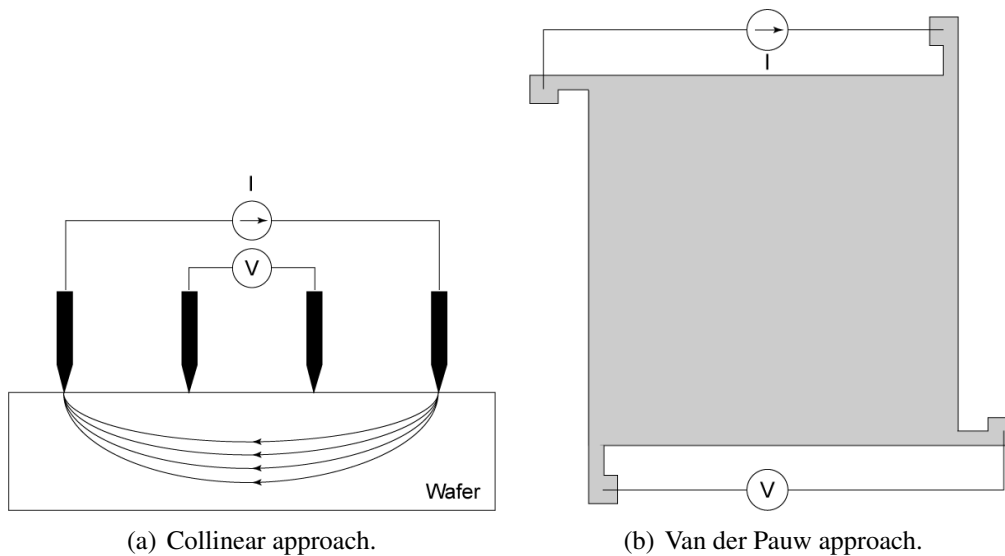


Figure 4.3: Illustrates two methods of measuring the sheet resistance of a sample. Inspired from [2, p. 57].

Another approach to the four-point probe measurement is the Van der Pauw method, see figure 4.3(b), which is done by contacting the edge of a randomly shaped sample at four places. A current is again forced between two contacts and the voltage is measured between two other contacts. To obtain the best accuracy possible the sample is rotated 90° three times so that four different measurements are conducted. The average resistance is then

$$R = \frac{1}{4} \left[\frac{V_{12}}{I_{34}} + \frac{V_{23}}{I_{41}} + \frac{V_{34}}{I_{12}} + \frac{V_{41}}{I_{23}} \right].$$

And the sheet resistance is

$$R_S = \frac{\pi}{\ln(2)} F(Q) R,$$

where $F(Q)$ is the geometry dependent correction factor. For a square the contacts must be made on the side of the sample, which yields a correction factor $F(Q) = 1$. For proper measurements ohmic contacts can be applied. [2, p. 55-56]

Chapter 5

Semiconductor Statistics

This chapter contributes to the calculation of the concentration of electrons and holes in the spherical parabolic and ellipsoidal energy bands in semiconducting materials. Furthermore the Fermi energy is found for an intrinsic semiconductor and the electron-hole ratio is derived for extrinsic semiconductors.

In order to calculate certain properties such as the diffusion potential it is necessary to know the concentrations of negatively and positively charged carriers in the conduction band and the valence band, respectively. Firstly, carriers can arise due to different types of excitations like thermal and optical excitations from valence to conduction band. If excitations mostly occur from valence band to conduction band the semiconductor is classified as an intrinsic semiconductor. Secondly, current carriers can occur by excitations from or to impurity states. If excitations mostly occur from impurity states the semiconductor is classified as an extrinsic semiconductor. And thirdly, current carriers can occur by excitations from an external source. In this chapter thermal excitations will be ignored meaning the semiconductor is in thermal equilibrium. [1, p.101]

5.1 Intrinsic semiconductors

If an intrinsic semiconductor with band gap E_g is considered, the Fermi-Dirac distribution

$$f_{FD}(\vec{k}) = \frac{1}{e^{\frac{E_{\vec{k}} - E_F}{k_B T}} + 1}, \quad (5.1)$$

specifies the electron occupation number of a state of energy $E_{\vec{k}}$ in thermal equilibrium at temperature T . k_B is Boltzmann's constant and E_F is the Fermi energy. If $T = 0$ then $f_{FD} = 1$ when $E_{\vec{k}} < E_F$, and $f_{FD} = 0$ when $E_{\vec{k}} > E_F$, signifying that all states with energies lower than the Fermi energy are occupied and all states with energies higher than the Fermi energy are unoccupied at $T = 0$. As the temperature rises more states with energies lower than the Fermi energy will be unoccupied and

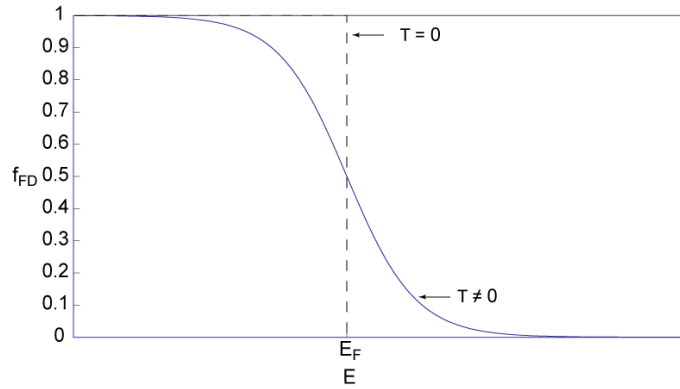


Figure 5.1: The Fermi-Dirac distribution function plotted against the energy for $T = 0$ and for $T \neq 0$. Inspired from [1, p. 102]

more states with energies higher than the Fermi energy will be occupied. The two situations for $T = 0$ and $T > 0$ are illustrated in figure 5.1, where the Fermi-Dirac distribution function is plotted against the energy.

The concentration of electrons in the conduction band is given by

$$\begin{aligned} n &= \frac{2}{\Omega} \sum_{\vec{k}} f_{FD}(\vec{k}) \\ &= \frac{2}{\Omega} \sum_{\vec{k}} \frac{1}{e^{\frac{E_{c\vec{k}} - E_F}{k_B T}} + 1}, \end{aligned} \quad (5.2)$$

where the sum is over all states in the conduction band with energies $E_{c\vec{k}}$, Ω is the volume of the system and the factor 2 is due to spin degeneracy. By converting the sum over \vec{k} to an integral

$$\sum_{\vec{k}} \longrightarrow \frac{\Omega}{(2\pi)^3} \int d^3k,$$

equation (5.2) becomes

$$n = \frac{2}{(2\pi)^3} \int d^3k \frac{1}{e^{\frac{E_{c\vec{k}} - E_F}{k_B T}} + 1}. \quad (5.3)$$

An analytic evaluation of the Fermi-Dirac integral is only possible with certain approximations of the energy bands. [1, p. 101-103]

5.1.1 Spherical parabolic energy bands

In the case of a spherical parabolic conduction band with an effective mass m_c^* , the energy of the conduction band is given by

$$E_{c\vec{k}} = E_C + \frac{\hbar^2 k^2}{2m_c^*}.$$

Here E_C is the edge of the conduction band. If it is assumed that $k_B T \ll E_C - E_F$, then the quantity +1 in equation (5.1) can be ignored. The Fermi-Dirac distribution can then be approximated to

$$f_{FD}(\vec{k}) \approx e^{-\frac{E_F - E_C}{k_B T} - \frac{\hbar^2 k^2}{2m_c^*}}.$$

Consequently equation (5.3) becomes

$$n = \frac{2}{(2\pi)^3} \int e^{-\frac{E_F - E_C - \frac{\hbar^2 k^2}{2m_c^*}}{k_B T}} d^3 k.$$

By introducing spherical coordinates

$$\begin{aligned} n &= \frac{2}{(2\pi)^3} \int_0^\pi \int_0^{2\pi} \int_0^\infty e^{-\frac{E_F - E_C - \frac{\hbar^2 k^2}{2m_c^*}}{k_B T}} k^2 \sin\phi \, dk d\theta d\phi \\ n &= \frac{2}{(2\pi)^3} 2 \cdot 2\pi \int_0^\infty k^2 e^{-\frac{E_F - E_C - \frac{\hbar^2 k^2}{2m_c^*}}{k_B T}} dk \\ n &= \frac{2}{2\pi^2} e^{-\frac{E_F - E_C}{k_B T}} \int_0^\infty k^2 e^{-\frac{\hbar^2 k^2}{2m_c^*}} dk, \end{aligned}$$

and changing the variable of integration from k to $E = \frac{\hbar^2 k^2}{2m_c^*}$ the concentration of electrons in the conduction band is now

$$\begin{aligned} n &= \frac{2}{2\pi^2} e^{-\frac{E_F - E_C}{k_B T}} \int_0^\infty \frac{1}{2} \left(\frac{2m_c^*}{\hbar^2} \right)^{3/2} E^{1/2} e^{-\frac{E}{k_B T}} dE \\ n &= e^{-\frac{E_F - E_C}{k_B T}} \int_0^\infty N_c(E) e^{-\frac{E}{k_B T}} dE, \end{aligned} \quad (5.4)$$

where

$$N_c(E) = \frac{1}{2\pi^2} \left(\frac{2m_c^*}{\hbar^2} \right)^{3/2} E^{1/2}$$

is the density-of-states in energy for the conduction band. The density-of-states is plotted against the energy in figure 5.2 and the free carrier concentration is plotted against the energy in figure 5.3.

If the constants of integration are left out the integral in equation (5.4) becomes

$$\begin{aligned} \int_0^\infty E^{1/2} e^{-\frac{E}{k_B T}} dE &= \Gamma\left(\frac{3}{2}\right) (k_B T)^{3/2} \\ &= \frac{\sqrt{\pi}}{2} (k_B T)^{3/2}, \end{aligned}$$

reducing equation (5.4) to

$$n = \bar{N}_c e^{-\frac{E_F - E_C}{k_B T}}, \quad (5.5)$$

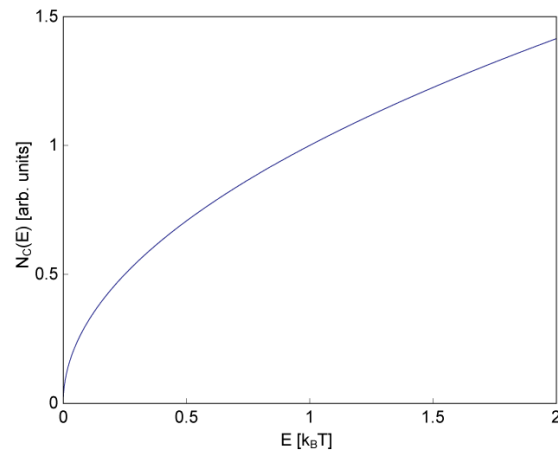


Figure 5.2: Density-of-states plotted against the energy. Inspired from [1, p. 104]

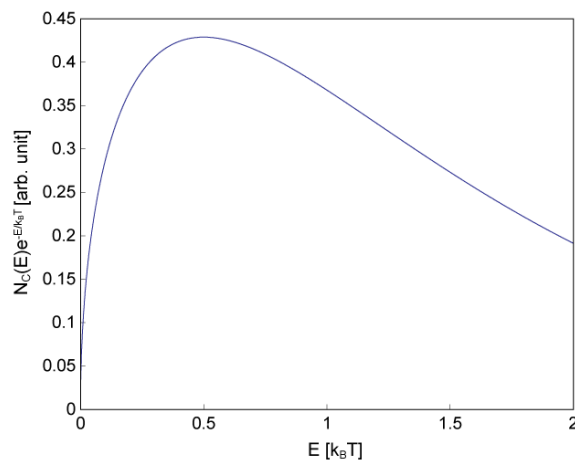


Figure 5.3: Free carrier concentration plotted against the energy. Inspired from [1, p. 104]

where

$$\bar{N}_c = 2 \left(\frac{m_c^* k_B T}{2\pi\hbar^2} \right)^{3/2} \quad (5.6)$$

is the effective density-of-states for the conduction band. \bar{N}_c represents a weighted sum of all the occupied states in the conduction band, where the weighting coefficient is the Boltzmann factor. It implies that the higher the energy of the state in the conduction band, the lower the probability of electron occupation. At a given temperature \bar{N}_c represents the degeneracy of the conduction band if it is regarded as a single level with the energy E_C . Equation (5.6) is only valid if $k_B T \ll E_C - E_F$ meaning that the system is non-degenerate, where the Boltzmann distribution has been used due to approximations. If $k_B T \ll E_C - E_F$ is not fulfilled the full Fermi-Dirac distribution must be used and consequently the carriers form a degenerate system. Whereas non-degenerate semiconductors have relatively low concentration of shallow impurities, the concentration of shallow impurities is relatively high in degenerate semiconductors. This high concentration of shallow impurities can lead to formation of impurity bands due to overlapping of atomic orbitals of neighbouring impurities. The Fermi energy can then lie sufficiently close to the energy of the conduction band resulting in a degenerate behaviour persisting to low temperatures.

Holes in the valence band are states lacking an electron, thus the distribution function for holes in the valence band is $1 - f_{FD}$. The concentration of holes p can then be written as

$$p = \frac{2}{\Omega} \sum_{\vec{k}} [1 - f_{FD}(\vec{k})] = \frac{2}{\Omega} \sum_{\vec{k}} \frac{1}{e^{\frac{E_F - E_{v\vec{k}}}{k_B T}} + 1},$$

where $E_{v\vec{k}}$ is the energy of a state in the valence band. As in the situation concerning electrons the valence band is considered spherical and parabolic with band edge E_V and effective mass m_v^* . The energy of the valence band state is then

$$E_{v\vec{k}} = E_V - \frac{\hbar^2 k^2}{2m_v^*}.$$

Again the temperature is considered sufficiently low so $k_B T \ll E_F - E_V$ yielding the concentration of holes

$$p = \bar{N}_v e^{\frac{E_V - E_F}{k_B T}}, \quad (5.7)$$

where \bar{N}_v is the effective density-of-states for holes

$$\bar{N}_v = 2 \left(\frac{m_v^* k_B T}{2\pi\hbar^2} \right)^{3/2},$$

analogous to the electron situation.

Combining equation (5.5) and (5.7) the Fermi energy, which is yet unknown, is eliminated

$$np = \bar{N}_c \bar{N}_v e^{-\frac{E_g}{k_B T}} = n_i^2, \quad (5.8)$$

where $E_g = E_C - E_V$ and n_i is the intrinsic carrier concentration. Equation (5.8) is called the law of mass action and implies that at a given temperature the product of electron and hole concentrations in a non-degenerate semiconductor is constant. The fundamental approximation is that the difference between the conduction band and the Fermi energy and between the Fermi energy and the valence band is large compared to the thermal energy $k_B T$. No assumptions concerning the source of the electrons and holes have been made. In case of excitation across the band gap in an intrinsic semiconductor $n = p$ due to charge conservation. Thus from equation (5.8) it follows that

$$\begin{aligned} n = p = n_i &= (\bar{N}_c \bar{N}_v)^{1/2} e^{-\frac{E_g}{2k_B T}} \\ &= 2 \left(\frac{k_B T}{2\pi\hbar^2} \right)^{3/2} (m_c^* m_v^*)^{3/4} e^{-\frac{E_g}{2k_B T}}. \end{aligned} \quad (5.9)$$

It is seen that the concentration of electrons and holes increases as the temperature rises and the energy gap is reduced.

As the concentration of n and p has been found the Fermi energy for an intrinsic semiconductor can be derived from equations (5.5) and (5.9)

$$\begin{aligned} 2 \left(\frac{m_c^* k_B T}{2\pi\hbar^2} \right)^{3/2} e^{\frac{E_{Fi} - E_C}{k_B T}} &= 2 \left(\frac{k_B T}{2\pi\hbar^2} \right)^{3/2} (m_c^* m_v^*)^{3/4} e^{-\frac{E_g}{2k_B T}} \\ m_c^{*3/2} e^{\frac{E_{Fi} - E_C}{k_B T}} &= (m_c^* m_v^*)^{3/4} e^{-\frac{E_g}{2k_B T}} \\ e^{\frac{E_{Fi} - E_C + 1/2 E_g}{k_B T}} &= \left(\frac{m_v^*}{m_c^*} \right)^{3/4} \\ E_{Fi} &= E_C - \frac{1}{2} E_g + \frac{3}{4} k_B T \ln \left(\frac{m_v^*}{m_c^*} \right). \end{aligned} \quad (5.10)$$

From equation (5.10) is seen that when $T = 0$ the intrinsic Fermi energy lies in the middle of the band gap. As the temperature rises the Fermi energy will increase when $m_v^* > m_c^*$ and decrease when $m_v^* < m_c^*$. If $m_v^* = m_c^*$ the Fermi energy lies in the middle of the band gap at all temperatures.[1, p. 103-106]

5.2 Extrinsic semiconductors

When impurity atoms are introduced to an intrinsic semiconductor, the semiconductor becomes extrinsic. The impurity atom, replacing a host atom in the crystal lattice, has either a higher or lower valence number than the host atom. If the valence number is higher than the one of the replaced host atom, then, at low temperatures, an electron will be bound to the positively charged ion and be excited to the conduction band at higher temperatures. Thus the impurity atom has donated an electron to the conduction band of the semiconductor and consequently the semiconductor is an n-type. If the valence number is lower than the one of the replaced host atom, then the missing electron can be regarded as a hole. At sufficiently low temperatures

the hole will be bound to the impurity atom, but at rising temperatures the hole will be replaced by an electron from a lattice atom far away. Thus the impurity atom is now a negatively charged ion and a hole has been added to the valence band making the semiconductor a p-type.[1, p. 90]

Rewriting equations (5.5) and (5.7) to

$$\begin{aligned} n &= \bar{N}_c e^{\frac{E_F + E_{Fi} - E_{Fi} - E_C}{k_B T}} = n_i e^{\frac{E_F - E_{Fi}}{k_B T}} \\ p &= \bar{N}_v e^{\frac{E_V + E_{Fi} - E_{Fi} - E_F}{k_B T}} = n_i e^{\frac{E_{Fi} - E_F}{k_B T}}, \end{aligned}$$

a general expression for the ratio between the electron and hole concentration can be derived

$$\frac{n}{p} = e^{2\frac{E_F - E_{Fi}}{k_B T}}. \quad (5.12)$$

From equation (5.12) it can be concluded that if the Fermi energy of the doped semiconductor is higher than that of the intrinsic semiconductor, then the concentration of electrons will be higher than the concentration of holes and vice versa.

The fact that impurity levels are localized states complicates a detailed statistical analysis. If a charge carrier of a given spin is already in a localized impurity orbital, it will cause a large change in energy to add a second carrier of opposite spin to the orbital as a result of the Coulomb repulsion of the two carriers. [1, p. 109-110]

Chapter 6

Junctions in Semiconductors at Thermal Equilibrium

This chapter contributes to describing the development of a diffusion potential, build-in electric field, and thus the behaviour of the energy bands in a pn-junction in thermal equilibrium. Furthermore the general principles governing the electronic structure of a metal-semiconductor junction is described.

To understand the principles of a solar cell it is important to understand the physics taking place in the junction between n- and p-type materials. The principle impurities of an n-type material are donors and thus the majority charge carriers are electrons in the conduction band, arising primarily from the ionized donor atom. Similarly, the principle impurities of a p-type material are acceptors and the majority carriers are holes arising from the acceptor atom. Together with the majority charge carriers from the impurity atoms thermally excited electrons and holes are still present. In case of a p-type material thermally excited electrons in the conduction band are minority carriers and in case of an n-type material thermally excited holes in the valence band are minority carriers.

If a rectangular slab of a semiconductor, as shown in figure 6.1, consisting of two parts, where one is p-type and one is n-type, is considered, the internal interface between the p- and n-type regions is called a pn-junction. The concentrations of donor and acceptor atoms can be either discontinuous across the interface, called an abrupt junction, or they can be continuous called a graded junction. This chapter will focus on the abrupt junction. [1, p. 308-309]

6.1 Space charge region

It is assumed that the acceptors in the p-type region and the donors in the n-type region are all shallow impurities, as the ionization energies are then in order of $k_B T$ at room temperature. Thus all impurity atoms are ionized at room temperature and consequently the concentration of holes p in the valence band is almost equal to the



Figure 6.1: Illustration of a rectangular slab of a semiconductor consisting of p-type material to the left and n-type material to the right. The interface between the p- and n-type region is called a pn-junction. Inspired from [1, p. 309].

concentration of acceptor impurities n_a in the p-type region. The concentration of electrons n in the conduction band is almost equal to the concentration of donor impurities n_d in the n-type region. See figure 6.2 for an illustration of the pn-junction before equilibrium, where the ionized acceptors and donors are indicated with encircled - and + signs, respectively.

Before the system is in equilibrium there is a very large concentration gradient

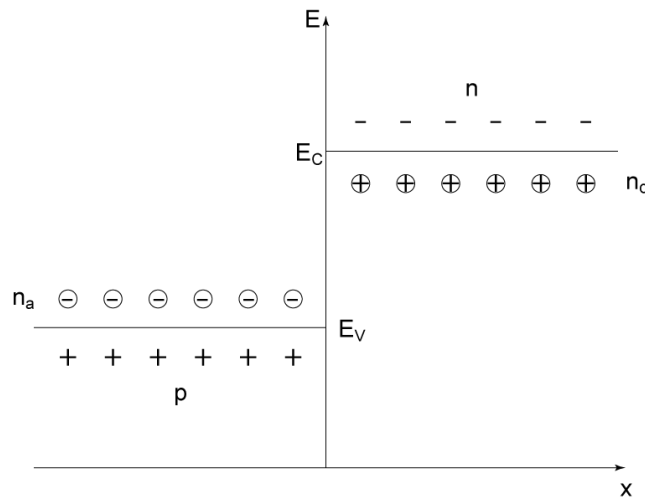


Figure 6.2: Illustration of the band diagram of a pn-junction before equilibrium. Inspired from [1, p. 309].

of electrons and holes at the interface between the n- and p-type region. At this stage there are different Fermi energies in the two regions. As the electrons start diffusing into the p-type region and the holes into the n-type region the Fermi energies finally reach a constant level throughout the system. Thus the basic criterion for thermal equilibrium is established. As a result of the diffusion of electrons and holes they start to recombine and a region near the interface is completely depleted of free carriers in the idealized situation. The electrons and holes, which compensated for the positively charged donors and negatively charged acceptors before equilibrium, have diffused into the p- and n-type region, respectively. Thus uncompensated charged ions are left to create a space charge region. The situation after thermal equilibrium is achieved is shown in figure 6.3.

As a result of the positive and negative ions in the space charge region a built-in electric field \vec{E} develops in this region. The electrons and holes experience the forces \vec{F}_e and \vec{F}_h , respectively, opposing the diffusion of electrons out of the n-type

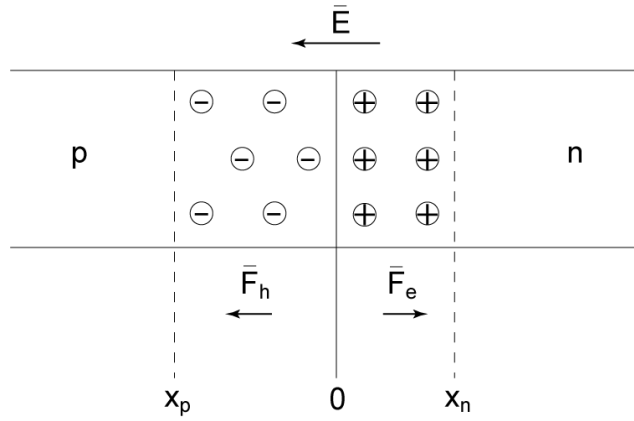


Figure 6.3: Illustration of the band diagram of a pn-junction after equilibrium. Inspired from [1, p. 310]

region and holes out of the p-type region due to the built-in electric field. Equilibrium requires that the current densities equals zero:

$$\begin{aligned}\vec{J}_e &= en\mu_e\vec{E} + eD_e\nabla n = 0 \\ \vec{J}_h &= en\mu_h\vec{E} + eD_h\nabla p = 0,\end{aligned}$$

where \vec{J}_e and \vec{J}_h are current densities for electrons and holes, μ_e and μ_h are their mobilities, and D_e and D_h their diffusion coefficients.[1, p. 308-310]

6.2 Charge density variation

The charge density $\rho(x)$ at a point x is given by

$$\rho(x) = e[n_d(x) - n_a(x) + p(x) - n(x)].$$

For $x \geq x_n$ the charge density is zero, as the thermally excited electrons and holes compensate for each others' charge. The charge due to the donor contribution to conduction electrons compensate for the positively charged donor ions. A Similar argument can be used to state that the charge density is zero for $x \leq x_p$. For $0 \leq x \leq x_n$ on the n-type side of the space charge region the only contribution to the charge density is the concentration of donor ions n_d , as the region is depleted of free charge carriers and no acceptor ions are present in the region. Finally for $0 \geq x \geq x_p$ on the p-type side of the space charge region the only contribution to the charge density is the concentration of acceptor ions n_a . As this region is also depleted of free charge carriers and no donor ions are present. Conclusively the charge density can be expressed as

$$\begin{aligned}\rho(x) &= 0 && \text{for } x \leq x_p \text{ and } x_n \leq x \\ \rho(x) &= -en_a && \text{for } x_p \leq x \leq 0\end{aligned}\tag{6.2a}$$

$$\rho(x) = en_d \quad \text{for } 0 \leq x \leq x_n.\tag{6.2b}$$

A plot of the charge density against x for an abrupt pn-junction is shown in figure 6.4.

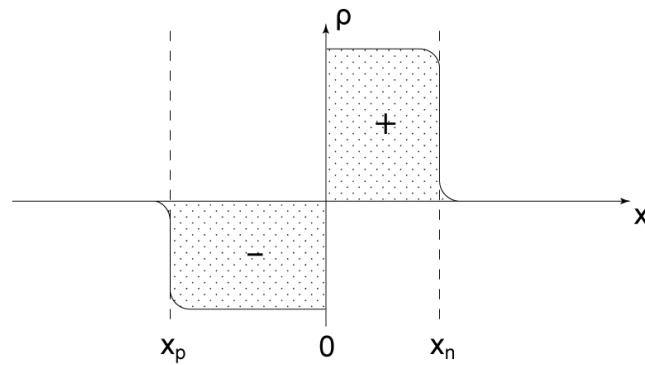


Figure 6.4: Illustration of the charge density ρ across the pn-junction. Inspired from [1, p. 311]

6.3 Diffusion potential

A build-in electric field arises in the space charge region due to the particular charge density distribution and can be written as the negative gradient of the electrostatic potential $V(\vec{r})$

$$\vec{E} = -\Delta V(\vec{r}). \quad (6.3)$$

The potentials in the different regions of the pn-junction are illustrated in figure 6.5.

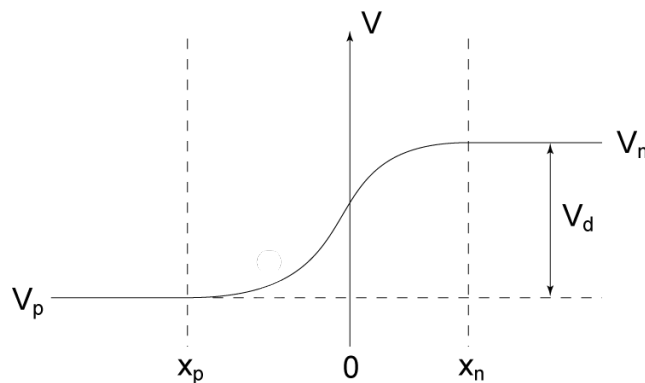


Figure 6.5: Illustrates the potential across the pn-junction. V_d is the diffusion potential, which is the difference between the potentials V_n and V_p . Inspired from [1, p. 311].

The diffusion potential V_d is the difference between the potentials in the neutral n-type and the p-type regions.

$$V_d = V_n - V_p. \quad (6.4)$$

In the situation of an ideal abrupt junction, where the build-in electric field is limited to the space charge region, the diffusion potential can be derived using the fact that

the system is at equilibrium. From equation (5.5) the electron concentration in the neutral n-type region can be written as

$$n_n = \bar{N}_c e^{\frac{E_F - E_{Cn}}{k_B T}} \quad (6.5)$$

and in the neutral p-type region as

$$n_p = \bar{N}_c e^{\frac{E_F - E_{Cp}}{k_B T}}, \quad (6.6)$$

where E_{Cn} and E_{Cp} are the energies of the conduction band minima in the neutral n- and p-type region, respectively. By isolating E_F and then equalizing equation (6.5) and (6.6) the difference in conduction band minima between the neutral n- and p-type region is found to

$$\begin{aligned} E_{Cp} - E_{Cn} &= k_B T \ln \left(\frac{n_n}{n_p} \right) \\ &= k_B T \ln \left(\frac{n_d n_a}{n_i^2} \right), \end{aligned}$$

where $n_n = n_d$ and the law of mass action

$$n_p = \frac{n_i^2}{p_p} = \frac{n_i^2}{n_a},$$

from equation (5.8) have been utilized. Generally, the conduction band minimum relates to the potential via

$$E_C = -eV,$$

e being the elementary charge. From equation (6.4) the diffusion potential is given as

$$\begin{aligned} V_d &= \frac{1}{e} (E_{Cp} - E_{Cn}) \\ &= \frac{k_B T}{e} \ln \left(\frac{n_n}{n_p} \right). \end{aligned}$$

6.4 Build-in electric field

To find the build-in electric field inside the space charge region it is seen from equation (6.3) that the potential in this region needs to be known. This can be derived by solving Poisson's equation with the charge density given by equation (6.2a) and (6.2b)

$$\frac{d^2 V}{dx^2} = -\frac{\rho(x)}{\epsilon_0 \epsilon}, \quad (6.7)$$

where ϵ is the dielectric constant of the junction.

If the region $x_p \leq x \leq 0$ is regarded, Poisson's equation becomes

$$\frac{d^2V}{dx^2} = -\frac{d\vec{E}}{dx} = \frac{en_a}{\epsilon_0\epsilon},$$

and after integration

$$\frac{dV}{dx} = -\vec{E}(x) = \frac{en_ax}{\epsilon_0\epsilon} + c_1. \quad (6.8)$$

The constant of integration c_1 is derived utilizing the boundary condition $\vec{E}(x_p) = 0$:

$$c_1 = -\frac{en_ax_p}{\epsilon_0\epsilon}$$

and equation (6.8) yields the build-in electric field at the p-type side of the space charge region

$$\vec{E}(x) = -\frac{en_a}{\epsilon_0\epsilon}(x - x_p). \quad (6.9)$$

Similarly the build-in electric field on the n-type side of the space charge region, where $0 \leq x \leq x_n$, can be found

$$\vec{E}(x) = \frac{en_d}{\epsilon_0\epsilon}(x - x_n). \quad (6.10)$$

Overall charge neutrality, illustrated in figure 6.6, in the space charge region requires that

$$x_p n_a = -x_n n_d,$$

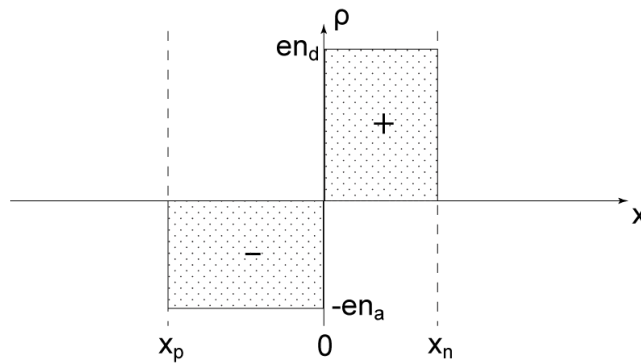


Figure 6.6: Illustrates the overall charge neutrality in the space charge region. Inspired from [1, p. 313].

which requires that $\vec{E}(x)$ is continuous at $x = 0$

$$\vec{E}(0) = \frac{en_ax_p}{\epsilon_0\epsilon} = -\frac{en_dx_n}{\epsilon_0\epsilon}.$$

At $x = 0$ the maximum electric field \vec{E}_m of the space charge region is found. This is illustrated in figure 6.7.

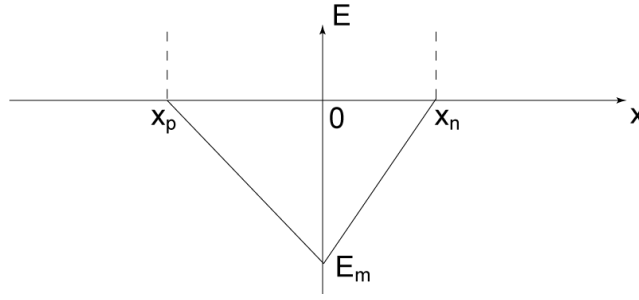


Figure 6.7: A plot of the built-in electric field as a function of x . Inspired from [1, p. 314].

6.5 Energy bands in space charge region

To find the potential energy of an electron in the pn-junction the potential $V(x)$ is multiplied by $-e$. If the valence band edge E_V is taken to be zero in the neutral p-type region, then it has the value

$$E_V(x) = -eV(x) \quad (6.11)$$

in the space charge region. As the band gap $E_g = E_C - E_V$ is constant in real space, an expression for the conduction band edge energy can be found

$$E_C(x) = E_g - eV(x). \quad (6.12)$$

The potential can be derived through

$$\frac{dV}{dx} = -\vec{E}(x).$$

This is done using the expressions (6.9) and (6.10) for the built-in electric field in the p- and n-type side of the space charge region, respectively. If the boundary condition $V(x_p) = V_p$ is used the potential in the p-type side of the space charge region is

$$V(x) = \frac{en_a(x - x_p)^2}{2\epsilon_0\epsilon} + V_p, \quad (6.13)$$

and if the boundary condition $V(x_n) = V_n$ is used in the n-type side of the space charge region, the potential is

$$V(x) = \frac{en_d(x - x_n)^2}{2\epsilon_0\epsilon} + V_n. \quad (6.14)$$

Thus, if equation (6.13) and (6.14) are substituted into equation (6.11) and (6.12), respectively, then the behaviour of the valence and conduction band edge in the space charge region is found. The behaviour of the bands are presented in figure 6.8. The band edges are tilted in the space charge region and the Fermi energy is constant throughout the structure due to thermal equilibrium. Considering the quasi-Fermi energies E_{Fn} and E_{Fp} in the neutral n- and p-type regions before equilibrium, where $E_{Fn} < E_{Fp}$, then the Fermi energy is given by

$$E_F = E_{Fn} - eV_d = E_{Fp}. \quad (6.15)$$

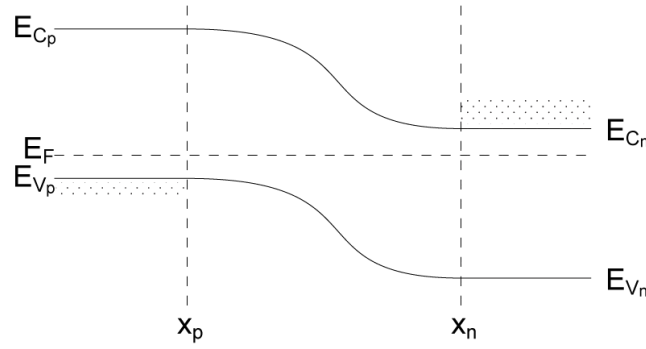


Figure 6.8: Illustration of the conduction and valence band edge behaviour throughout the pn-junction. The Fermi energy is constant through out the structure. A bending of the bands arises due to the junction formation. Inspired from [1, p. 315].

6.6 Solar cells

When light is absorbed in or near the pn-junction in a solar cell an electric potential is created. This is called the photovoltaic effect, see chapter 1. Photons of energy equal or higher than the band gap E_g can be absorbed and thereby excite electrons from the valence band to the conduction band creating electron-hole pairs. The build-in electric field then contributes to separation of the electrons and the holes, which otherwise would recombine, and thus electrical energy is created. The separation of electron and hole modifies the space charge, reducing the build-in electric field from \vec{E} to $\vec{E} - \vec{\bar{E}}$ under open circuit conditions. Thus the diffusion potential is reduced from V_d to $V_d - \bar{V}_d$ and consequently the energy barrier, which the electrons and holes have to surpass, is reduced to $e(V_d - \bar{V}_d)$. \bar{V}_d is the open circuit voltage of the junction, which at most can be equal to V_d , leading to complete elimination of the build-in electric field.

From equation (6.15) the diffusion potential is described as

$$eV_d = E_{Fn} - E_{Fp}.$$

In order to achieve an optimal diffusion potential the quasi-Fermi energies have to satisfy $E_{Fn} \approx E_C$ and $E_{Fp} \approx E_V$ yielding

$$eV_d \approx E_C - E_V = E_g. \quad (6.16)$$

A large band gap is preferable when a large open-circuit voltage is sought as a consequence. Furthermore it is seen from equation (6.16) that V_d cannot surpass the potential which the band gap gives rise to.[1, p. 368]

6.7 Metal-semiconductor junctions

As the metal-semiconductor interface is of great importance to the efficiency achieved by a solar cell, this section will aim to describe some of the general principles gov-

erning the electronic structure of such an interface. To describe the essential electronic properties of the metal-semiconductor junction the work function of the metal and the electron affinity of the semiconductor is utilized. If a metal and a semiconductor are brought into contact, thermal equilibrium requires that the Fermi energy of the two materials must be aligned.

The situation arising when the two materials are brought together will depend on the work function of the metal and the electron affinity of the semiconductor. As the Fermi levels of the two materials align charge will flow from the material of highest Fermi level to the one of lowest. Thus a dipole layer is built up at the interface. In the metal the charge imbalance is screened by the high density of conduction electrons within a few Angstroms. However, in the semiconductor the lack of free carriers makes the shielding much less effective and the space charge layer can be formed hundreds of Angstroms into the material.

Figure 6.9(a) depicts the situation of aluminum in contact with n-type silicon, where $e\phi_{Al} < e\phi_{Si}$. As a consequence of the n-doping, the Fermi energy lies above the middle of the band gap. In this case the electrons will flow from the aluminum and accumulate in the silicon after contact. In this accumulation layer the downwards band bending is correlated via Poisson's equation, (6.7), with the negative space charge of conduction electrons. This negative space charge is balanced by a corresponding lack of electrons in the aluminum. The same situation for aluminum in contact with p-type silicon is depicted in figure 6.9(b). Due to the p-type doping the work function of the silicon substrate is increased and thus the degree of band bending is increased. The maximum band bending is related to the Schottky barrier, which has to be overcome to excite an electron from the metal to the semiconductor conduction band.[8, p. 377-381]

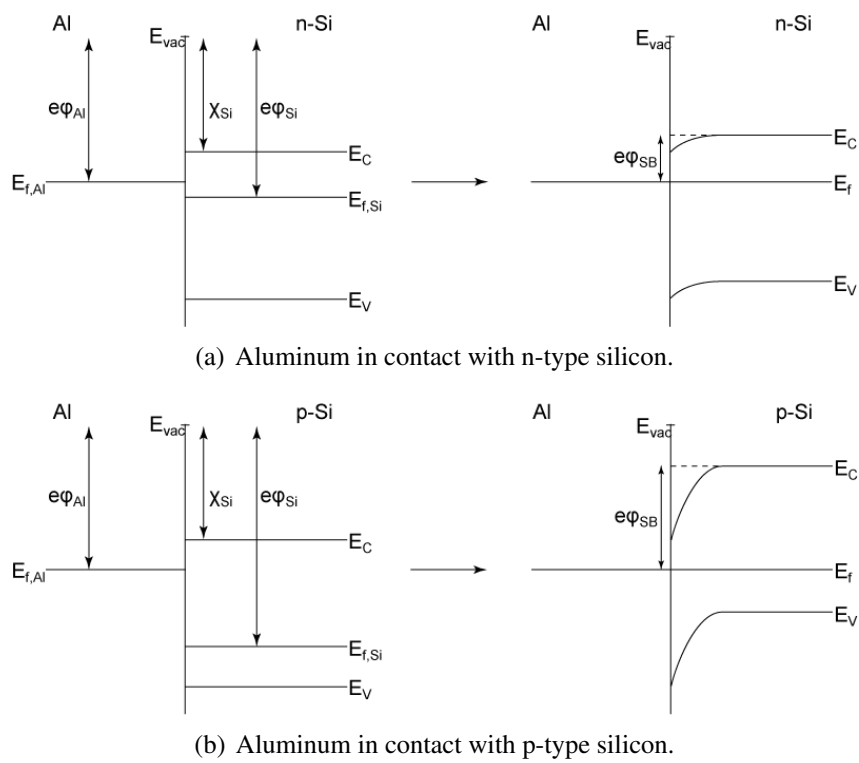


Figure 6.9: Illustrates the diagram of band bending before and after contact. Inspired from [8, p. 380].

Chapter 7

Absorption of Electromagnetic Radiation

In this chapter the absorption coefficient of silicon with the band gap E_g is derived. Furthermore the absorption depth for a range of wavelength is derived utilizing the imaginary part of the refraction index of silicon. Finally, important recombination processes occurring in solar cells is described.

7.1 Absorption coefficient

The output of a solar cell or photo converter is determined by a balance between light absorption, current generation and recombination. The light absorption process will be examined in the following.

Photons with energies higher than that of the energy band gap of a pure semiconductor can cause the excitation of an electron in the valence band into the conduction band leaving a hole behind in the valence band. Thus an electron-hole pair is created due to intrinsic interband absorption.

The absorption coefficient will be calculated using quantum mechanics as the nature of electronic energy bands is quantum mechanical. If transitions of an electron between states of the same or different energy bands are considered the relation between the transition rate and the absorption coefficient can be regarded.

If a beam of electromagnetic radiation with the intensity I is incident on a sample of thickness dx , the absorption coefficient is defined from the equation

$$dI = -I\alpha(\omega)dx,$$

where dI is the change in intensity after the beam has passed through the sample of thickness dx . If the sample has a cross-sectional area A , then $-AdI$ is the rate of the energy absorption in the sample

$$\begin{aligned}\frac{dE}{dt} &= -AdI \\ &= I\alpha(\omega)Adx.\end{aligned}$$

As the energy absorption rate is also given by

$$\frac{dE}{dt} = \hbar\omega W,$$

then the absorption coefficient can be found to be

$$\alpha(\omega) = \frac{\hbar\omega W}{I\Omega}, \quad (7.1)$$

where $\Omega = Adx$ is the volume of the sample and W the transition probability.

The mean value of the poynting vector $\vec{S} = \vec{E} \times \vec{H}$ can be used as a measure of the intensity. The electric field vector \vec{E} and the magnetic field vector \vec{H} can be expressed in terms of the vector potential \vec{A} :

$$\begin{aligned}\vec{E} &= -\frac{\partial\vec{A}}{\partial t} \\ \mu_0\vec{H} &= \nabla \times \vec{A},\end{aligned}$$

when using the Coulomb gauge. If it is assumed that \vec{A} has a standing wave form

$$\vec{A} = \vec{A}_0 \cos(\vec{q} \cdot \vec{r} - \omega t), \quad (7.2)$$

then

$$\begin{aligned}\vec{E} &= -\omega\vec{A}_0 \sin(\vec{q} \cdot \vec{r} - \omega t) \\ \mu_0\vec{H} &= -\vec{q} \times \vec{A}_0 \sin(\vec{q} \cdot \vec{r} - \omega t).\end{aligned}$$

This gives a poynting vector of the form

$$\vec{S} = \frac{\omega}{\mu_0}\vec{A}_0 \times (\vec{q} \times \vec{A}_0 \sin^2(\vec{q} \cdot \vec{r} - \omega t)). \quad (7.3)$$

From vector analysis the identity

$$\vec{A} \times (\vec{B} \times \vec{C}) = (\vec{A} \cdot \vec{C})\vec{B} - (\vec{A} \cdot \vec{B})\vec{C}$$

used in equation (7.3) yields the poynting vector

$$\vec{S} = \frac{\omega}{\mu_0} |\vec{A}_0|^2 \vec{q} \sin^2(\vec{q} \cdot \vec{r} - \omega t),$$

where the orthogonality of \vec{q} and \vec{A}_0 has been used. Neglecting the imaginary part of the refractive index reduces the dielectric function to [1, p. 232]

$$\varepsilon(\omega) = n(\omega)^2,$$

which reduces the dispersion relation in equation (A.21) to

$$q = \frac{\omega}{c} n(\omega).$$

Taking the time average of the magnitude of \vec{S} then yields

$$\langle S \rangle = \frac{\omega^2 n(\omega)}{2\mu_0 c} |\vec{A}_0|^2. \quad (7.4)$$

When inserting equation (7.4) as the intensity in equation (7.1), the absorption coefficient is given as

$$\alpha(\omega) = \frac{2\mu_0 c \hbar W}{\omega n(\omega) |\vec{A}_0|^2 \Omega}. \quad (7.5)$$

7.1.1 Transition probability

To calculate the absorption coefficient the transition probability has to be evaluated. It is assumed that the intensity of the electromagnetic radiation is low enough to allow for the use of perturbation theory to describe the interaction between an electron and the radiation. The Hamiltonian of an electron moving in the radiation field can, in the semi-classical approach, be written as

$$\begin{aligned} H &= \frac{1}{2m} (\vec{p} + e\vec{A})^2 + V(\vec{r}) \\ &= \frac{p^2}{2m} + \frac{e}{2m} (\vec{p} \cdot \vec{A} + \vec{A} \cdot \vec{p}) + \frac{e^2}{2m} \vec{A}^2 + V(\vec{r}), \end{aligned}$$

where \vec{p} is the electron momentum, \vec{A} is the vector potential of the radiation, and $V(\vec{A})$ is the potential energy of the electron. For low intensities the term \vec{A}^2 can be neglected and the interaction Hamiltonian can be written as

$$H = \frac{e}{2m} (\vec{p} \cdot \vec{A} + \vec{A} \cdot \vec{p}). \quad (7.6)$$

As the wave vector \vec{q} of the radiation of interest is much smaller than that of a typical electron, the term arising from the operation of \vec{p} and \vec{A} can be neglected. The interaction Hamiltonian in equation (7.6) is therefore reduced to

$$H = \frac{e}{m} \vec{A} \cdot \vec{p},$$

where \vec{A} is given by equation (7.2)

The time-dependent perturbation theory is now used to derive the transition probability of an electron from a valence band Bloch state $|\vec{k}v\rangle$ to a conduction band Bloch state $|\vec{k}'c\rangle$, which is given by Fermi's golden rule as

$$W(\vec{k}v \rightarrow \vec{k}'c) = \frac{2\pi}{\hbar} \left| \langle \vec{k}'c | H_{int} | \vec{k}v \rangle \right|^2 \delta(E_{\vec{k}'c} - E_{\vec{k}v} - \hbar\omega). \quad (7.7)$$

The interband matrix element of H_{int} for absorption processes is now expressed as

$$\langle \vec{k}'c | H_{int} | \vec{k}v \rangle = \frac{e}{2m} \langle \vec{k}'c | \vec{A}_0 \cdot \vec{p} | \vec{k}, v \rangle \quad (7.8)$$

where the fact that \vec{q} is negligible compared to \vec{k} , thus

$$\vec{k} + \vec{q} \cong \vec{k}. \quad (7.9)$$

Equations (7.8) and (7.9) are put into equation (7.7) and one obtain

$$W(\vec{k}v \rightarrow \vec{k}'c) = \frac{\pi e^2}{2\hbar m^2} |\vec{A}_0|^2 \left| \langle \vec{k}'c | p_{\vec{A}} | \vec{k}v \rangle \right|^2 \delta(E_{\vec{k}'c} - E_{\vec{k}v} - \hbar\omega),$$

where $p_{\vec{A}}$ is the component of \vec{p} in the direction of \vec{A} .

The momentum matrix element is evaluated using the Bloch form

$$\Psi_{\vec{k}}(\vec{r}) = e^{i\vec{k} \cdot \vec{r}} u_{\vec{k}}(\vec{r}),$$

where the periodic function is

$$u_{\vec{k}}(\vec{r}) = \sum_{\vec{G}} C(\vec{k} - \vec{G}) e^{i\vec{G}\cdot\vec{r}},$$

and the quantities $C(\vec{k} - \vec{G})$ are the expansion coefficients, and \vec{G} is reciprocal lattice vectors. The Bloch form is used for the eigenstates $|\vec{k}v\rangle$ and $|\vec{k}'c\rangle$

$$\langle \vec{k}'c | p_{\vec{A}} | \vec{k}v \rangle = \int_{crystal} e^{-i\vec{k}'\cdot\vec{r}} u_{c\vec{k}'}^*(\vec{r}) p_{\vec{A}} e^{i\vec{k}\cdot\vec{r}} u_{v\vec{k}}(\vec{r}) d^3 r.$$

If the crystal is divided into unit cells an alternative expression is obtained

$$\langle \vec{k}'c | p_{\vec{A}} | \vec{k}v \rangle = \sum_{\vec{\ell}} \int_{cell\vec{\ell}} e^{i(\vec{k}-\vec{k}')\cdot\vec{r}} u_{c\vec{k}'}^*(\vec{r}) (ik_{\vec{A}} + p_{\vec{A}}) u_{v\vec{k}}(\vec{r}) d^3 r. \quad (7.10)$$

The periodicity of $u_{n\vec{k}}$ and $p_{\vec{A}}$ is utilized and \vec{r} is set to

$$\vec{r} = \vec{R}(\vec{\ell}) + \vec{\rho},$$

which yields

$$u_{n\vec{k}}(\vec{r}) = u_{n\vec{k}}(\vec{R}(\vec{\ell}) + \vec{\rho}) = u_{n\vec{k}}(\vec{\rho}).$$

Equation (7.10) then reduces to

$$\langle \vec{k}'c | p_{\vec{A}} | \vec{k}v \rangle = \sum_{\vec{\ell}} e^{i(\vec{k}-\vec{k}')\cdot\vec{R}(\vec{\ell})} \int_{cell0} e^{i(\vec{k}-\vec{k}')\cdot\vec{\rho}} u_{c\vec{k}'}^*(\vec{\rho}) (ik_{\vec{A}} + p_{\vec{A}}) u_{v\vec{k}}(\vec{\rho}) d^3 \rho. \quad (7.11)$$

Using the definitions of the lattice vector, reciprocal lattice vector, and the relation between the the primitive translation vectors of the direct and reciprocal lattice [1, p. 3,21,23]:

$$\begin{aligned} \vec{R}(\ell) &\equiv \ell_1 \vec{a}_1 + \ell_2 \vec{a}_2 + \ell_3 \vec{a}_3 \\ \vec{k} &= \frac{m_1}{N_1} \vec{b}_1 + \frac{m_2}{N_2} \vec{b}_2 + \frac{m_3}{N_3} \vec{b}_3 \\ \vec{a}_i \cdot \vec{b}_j &= 2\pi \delta_{ij}, \quad i, j = 1, 2, 3 \end{aligned}$$

the lattice sum in equation (7.11) is found to be $N\delta_{\vec{k},\vec{k}'}$, where N is the number of unit cells. Due to orthogonality between $u_{c\vec{k}}(\rho)$ and $u_{v\vec{k}}(\vec{\rho})$, equation (7.11) reduces to

$$\langle \vec{k}'c | p_{\vec{A}} | \vec{k}v \rangle = N\delta_{\vec{k},\vec{k}'} \int_{cell0} u_{c\vec{k}}^*(\vec{\rho}) p_{\vec{A}} u_{v\vec{k}}(\vec{\rho}) d^3\rho.$$

However, the integral over a unit cell depends only weakly on \vec{k} in a typical semiconductor, and be approximated by a constant. Introducing

$$P = N \int_{cell0} u_{c\vec{k}}^*(\vec{\rho}) p_{\vec{A}} u_{v\vec{k}}(\vec{\rho}) d^3\rho.$$

the transition probability can be written as

$$W(\vec{k}v \rightarrow \vec{k}'c) = \frac{\pi e^2}{2\hbar m^2} |\vec{A}_0|^2 \left| \langle \vec{k}'c | p_{\vec{A}} | \vec{k}v \rangle \right|^2 P^2 \delta(E_{\vec{k}'c} - E_{\vec{k}v} - \hbar\omega) \delta_{\vec{k},\vec{k}'}$$

Due to the Kronecker delta, this expression is only valid for direct or vertical transitions from the valence band to the conduction band. This is illustrated in figure 7.1. If the crystal has a center of inversion, the functions $u_{c\vec{k}}(\rho)$ and $u_{v\vec{k}}(\vec{\rho})$ must have opposite parity to achieve a transition.

To find the total probability of transitions from the valence band to the conduction band, one has to sum $W(\vec{k}v \rightarrow \vec{k}'c)$ over \vec{k} and \vec{k}' , taking the Pauli principle into account

$$\begin{aligned} W_{vc} &= 2 \sum_{\vec{k}} \sum_{\vec{k}'} W(\vec{k}v \rightarrow \vec{k}'c) f_{\vec{k}v} (1 - f_{\vec{k}'c}) \\ &= \frac{e^2 \Omega}{8\pi^2 \hbar m^2} |\vec{A}_0|^2 P^2 \int \delta(E_{\vec{k}c} - E_{\vec{k}v} - \hbar\omega) f_{\vec{k}v} (1 - f_{\vec{k}c}) d^3k, \end{aligned} \quad (7.12)$$

where f is the Fermi-Dirac distribution function from equation (5.1), the factor two is introduced due to spin, and the sum over \vec{k} has been converted to an integral. For the spin-orbit interaction to be taken into account the eigenstates $\vec{k}c$ and $\vec{k}v$ must be labeled with spin indices, and the factor two replaced by a sum over these indices. Also the operator \vec{p} must be replaced by the operator $\vec{\pi}$. [1, p. 237-239]

In the case of $T = 0K$ and spherical, parabolic energy bands, neglecting spin-orbit interaction and degeneracy of the valence band, a two-band model can be utilized with $f_{\vec{k}v} = 1$, $f_{\vec{k}c} = 0$ and

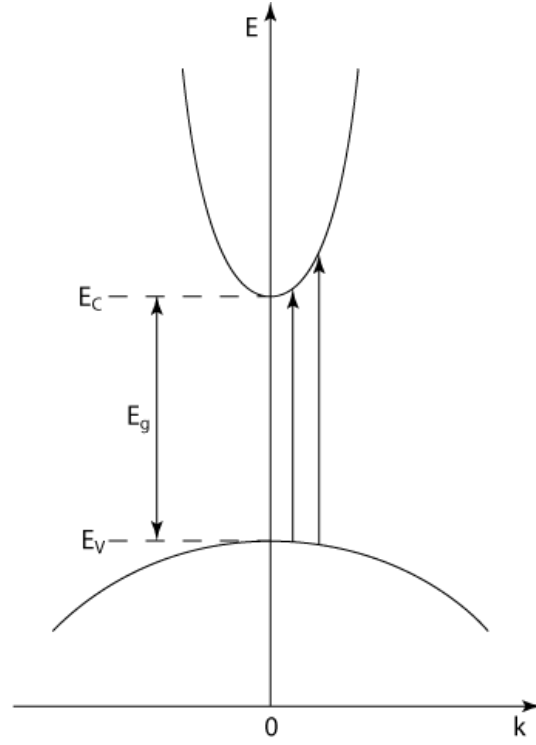


Figure 7.1: Illustrates the direct transitions from the valence band to the conduction band. Inspired from [1, p. 238]

$$\begin{aligned} E_{\vec{k}c} - E_{\vec{k}v} &= E_g + \frac{\hbar^2 k^2}{2m_c^*} + \frac{\hbar^2 k^2}{2m_v^*} \\ &= E_g + \frac{\hbar^2 k^2}{2\bar{m}^*}, \end{aligned}$$

where \bar{m}^* is the reduced effective mass of electrons and holes. With the Fermi-Dirac distribution function for the valence and conduction band in mind, the integral over \vec{k} in equation (7.12) is evaluated in spherical coordinates

$$\begin{aligned} \int \delta(E_{\vec{k}c} - E_{\vec{k}v} - \hbar\omega) d^3k &= 4\pi \int_0^\infty k^2 \delta\left(E_g - \hbar\omega + \frac{\hbar^2 k^2}{2\bar{m}^*}\right) dk \\ &= \begin{cases} 2\pi \left(\frac{2\bar{m}^*}{\hbar^2}\right)^{3/2} \sqrt{\hbar\omega - E_g} & \text{if } \hbar\omega \geq E_g \\ 0 & \text{if } \hbar\omega < E_g. \end{cases} \quad (7.13) \end{aligned}$$

Thus if equations (7.13), (7.12), and (7.5) are combined the result for the absorption coefficient is given as

$$\alpha(\omega) = \begin{cases} \frac{e^2}{2\pi\epsilon_0 c m^2 \omega n(\omega)} \left(\frac{2\bar{m}^*}{\hbar^2}\right)^{3/2} \sqrt{\hbar\omega - E_g} & \text{if } \hbar\omega \geq E_g \\ 0 & \text{if } \hbar\omega < E_g. \end{cases} \quad (7.14)$$

At the conditions of $T = 0\text{K}$ and spherical parabolic energy bands with spin-orbit interaction and degeneracy of the valence band neglected, it is seen from equation (7.14), if the energy of the radiation is less than the energy band gap no radiation is absorbed due to interband transitions. The following relations

$$\begin{aligned}\omega &= \frac{2\pi c}{\lambda}, \\ c &= \frac{1}{\sqrt{\mu_0 \epsilon_0}}, \\ E &= \hbar\omega = \frac{hc}{\lambda},\end{aligned}$$

are utilized in equation (7.14) to derive the absorption coefficient dependency of the wavelength to:

$$\alpha(\lambda) = \begin{cases} \frac{e^2 \mu_0 \lambda}{4\pi^2 m^2 n(\lambda)} \left(\frac{2\bar{m}^*}{\hbar^2} \right)^{3/2} \sqrt{hc \left(\frac{1}{\lambda} - \frac{1}{\lambda_g} \right)} & \text{if } \lambda \leq \lambda_g \\ 0 & \text{if } \lambda > \lambda_g. \end{cases} \quad (7.15)$$

This is illustrated in figure 7.2.

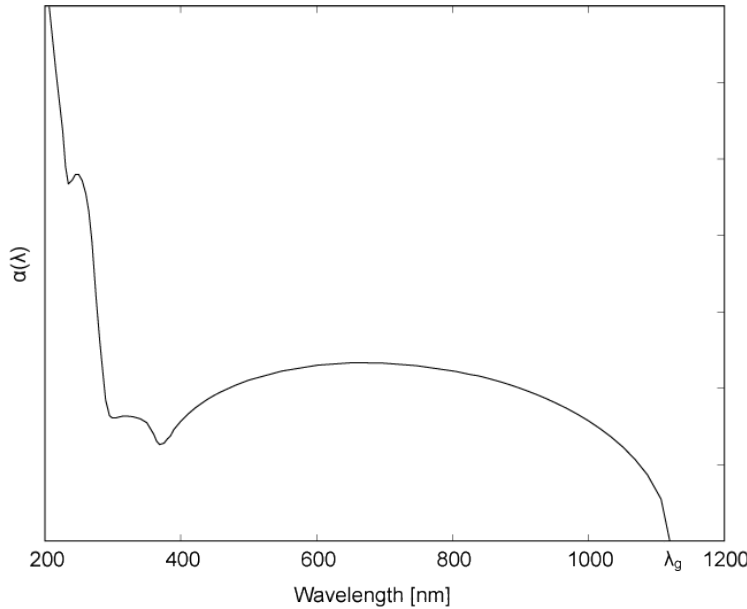


Figure 7.2: Illustration of the absorption coefficient versus wavelength, when the energy band gap is set to 1.17eV, corresponding to a gap wavelength at 1120 nm.

In figure 7.2 the fact, that the energy band gap of 1.17eV is indirect, has not been taken into account. For direct transitions silicon has a band gap of 3.45eV. To utilize the indirect band gap the radiation has to be assisted by a phonon, which lowers the probability of light absorption for silicon with $h\nu < 3.45\text{eV}$.

7.2 Photogeneration

Photogeneration dominates the generation processes of a photovoltaic device under illumination. The process is, however, not the only optical process occurring in a photovoltaic device. Some light may be scattered without being absorbed at all. Some photons may transfer their energy to raise the kinetic energy of already mobile carriers and some may generate phonons, heat, to the system. The rate of the photogeneration is sought in the following.

A slab of thickness x is considered exposed to the light intensity I_o , see figure 7.3.

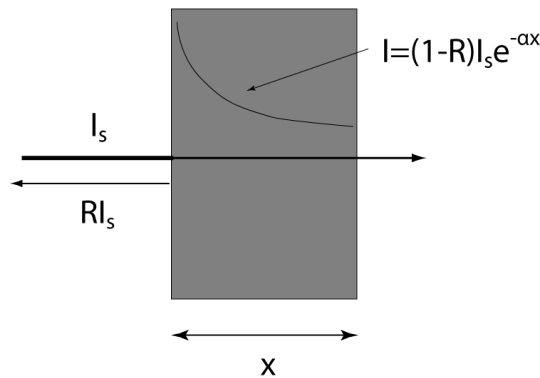


Figure 7.3: A slab of thickness x and absorption coefficient α is exposed from the left to the intensity I_s . A portion is reflected as RI_s , and a portion is exponentially attenuated through the material depicted by the exponentially decaying line drawn. Inspired from [9, p. 89].

As the light intensity passes through the material it is attenuated and this is described using the absorption coefficient α . A ray of photons with energy E and intensity I_s is considered at normal incidence to a surface of a given absorbing material. If it travels an infinitesimal distance dx a fraction $\alpha(E)dx$ of the incident light of energy E is absorbed. The light intensity $I(x)$ is then attenuated by a factor $e^{-\alpha(E)dx}$. The change in intensity over traveled distance in the material is thus

$$\frac{dI}{dx} = -\alpha I.$$

Integrating this over a none uniform α yields

$$I(x) = I(0)e^{-\int_0^x \alpha(E,x')dx'},$$

where $I(0)$ is the intensity just inside of the slab.

If the light travels a distance x the intensity inside the slab is given by Lambert-Beer's Law, α being uniform, as

$$I(x) = I(0)e^{-\alpha x} \quad (7.16)$$

It is now assumed all photons are absorbed by the material generating free carriers. At a distance x below the surface the rate of carrier generation per unit volume is

$$g(E,x) = b(E,x)\alpha(E,x),$$

where $b(E, x)$ is the photon flux at a distance x inside the material. This is, however, an idealized situation and to fully describe the rate of generation reflection at the surface and attenuation in the material must be included. Therefore $g(E, x)$ becomes

$$g(E, x) = (1 - R(E))\alpha(E)b_s(E)e^{-\int_0^x \alpha(E, x')dx'}$$

$b_s(E)$ is the incident flux of photons to the surface and $R(E)$ the reflectivity normal to the surface. The above expression is the so-called spectral photogeneration rate as it includes terms of photonic energy only at E . Finally, in order to find the total rate of generation at a distance x a sum must be made over all photon energies that result in free carrier generation

$$G(x) = \int g(E, x)dE,$$

as these ultimately contributes to the photocurrent. It should be noted that the photogeneration rate does not depend on the energy of the incident photons but the number, as the energy must exceed the band gap. Absorbed photons with $E > E_g$ generate carriers with kinetic energy higher than the band gap but the excess energy is quickly lost by thermalization in the order of picoseconds, see figure 7.4. [9, p. 89]

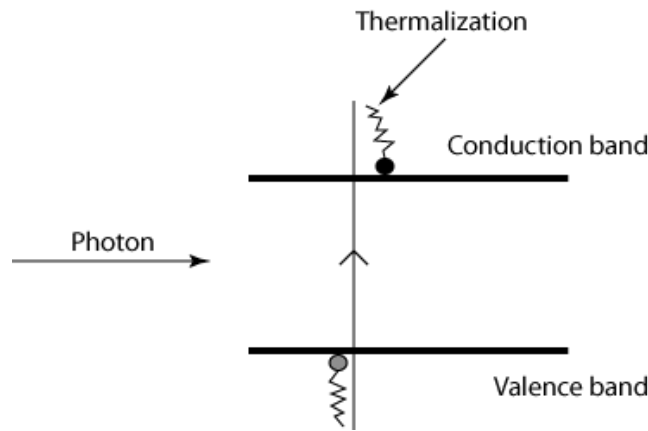


Figure 7.4: Electron-hole pair generated by the absorption of a photon with $E > E_g$. Excess energy is lost by thermalization to the respective band edges. Inspired from [9, p. 90].

7.2.1 Absorption depth

Due to the theory worked out through out this chapter the absorption depth is sought to be derived in this section. From combining equation (7.15) and (7.16), the transmittance of a given wavelength in a given material could be derived. This is, however, not utilized as the absorption coefficient in equation (7.15) does not account for both the direct and indirect band gap of silicon. Instead experimental data from

[5] of the imaginary part of the refractive index will be used for calculations of the transmittance of a given wavelength. This is done to give an estimate of a reasonable junction depth. The electric field of an electromagnetic wave can be written as [7, p. 46]

$$\vec{E} = \vec{E}_0 e^{i(\omega t - \vec{k} \cdot \vec{r} + \varphi)}, \quad (7.17)$$

where E_0 is the amplitude of the electric field, ω is the angular frequency, t is the time, \vec{k} is the wave vector, \vec{r} is the spatial position, and φ is the phase. As it is assumed that the medium does not change in time, the first term of the argument can be excluded. Furthermore the phase is set to zero. Thus equation (7.17) in the z -direction reduces to

$$E = E_0 e^{-ikz}. \quad (7.18)$$

The relations $k = \tilde{n} \frac{\omega}{c}$, $\tilde{n} = n - i\kappa$ [7, p. 68], $\omega = 2\pi\nu$, and $c = \lambda\nu$ used in equation (7.18) yields

$$E = E_0 e^{-i \frac{2\pi}{\lambda} (n - i\kappa) z},$$

where λ is the wavelength and n and κ are the real and imaginary parts of the refractive index of the surrounding medium, respectively. The intensity of the electromagnetic field is

$$I \propto |E|^2 = I_0 e^{-\frac{4\pi}{\lambda} \kappa z},$$

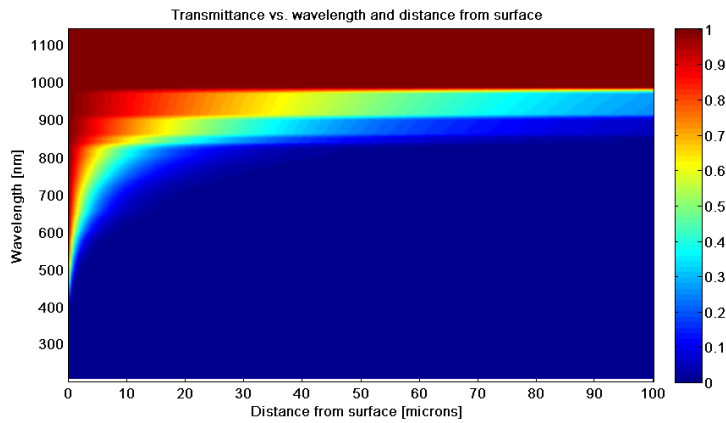
where I_0 is the amplitude of the incoming light. Thus the transmittance is given as

$$T = \frac{I}{I_0} = e^{-\frac{4\pi}{\lambda} \kappa z},$$

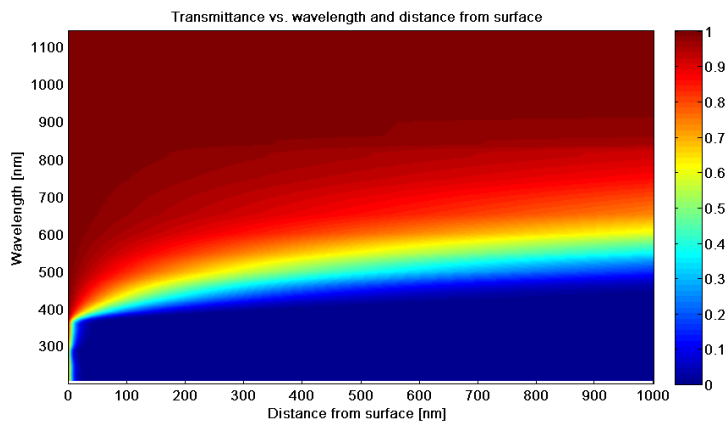
Figures 7.5(a) and 7.5(b) show plots of the transmittance in a slab of silicon as a function of distance from the silicon surface and wavelength. The transmittance is shown in units of $(1 - R)$ cf. figure 7.3

7.3 Recombination processes

Recombination is a process in which the mobile electrons do not contribute to the net photo current but are lost by different removal mechanisms. One distinguishes



(a) 100 μm silicon slab.



(b) 1 μm silicon slab.

Figure 7.5: The transmittance in units of $(1 - R)$ versus the wavelength and distance from surface in two silicon slabs of different thickness.

between unavoidable recombinations and avoidable recombination processes. The latter is called Shockley Read Hall (SRH) recombination and is mainly due to imperfections in the crystal structure, defects, known as trap states. Single crystalline silicon e.g. has less flaws in the crystal structure than poly crystalline and thus fewer trap states. Furthermore metal combined with silicon can give rise to defects and mid gap states which consequently would lower the device performance[3].

As a carrier is captured by a trap state it can subsequently be released by thermal activation. Alternatively, the trap can capture a carrier of opposite polarity to the none released carrier and serve as a recombination providing the trap empty again. Localized states which capture and trap carriers of similar polarity are usually referred to as trap states whereas traps capturing both types of carriers are called recombination centres. These centres usually lie deeper within the band gap as opposed to the trap states which lie closer to the band gap edges. SRH recombination is non-radiative and usually is the dominate loss mechanism.

For a photovoltaic device an unavoidable loss process is radiative recombination or spontaneous emission mentioned in section 8.1.2. The other important recom-

Recombination process is the so-called Auger recombination. Here an electron or a hole can interact with a similar carrier transferring its energy resulting in a decay of one carrier across the band gap and an increase in kinetic energy of the other equal to E_g . The three types of recombination are depicted in figure 7.6.

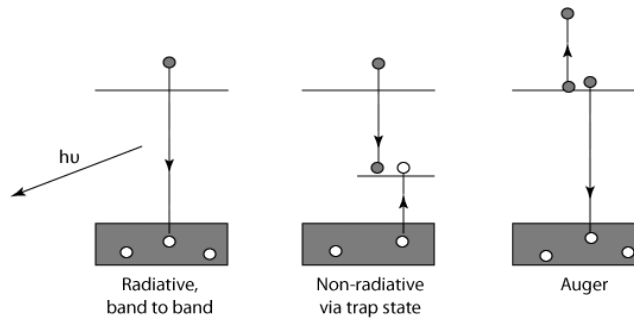


Figure 7.6: Three types of recombination. Radiative band-to-band, non-radiative via trap states and Auger recombination. Inspired from [9, p. 100].

Chapter 8

Solar Cell Characteristics

This chapter deals with the concept of a photovoltaic device and the limitations that arise when converting solar energy into electrical energy. Many factors have more or less impact on the efficiency that can be obtained when converting solar energy.

8.1 Detailed balance

As explained in Section 6.1 excited electrons in the pn-junction need to not recombine to the valence band and must be extracted to an external circuit to obtain a photocurrent. The efficiency by which solar energy is converted to electrical energy, i.e. the photocurrent, in the cell is affected by various limiting factors.

A fundamental physical limitation arises due to the principle of so-called detailed balance. The solar cell does not only absorb solar radiation it also exchanges heat, thermal radiation, with its surroundings. The solar cell and its surroundings radiate long wavelength thermal photons due to their finite temperature. To obtain a constant electron concentration in steady state the cell absorption rate must match that of photon emission.[9, p. 24]

8.1.1 Cell in the Dark

Under no illumination the cell will reach a thermal equilibrium with the ambient, which is assumed to radiate like a black body at a temperature T_a . The flux of photons on the surface of the solar cell at point s can be written using Planck's radiation law as [9, p.18]

$$\beta_a(E, \vec{s}, \theta, \phi) d\Omega \cdot d\vec{S} dE = \frac{2}{h^3 c^2} \left(\frac{E^2}{e^{E/k_B T_a} - 1} \right) d\Omega \cdot d\vec{S} dE,$$

where $d\vec{S}$ is the element of surface area around \vec{s} and $d\Omega$ the unit of solid angle around the direction of emitted light which depends on (θ, ϕ) .

Considering the solar cell as a flat plate the incident flux normal on the surface, assuming the ambient radiation is received over a hemisphere and that the temperature at all points \vec{s} on the surface of the black body is equal, \vec{s} can be excluded, yielding

$$b_a(E) = \frac{2\pi}{h^3 c^2} \left(\frac{E^2}{e^{E/k_B T_a} - 1} \right).$$

The current density due to absorption of ambient radiation can be written as

$$j_{abs}(E) = q(1 - R(E))a(E)b_a(E) \quad (8.1)$$

where $R(E)$ is the probability of photon reflection and $a(E)$ is the probability of absorption of a photon of energy E . It is assumed that each photon of energy E generates one equivalent electron contributing to the current density $j_{abs}(E)$. The quantity $a(E)$ is known as the absorptivity of the cell and depends on the absorption coefficient of the material and the optical path length through it. Finally to obtain the current due to ambient photon absorption equation (8.1) needs to be integrated over the dimensions of the surface of the solar cell.

The solar cell also emits thermal photons by spontaneous emission which is needed to maintain a steady state and thus a constant electronic charge concentration as mentioned above. When the cell is in thermal equilibrium with its surroundings it emits thermal photons characteristic of its finite temperature T_a . The probability of emission of a photon with energy E through the cell's surface is known as its emissivity ϵ . The corresponding current density of the photon emission is then given by

$$j_{rad}(E) = q(1 - R(E))\epsilon(E)b_a(E) \quad (8.2)$$

Comparing the two terms of equation (8.1) and (8.2) the densities j_{abs} and j_{rad} must be equal to maintain the criteria of steady state. This implies that $\epsilon(E) = a(E)$. In other words the rate of absorption must equal the rate of spontaneous emission and is a result of detailed balance. [9, p. 24-26]

8.1.2 Cell under illumination

If the cell is illuminated by a solar photon flux $b_s(E)$ it absorbs photons at a rate

$$(1 - R(E))a(E)b_s(E),$$

where the similarity is seen to that of the rate of ambient absorption in equation (8.1). The corresponding current density due to illumination includes thus both a contribution from thermal and solar photons,

$$j_{abs}(E) = q(1 - R(E))a(E) \left(b_s(E) + \left(1 - \frac{F_s}{F_e} \right) b_a(E) \right)$$

The reducing fraction of $\frac{F_s}{F_e}$ to $b_a(E)$ arises due to a part of the incident ambient flux is replaced by solar radiation.

The solar illumination will excite a part of the electron population of the cell resulting in a raised system chemical potential, $\Delta\mu > 0$. Due to a higher population in the excited state spontaneous emission is increased as a direct consequence with a rate determined by $\Delta\mu$. The spectral flux of photons by a system at temperature T_c and chemical potential μ into a medium of refractive index n_s , using Planck's generalized radiation law, is [9, p.27]

$$\beta(E, s, \theta, \varphi) = \frac{2n_s^2}{h^3 c^2} \frac{E^2}{e^{(E-\Delta\mu)/k_B T_c} - 1} \quad (8.3)$$

By integrating over the solid angle of which photons can escape from the cell and using $n_0 = 1$, air at the surface, equation (8.3) reduces to

$$b_e(E, \Delta\mu) = \frac{2\pi}{h^3 c^2} \frac{E^2}{e^{(E-\Delta\mu)/k_B T_c} - 1}$$

As for the cell in the dark the emissivity is denoted ϵ of the illuminated cell and the current density for photon emission is thus

$$j_{rad}(E) = q(1 - R(E))\epsilon(E)b_e(E, \Delta\mu). \quad (8.4)$$

Studying equation (8.4) it is clearly seen that it reduces to equation (8.2) for the cell in equilibrium with its surroundings in the dark, where $a = \epsilon$ and $\mu > 0$. It is, however, less obvious how $a(E)$ relates to $\epsilon(E)$ when $\Delta\mu > 0$. The equal sign still holds though for a chemical potential that is constant through the device, but will not be shown here. [9, p.28]

To obtain the highest possible net current for a cell under illumination $j_{abs}(E)$ is subtracted from $j_{rad}(E)$, which makes good sense as $j_{rad}(E)$ is a loss in the process. The net current then becomes

$$j_{abs}(E) - j_{rad}(E) = q(1 - R(E))a(E) \left(b_s(E) + \left(1 + \frac{F_s}{F_a} \right) b_a(E) - b_e(E, \Delta\mu) \right) \quad (8.5)$$

To gain a better view on the expression it is divided into two terms. The first concerns the net absorption in excess of that at equilibrium:

$$j_{abs(net)} = q(1 - R(E))a(E) \left(b_s(E) - \frac{F_s}{F_e} b_a(E) \right). \quad (8.6)$$

The term to the right of the equal sign before the large brackets is simply the repeating one in all the densities from earlier calculated. In the large brackets the first term is the flux of solar photons and the second is the fraction of thermal photons that have been replaced by solar photons.

The second contributing term of equation (8.5) is the net emission also called the radiative recombination current density,

$$j_{rad(net)}(E) = q(1 - R(E))a(E)[b_e(E, \Delta\mu) - b_e(E, 0)]$$

where $b_a(E) = b_e(E, 0)$ as the chemical potential would be zero. The term in square brackets accounts for the difference between the radiation of a surface with $\Delta\mu > 0$ to that of the incident flux of thermal photons normal to the surface.

The radiative recombination in the cell is an unavoidable loss process that lowers the efficiency of the cell as the solar energy absorbed cannot be fully converted into electrical energy and i.e. fed to an external circuit. [9, p. 26-28]

8.2 Characteristics of a solar cell

In the previous section the radiative recombination was found to be accounting for lowering the maximum efficiency of converting solar rays into electrical energy. With the knowledge outlined, however, the absolute limiting efficiency can be calculated. A simple two-band system is considered where the ground state is completely filled and the excited is empty, see figure 8.1.

The two bands are separated by a band gap E_g , where the promotion of an electron to the excited state cannot occur for an incident solar quantum with $E < E_g$. It is furthermore assumed that the electrons in each band are in a quasi thermal equilibrium at a temperature T_a from the surroundings and the chemical potential of the i 'th band is μ_i .

8.2.1 Short circuit current

As the solar cell is under illumination it absorbs a net flux of photons that excite some of the electron population. Due to the field at the pn-junction the electrons are separated from their holes and can thus be fed to an external circuit creating a photocurrent. The angular range of the sun compared to the ambient is negligible and therefore the second term $\frac{F_s}{F_e} b_a(E)$ in equation (8.6) can be excluded without violation.

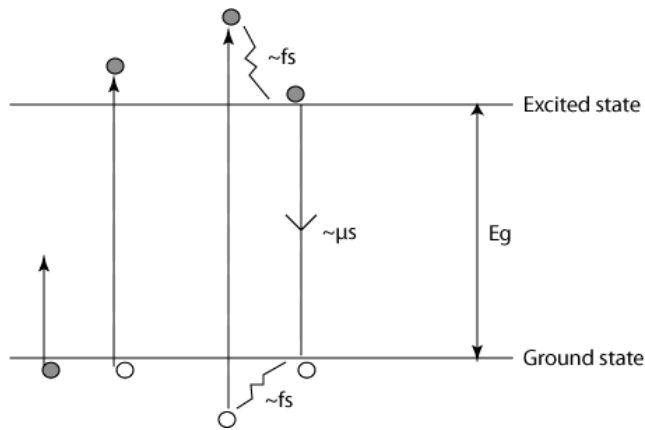


Figure 8.1: A two band system with an energy gap of E_g . Photons with $E \geq E_g$ promote electrons to the excited state but for $E \gg E_g$ excess energy is quickly lost as heat to the system as the carriers relax to the band edges. Inspired from [9, p. 29]

An expression for the photocurrent density in a circuit can be obtained by integrating j_{abs} from equation (8.6) over all photon energies. Furthermore the probability of collecting an excited electron to the circuit is introduced as $\eta_c(E)$ which yields the short circuit current density

$$J_{sc} = q \int_0^{\infty} \eta_c(E)(1 - R(E))a(E)b_s(E)dE.$$

In the ideal case of a maximum efficient solar cell it is assumed that the material is perfectly absorbing, non-reflecting so each photon with $E > E_g$ contributes to the promotion of exactly one electron to the upper excited state. Radiative recombination cannot be neglected, however, and is an unavoidable loss. The remaining electrons are assumed to be perfectly separated from their holes and thus collected by the negative terminal of the cell, $\eta_c(E) = 1$. Using the above assumptions and utilizing

$$a(E) = \begin{cases} 1 & E \geq E_g \\ 0 & E < E_g \end{cases},$$

the maximum photocurrent for the particular band gap can be reduced to the expression

$$J_{sc} = q \int_{E_g}^{\infty} b_s(E)dE.$$

The photocurrent is now only a function of the size of the band gap and the incident solar spectrum. It is clear that J_{sc} will increase as E_g decreases and in order to determine the actual efficiency of conversion the spectrum must be defined.

8.2.2 Open circuit voltage

Applying a bias over the cell in the dark results in a so-called dark current that flows through the device. The dark current acts in the opposite direction of the photocurrent and lowers the net current. The $J(V)$ characteristic can be written as

$$J(V) = J_{sc} - J_{dark}(V),$$

as J is a function of applied potential.

Most solar cells behave like diodes in the dark and the reverse current density has the form $J_{dark}(V) = J_0(e^{qV/k_B T} - 1)$, where J_0 is a temperature dependent constant. The term qV is the chemical potential $\Delta\mu$ of the cell, assuming the material is ideal with lossless carrier transport. As the cell is illuminated by solar photons there is a contribution from the photocurrent and reverse current due to applied bias. The reverse current in the dark compared to that under illumination, however, is not formally equal, but for many photovoltaic materials they are approximately identical and the $J(V)$ characteristic still holds as

$$J(V) = J_{sc} - J_0(e^{qV/k_B T} - 1). \quad (8.7)$$

The open circuit voltage V_{oc} is the maximum value the potential difference can reach. This is achieved when the contacts are isolated, where the dark current and the short circuit photocurrent cancel out. Thus from equation (8.7) V_{oc} is

$$\begin{aligned} 0 &= J_{sc} - J_0(e^{\frac{qV_{oc}}{k_B T}} - 1) \\ V_{oc} &= \frac{k_B T}{q} \ln\left(\frac{J_{sc}}{J_0}\right). \end{aligned} \quad (8.8)$$

According to equation (8.8) the open circuit voltage increases logarithmically with the light intensity. The point V_{oc} is shown in figure 8.2, from which it also can be seen, that for $V < 0$ the cell consumes power to generate a photocurrent, for $0 < V < V_{oc}$ the cell creates power, and for $V > V_{oc}$ the cell is power consuming again. [9, p. 10-11+30-31]

8.2.3 Parasitic resistances

In a real solar cell the contact between metal and semiconducting material and the fact that current leaks around the sides of the device acts as resistances. Electrically this corresponds to a shunt resistance in parallel and a resistance in series with the cell, which is illustrated in figure 8.3.

The series resistance arises due to the resistance of the cell material and the contacts. A large series resistance is problematic for high current densities. Optimally the series resistance is to be as low as possible. The shunt resistance arises due to leakage of current through the cell, around the edges of the device and between

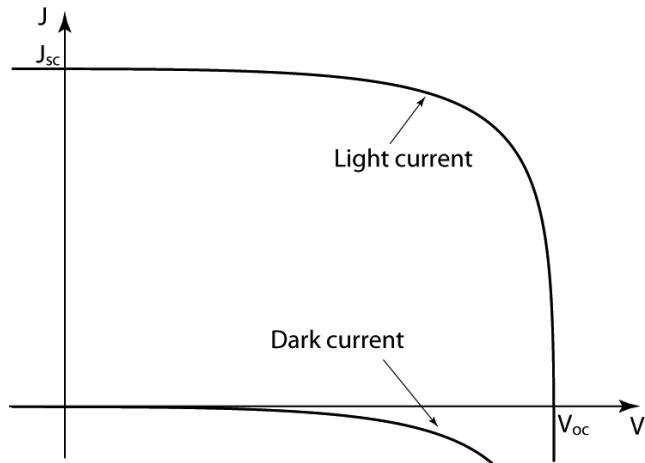


Figure 8.2: I-V characteristic of an ideal diode under illumination and in the dark. Inspired from [9, p.10]

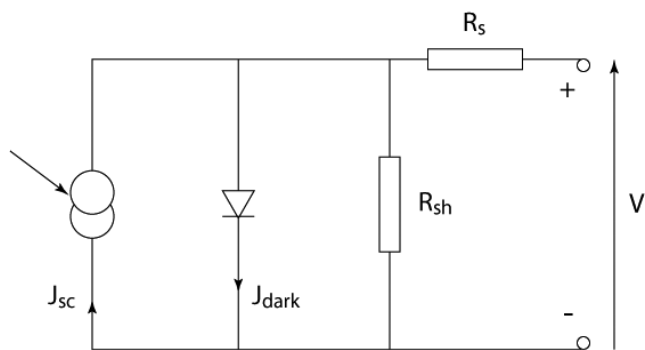


Figure 8.3: Illustrates a circuit model of a solar cell. Inspired from [9, p. 14].

contacts of different polarity. The shunt resistance should be as high as possible. If the parasitic resistances are included the diode equation from equation (8.7) is modified to [9, p.14]

$$J = J_{sc} - J_0 \left(e^{q(V+JAR_s)/k_B T} - 1 \right) - \frac{V + JAR_s}{R_{sh}}$$

Here A is the surface area of which J passes through. The effect of increasing series resistance and decreasing shunt resistance on an I-V curve is shown in figure 8.4.

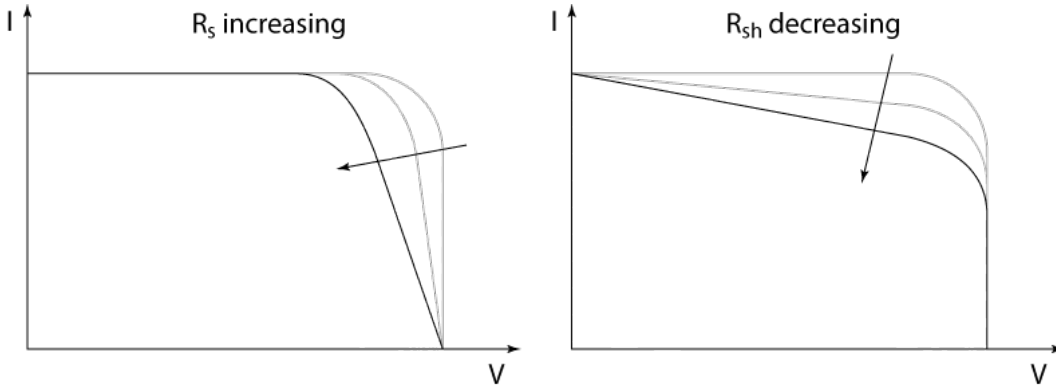


Figure 8.4: I-V characteristic of a solar cell where a decrease in shunt resistance and an increase in series resistance lowers the total output of the cell. Inspired from [9, p.14].

8.3 Efficiency

As described in Section 8.2.2 a solar cell delivers power in the range of bias from 0 to V_{oc} . The power density can be written as

$$P = JV \tag{8.9}$$

The maximum efficiency is reached at a voltage V_m with a corresponding current density J_m . The fill factor FF describing the squareness of the J-V curve is defined as

$$FF = \frac{J_m V_m}{J_{sc} V_{oc}} \tag{8.10}$$

In figure 8.5 V_m, V_{oc}, J_m, J_{sc} are shown, where the area of the inner and outer rectangle is drawn by $V_m \times J_m$ and $V_{oc} \times J_{sc}$, respectively. Thus the fill factor is illustrated by the ratio between the inner and outer rectangle. The efficiency of a cell is given as a fraction of the maximum power density delivered by the cell to the incident light power density

$$\eta = \frac{P_m}{P_s} = \frac{J_m V_m}{P_s} = \frac{J_{sc} V_{oc} FF}{P_s}$$

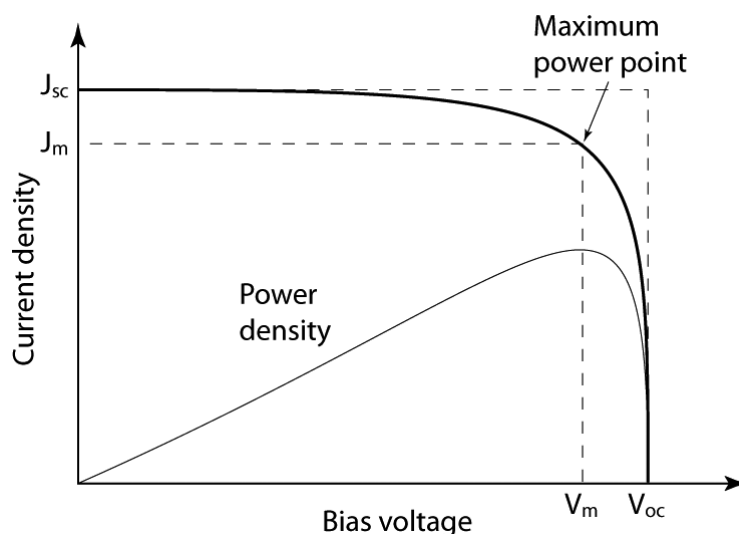


Figure 8.5: Current-voltage (thick) and power-voltage (narrow) characteristics of an ideal cell. The maximum power density occurs at maximum bias V_m . It can be calculated by multiplying J_m and V_m and is also given by the area of the inner rectangle. The outer rectangle has the area $J_{sc} \times V_{oc}$. A fill factor FF of 1 would equal the extreme case of the current voltage curve following the outer rectangle. Inspired from [9, p.12].

where equations (8.9) and (8.10) have been used. V_{oc} , J_{sc} , FF , and η are the four key characteristics of a solar cell, and should be determined for particular illumination conditions.

As a consequence maximum efficiency must be achieved when

$$\frac{d(J(V)V)}{dV} = 0.$$

In the simplified case in the above theory outlined, the efficiency of the two band photo converter is only a function of the band gap E_g and the incident spectrum. Furthermore the power conversion efficiency η is a function of only the band gap size if the incident spectrum is fixed. In this situation it is seen that very small and very large band gaps make poor photo converters. In the first situation a very small band gap leads to a low working value of V because V_m is always less than E_g . In the latter case the majority of incident photons do not have enough energy to promote the electrons from the lower band resulting in a poor photocurrent.

The efficiency versus band gap calculated from a standard solar spectrum is shown in figure 8.6 with a maximum of 33% at an E_g of 1.4eV. From [9, p. 33]

Typical material compounds possessing these high efficiencies are gallium arsenide and indium phosphide due to their band gaps lying close to the optimum value. These compounds, however, are expensive compared to the much more abundant silicon based solar cells with a band gap at 1.17eV. This value is not favourable for high efficiency cells and an efficiency of app. 29% has been achieved as a high efficiency value. [9, p. 36]

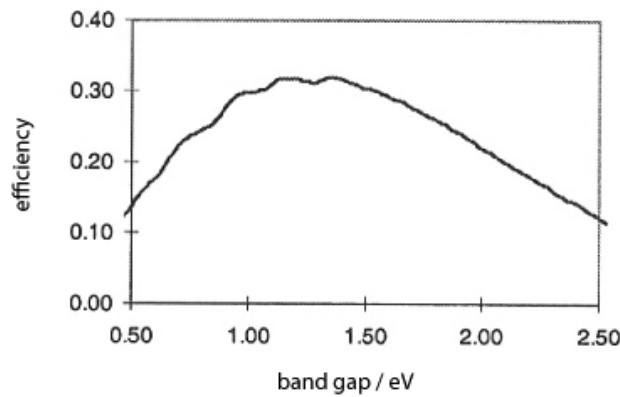


Figure 8.6: Efficiency versus band gap size calculated for a standard solar spectrum. Maximum of 33% at an E_g around 1.4eV . From [9, p. 33]

8.3.1 Spectrum influence on efficiency

In order to determine the effect the incident spectrum has on the efficiency of the photo conversion a representative model is used. The sun is replaced with a black body at temperature $T_s=5760\text{K}$ as illuminating source. This model predicts a limiting efficiency of around 31% at a band gap of 1.3eV , calculated by [9, p. 34]. If the radiating source red shifts its spectrum it results in lower energy radiated and overall it decreases the optimum band gap and the limiting efficiency. In the extreme case of $T_s = T_a$, where T_a is the cell temperature, the cell is in thermal equilibrium with the source and no net photo conversion occurs. Raising the temperature of the source relatively to the cell increases the efficiency as a direct consequence. If $T_a \rightarrow 0$ the cell does not experience any radiative recombination as the spontaneous emission has vanished at this extremum.

With this assumption and if all carriers are collected to the external circuit contributing with $\Delta\mu = qV$ the maximum efficiency is given by

$$\eta = \frac{E_g \int_0^\infty b_s(E) dE}{\int_0^\infty E b_s(E) dE}.$$

The term in the top of the fraction accounts for the energy that is absorbed above E_g and the bottom of the fraction is simply all incident energy. The theoretical maximum has been reported by Shockley and Queisser [9, p. 35] to around 44% with a band gap at 2.2eV and a modelled black body sun at 6000K . This value is calculated to be the ultimate efficiency to be obtained from a photovoltaic device. However, cooling down the cell requires energy which again reduces the net efficiency.

Another method to improve the efficiency is to concentrate the solar rays that hit the surface of the cell. The angular range subtended by the sun is focused onto the cell surface resulting in a larger absorbed flux yielding a larger photocurrent. The cell emits radiation in all directions but only absorbs in a narrow angular range from the sun. A result of increasing the angular range is a more effective balance between the two contributions to the photocurrent.

To summarize, a lot of limitations decrease the maximum efficiency that can be obtained by the solar cell. Incomplete absorption of incident light due to reflection at the surface and furthermore some light travels through the device which reduces the photocurrent. Excited electrons can be trapped at defect sites as the crystal structure of the material is not perfect and recombine before being collected to the external circuit.[9, p. 35]

Chapter 9

Solar Cell Fabrication

This chapter contains the fabrication methods utilized to construct the silicon solar cells. Phosphorus is screen printed on p-type multi crystalline silicon and phosphorus is deposited using a spin-on method.

The solar cells to be constructed are all based on p-type polycrystalline silicon with a resistivity of 1,8-4,5 Ω cm and a thickness of 750 μ m. Furthermore substrates of 15-20 Ω cm have been used for examination. The general structure of a cell consists of four layers. The top layer is an aluminum contact with a designed pattern that allows radiation to reach the two layers below containing the pn-junction. According to figure 7.5 an ideal junction depth should lie in the range between app. 200-400nm for the depletion layer to lie in the vicinity of a relatively high absorption. However, the junction cannot be too shallow as defects near the surface give rise to recombination centres. Finally the bottom layer consist of an aluminum backside contact. See figure 9.1 for schematic setup of the four layers.

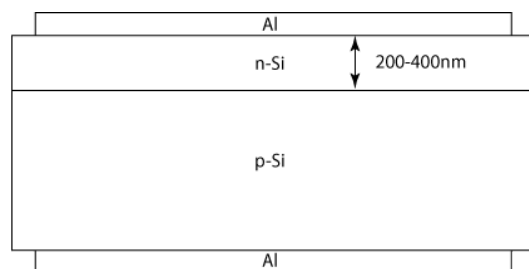


Figure 9.1: Illustrates the four basic layers of the solar cells fabricated.

9.1 pn-junction formation

In order to construct a solar cell a pn-junction needs to be formed inside a semi-conducting material. The intrinsic property of a band gap in the semiconducting material is needed for the generation of electron-hole pairs that are created under

illumination, see section 6. The pn-junction formation was conducted by the diffusion of phosphorus into the above mentioned p-type silicon substrates. Two methods were used for adding the phosphorus paste onto the silicon substrates.

9.1.1 Phosphorus application onto p-type silicon

The first method utilized a screen-printing technique in which a stainless steel mesh (Fe/Cr18/Ni10/Mo3), 180 mesh per inch from Advent Research Materials Ltd, was used. The mesh was fixed in a metal frame depicted in figure 9.2.



Figure 9.2: Illustrates the steel mesh to the left and the platform rack to the right on which the substrates are placed.

The screen printing setup was constructed for the application of 1x1 or 1x2cm silicon substrates, which were placed onto either a 1x1 or 1x2cm platform. The steel mesh was placed on top of the substrates with a distance of 1-2mm to enable the adding of phosphorus screen printing paste (Filmtronics) onto the silicon, see figure 9.3 for application setup.

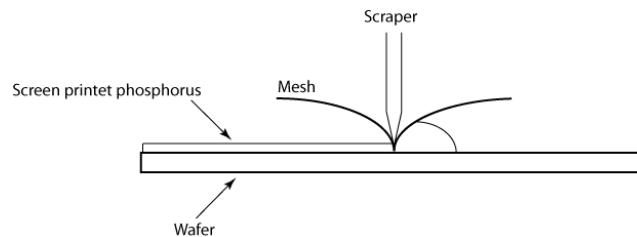


Figure 9.3: Illustrates the application of phosphorus using the screen printing technique.

The phosphorus was added by pouring down a droplet at one end of the mesh and then scraped over the mesh to cover the silicon substrate entirely. The amount of paste added on the substrate depended on the pressure at which the paste was scraped and was not entirely consistent. After the application of phosphorus the substrates were heated on a plate for 15min at 150°C.

A spin-on method was utilized as well for the application of a spin-on phosphorus paste on the silicon substrates as it allowed for examining the effect of varying the paste thickness. After spin-on the substrates were heated for one minute at 200°C. Furthermore the screen print phosphorus was also used in the spin-on experiments to examine the possible effects of such. These samples were heated as in the screen print experiment at 150°C for 15min.

The advantage of screen printing is a somewhat uniform layer thickness of phosphorus opposed to the spin-on method which gives rise to an uneven layer thickness on the substrate at particular points.

9.1.2 Drive-in

The silicon substrates were annealed in two different furnaces after phosphorus application, see figure 9.4 for a diffusion profile for a dopant into an arbitrary substrate.

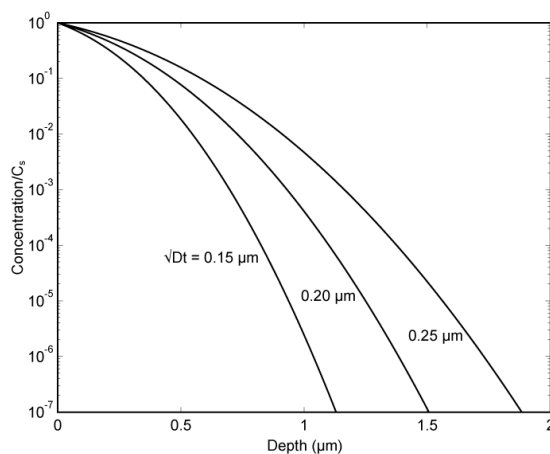


Figure 9.4: Illustrates the diffusion length for various diffusion times \sqrt{Dt} in the assumption of unlimited dopant source at the surface of the substrate.

The first method utilized a carbolithe furnace in which the samples were annealed at app. 950°C at air for various annealing times. This method did not allow for control of the atmosphere in which the samples were annealed.

The second method of annealing was carried out in a quartz tube furnace at temperatures of 1000-1050°C and at various annealing times. The QTF allowed for the use of different atmospheres during the annealing process. Experiments were conducted with no flow present where the samples were at air, and with the flow of dry air. Dry air was used as the phosphorus paste was manufactured to be used with this specific atmosphere.

9.2 Contacts

Firstly the oxide layer formed from the drive-in process had to be removed, which was done in hydrofluoric acid. The front and backside contacts on the solar cells were fabricated followingly using two different techniques. The first approach utilized photolithography where a positive photoresist of the type ma-P 1205 was spun at 1000 rpm onto the top n-type layer and dried at two minutes at 120°C on a hot plate. A mask is put on top of the resist, see figure 9.5, and the positive resist is exposed to uv-radiation for one minute at 32W in order to form a contact pattern that allows for light to reach the active solar cell area. The exposed resist on the

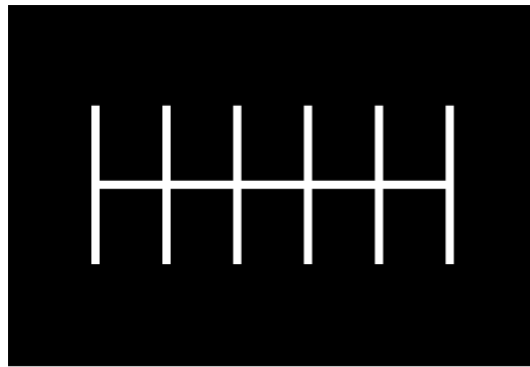


Figure 9.5: Front contact mask

substrate is then removed using a photoresist developer type ma-D 331.

Afterwards app. 200nm aluminum was sputtered on as conductor. The layer was formed in a sputter coater at a vacuum of $8\text{-}9\cdot 10^{-6}$ mbar. Finally lift-off is executed in an ultra sound bath of acetone. The backside pattern was constructed similarly in order to cover the whole backside of the solar cell with aluminum but leave one millimeter unexposed along each side to avoid short circuiting from the front side to the backside contacts. In addition the solar cells were polished along the sides with fine sandpaper as the sputtering process would leave aluminum on the sides of the wafer which increases the risk of contacting the wrong layers. However, this treatment was not consistent to prove that the aluminum at the sides had vanished completely.

To avoid the issue of short circuit along the sides due to aluminum a metal mask was constructed to cover the substrates with contact patterns, see figure 9.6. Furthermore after the spin-on process the phosphorus tended to accumulate to a cer-

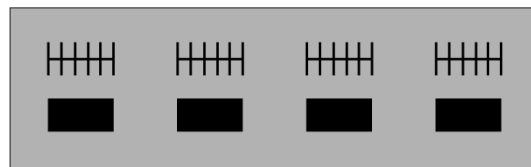


Figure 9.6: Metal mask with contact patterns for front and backside.

tain extent on the sides of the wafers resulting in a short circuit between the n-side

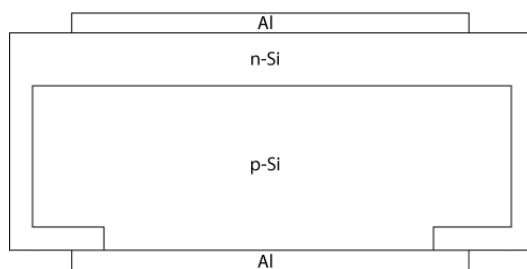


Figure 9.7: Illustrates the solar cell with the n-type layer short circuited to the backside contact due to phosphorus accumulating at the sides of the substrates after the spin-on process.

and the backside contact, see figure 9.7. The ideal situation of the separation of the four basic layers is depicted in figure 9.1.

To try and resolve this issue Reactive Ion Etching was used to separate the n-side layer from the backside contact, see figure 9.8. This was done by firstly spinning on a photo resist on the substrates after the hydrogen termination process. The

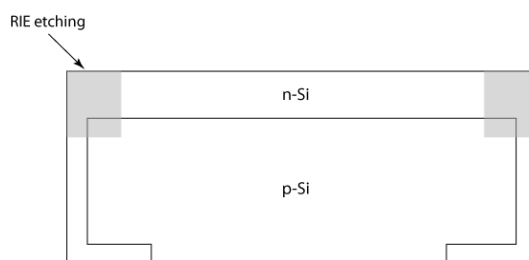


Figure 9.8: Illustrates the concept of the RIE process where the n-type layer is separated from the back side contact to prevent short circuiting the solar cell.

substrates were heated on a hot plate for two minutes at 120°C. Afterwards the substrates were exposed to uv-radiation for 80sec at 32W using a mask that left 2mm along each side of the substrate exposed. The substrates were developed as in section 9.2 leaving 2mm along each side of the substrate prepared for the RIE-etching. The etching depth was hence examined in a profiler to app. 4μm, which succeeds the depth of the n-doped layer.

Chapter 10

Characterization Methods

This chapter presents the different characterization methods used to study the fabricated solar cells from Chapter 9.

10.1 Sheet resistance

Sheet resistance measurements were conducted after the oxygen removal process described in section 9.2. The technique is simple and gives a direct estimate of the dopant concentration in the substrate and also how far from the surface the junction is located. A high sheet resistance results in a low dopant concentration and a shallow junction level and vice versa. The experimental theory can be seen in section 4.2 where the collinear four point probe approach is utilized, see figure 10.1.

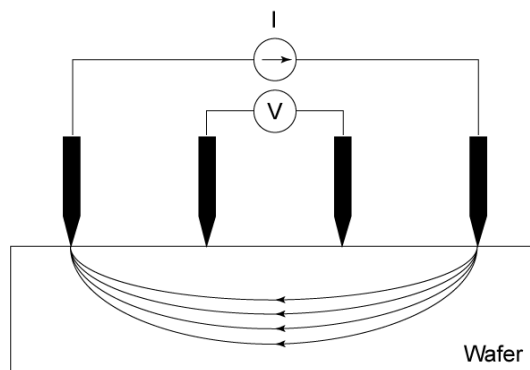


Figure 10.1: Collinear four point probe approach utilized to determine the sheet resistance.

10.2 Diode characterization

The various solar cells fabricated in chapter 9 were studied by determining their diode characteristics. This was done to study if the solar cell acts as a diode and rectifies the current in one direction, at forward bias, and cuts off at reverse bias. This property is imperative in order to have a functioning solar cell. At reverse bias, with a negative voltage applied to the p-region and a positive voltage to the n-region, it results in a potential difference increase between the two regions. As a result practically no electrons can climb the potential barrier from the p-side to the n-side. The potential is depicted in figure 6.5 in thermic equilibrium under no applied bias. At forward bias the potential energy barrier is lowered between the n and -p side enabling more electrons to flow from the n side to the p side region.

The experimental setup is shown in figure 10.2, where the variable resistor allows for the setup to sweep the voltage over the cell and gain the corresponding current. At first a measurement was conducted under no illumination and followingly with

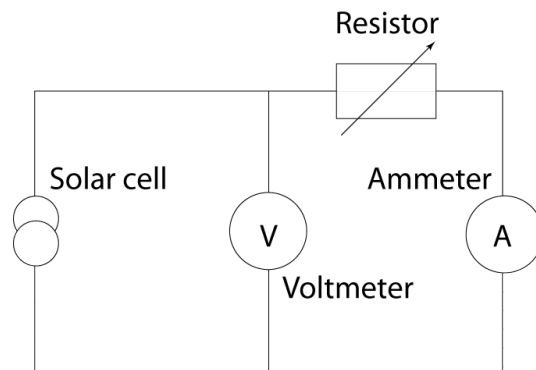


Figure 10.2: Illustrates the solar cell in a closed circuit utilizing a variable resistor to sweep the voltage in a desired range.

the cell illuminated by an arbitrary light source to indicate a possible light response of the photovoltaic device. The voltage sweeps ranged from -1V to +1V and -4V to +4 for specific cells. The deviation in voltage is due to overload occurring while measuring on some of the cells and voltage hence had to be lowered to gain useful I-V curves.

An example of a diode characteristic is depicted in figure 10.3 for sample O8 in table B.2 with a voltage sweep from -1V to +1V.

The characteristic rectifying behaviour of the current is seen as the diode only lets current flow in one direction under applied voltage. Furthermore a zoom in on sample O8 is shown in figure 10.4 where the cell now produces a positive current due illumination of the solar cell.

10.3 I-V characterization and cell efficiency

The solar cells were studied with an Endeas Quicksun setup with the solar cell in a similar circuit to the one used in the diode characterization. The setup is depicted in

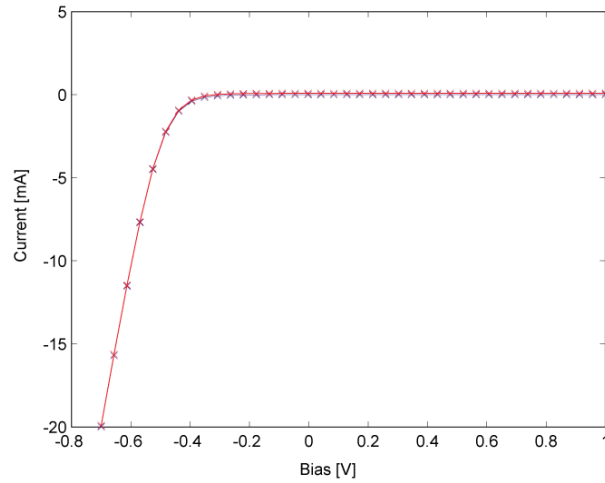


Figure 10.3: Diode characteristic of sample O8 from -1V to +1V. The rectifying behavior of the current is observed as the diode only lets current flow in one direction.

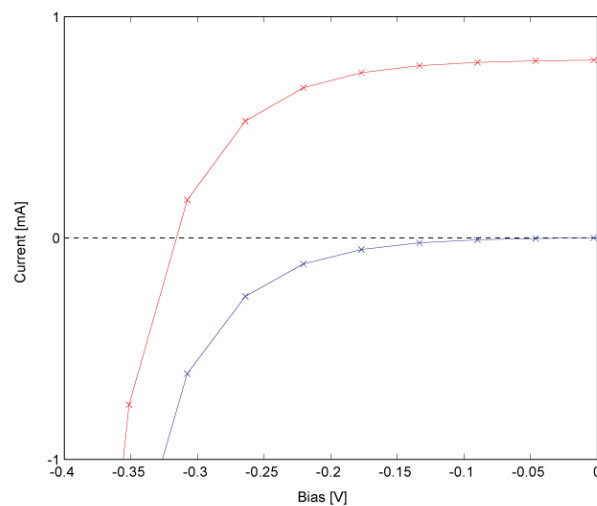


Figure 10.4: Illustrates a zoom in on sample O8 where the current rises above zero due to the irradiation of light at the solar cell surface. The cell hence produces power.

figure 10.5, where a xenon flash is utilized as the illuminating source with an effect of $1200\text{W}/\text{m}^2$. The spectrum of the xenon lamp approximately resembles that of the

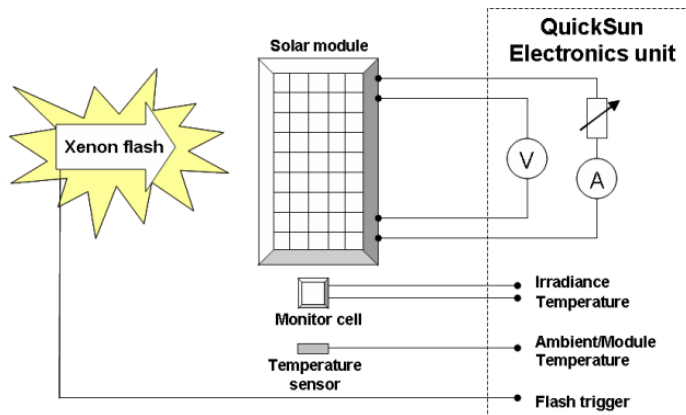


Figure 10.5: Illustrates the solar cell in series with a variable resistor and ammeter and in parallel with a voltmeter, used in the efficiency measurement setup. [10]

sun, see figure 10.6, and to a certain extent this indicates how the solar cell would operate under solar illumination.

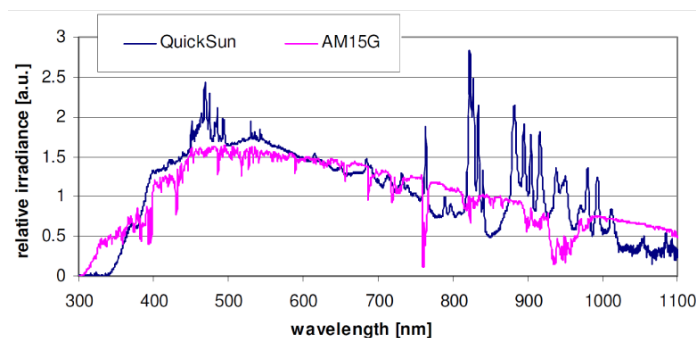


Figure 10.6: Spectrum of the artificial light source used as illuminator during I-V characteristics. The spectrum resembles that of the sun to a certain extent and therefore indicates how the solar cell operates under solar illumination. [10]

The solar cell is in series with an ammeter and in parallel with a voltmeter and current voltage characteristics is measured by sweeping from open circuit to short circuit while measuring the voltage current output. This output yields the I-V characteristic of the specific cell and the quantities I_{sc} , V_{oc} , and the fill factor FF , outlined in section 8.3. To determine the efficiency of the solar cell the irradiance of the flash is measured at a monitor cell and a computer program calculates the effect of the light flash arriving at the cell surface. The maximum power created by the solar cell is determined by utilizing the quantities V_m and I_m in $P_m = I_m \cdot V_m$. The efficiency is thus calculated by the ratio between the maximum power delivered by the cell to the incident light power, $\eta = P_m/P_s$.

The I-V curve of a fabricated solar cell, sample O8 in table B.2, is shown in figure 10.7

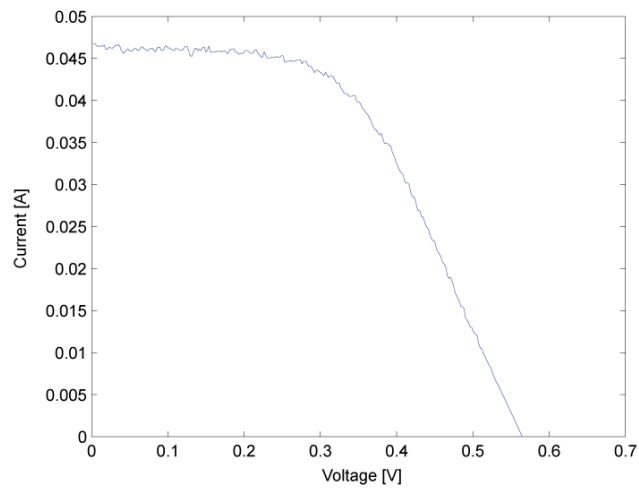


Figure 10.7: Illustrates the I-V curve of sample O8 in table B.2

The I-V curve gives information about the shunt and series resistances that governs the specific solar cell, as outlined in section 8.2.3. This information can be utilized to establish whether the solar cell has contact problems i.e. a high series resistance which is a problem at high current densities. Additionally it yields information about the leakage current or shunt resistance in the cell that is a problem in poorly rectifying devices. [9, p. 13-14]

Chapter 11

Results

In this chapter the characteristics of the solar cells, achieved by sheet resistance-, I-V-, and diode-measurements, are studied. These characteristics are discussed and possible improvements are conducted. The experiments are presented chronologically.

11.1 Drive-in atmosphere

By manufacture prescription, except for the paste application technique, four samples were fabricated varying the spin-on speed between 1k and 2k rpm and drive-in time between 1.5min and 3min. As explained in section 9.1.2 drive in of spin-on screen print phosphorus was at first conducted in a carbolithe furnace at app. 950°C at air. A 1% HF acid was used for oxide removal for 30sec before contacts were fabricated using photolithography described in section 9.2.

The diode characteristic of sample A2 spun at 1k rpm and a drive-in time of 1.5min is shown in figure 11.1. Note that the red curve is due to illumination of the solar cell using a microscope lamp to investigate a photovoltaic response and the blue curve is the dark current. If only a red curve has been displayed, this is for the illuminated solar cell. It is seen that the solar cell exhibits some rectifying diode behavior, however, the insufficient current implies an issue with the series resistance of the solar cell. The corresponding I-V curve from the efficiency measurement is shown in figure 11.2, with an efficiency $\eta = 0.1\%$. The efficiency has been measured for the total area of the solar cell top surface, thus the area covered by the front contact has not been accounted for in the efficiency calculations. This is consistent for all efficiency measurements.

As the dopant paste originally was fabricated to be utilized in a combination with a mesh screen at app. 200-400 mesh per inch, the issue could lie in a deviating paste thickness according to supplier prescription.

Samples B1-B4 were fabricated using the same conditions as in the above and in order to apply a proper amount of dopant onto the substrates a mesh frame was constructed, as outlined in section 9.1.1. However, the diode characteristics obtained

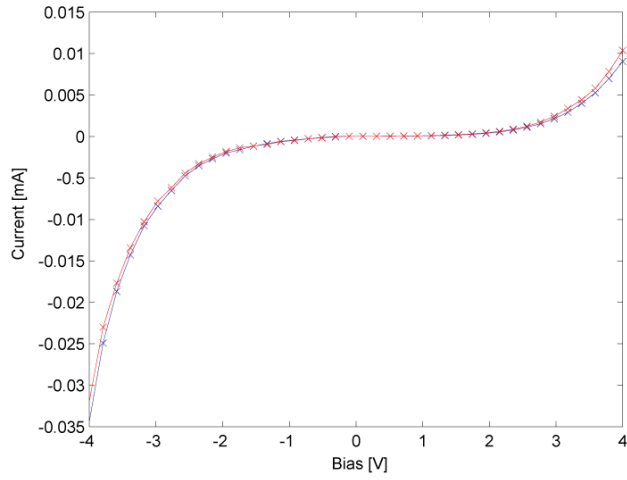


Figure 11.1: Diode characteristic of sample A2.

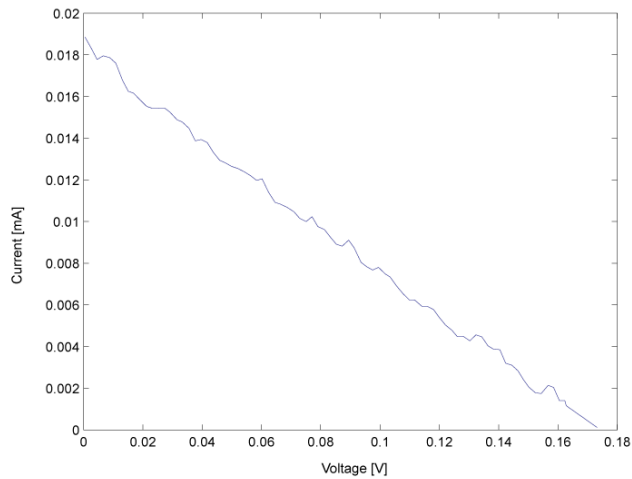


Figure 11.2: I-V characteristic of sample A2 for measurements obtained by the use of an artificial light source resembling the solar spectrum.

from using screen printing as phosphorus application technique did not reveal any improvement for the cell to act as a rectifying diode.

To resolve the problem of not gaining a proper diode behavior, a quartz tube furnace was used in the drive-in process to enable manipulation of the atmosphere. This allowed for the use of a controlled dry air atmosphere which reduced the oxide layer formation at the substrate surface in contrary to the drive-in process using the carbolithe furnace, where the substrates were in a non-dry air atmosphere. The altering of the particular atmosphere, lies in the composition of the phosphorus dopant. By conferring with the semiconductor-group in Aarhus, the drive-in temperature was increased to 1000°C due to a more suitable diffusion profile. The concentration of the HF acid was also increased from 1% to 10% to ensure complete removal of the oxide layer formed during drive-in.

A general issue when applying the phosphorus paste onto the substrates, both in the spin-on and screen printing techniques, was the accumulation of paste along the edges of the samples. This could result in a low shunt resistance and possibly a short circuit between the contacts as the n-doped region would directly connect the front- and backside contacts. To prevent the paste from accumulating at edges of the samples, tape was placed along the sides of the samples covering app. 1mm of the substrate area from the edge before screen printing the phosphorus.

The initiatives discussed were implemented in the fabrication of the C-series. Figure 11.3 shows the diode characteristics measurement of sample C2, which is seen to exhibit no diode behavior and instead resemble a resistor.

At this stage the sheet resistance measuring method from section 10.1 was set

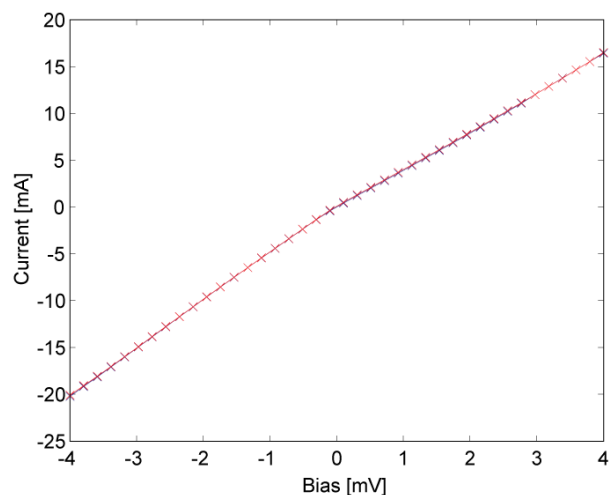


Figure 11.3: Diode characteristic of sample C2.

up and utilized. The aim was to investigate the diffusion of phosphorus into the substrates, as the sheet resistance gives a measure of the dopant concentration level and the position of the pn-junction. If the pn-junction lies too close to the substrate surface metal defects from the front contact can act as recombination centres and thus reduce the net current generation. Sample D was fabricated at the same conditions as sample B2 in order to measure the sheet resistance. The sheet resistance

of sample D was measured to $44.01\Omega/\text{sq}$. As a sheet resistance of app. $25\Omega/\text{sq}$ is sought, the high value indicates drive-in issues. This sheet resistance value was sought by conferring with the semiconductor group in Aarhus.

The HF acid aims to remove the oxide layer formed during the drive-in process. If an oxide layer remains at the surface it will isolate the contacts from the solar cell. When all oxide has been removed the hydrogen from the acid forms covalent bonds to the silicon atoms at the surface. This leaves the surface highly hydrophobic. Sample D was observed to not exhibit a hydrophobic surface and therefore it was assumed that too much phosphorus had not contributed to the drive-in process and thus prevented the hydrogen to access the surface silicon atoms. This excess amount of phosphorus paste could also have an influence on the sheet resistance measurement.

Samples G1-G4 were fabricated by increasing drive-in times of 3, 5, 7, and 9min of identical phosphorus paste thickness to investigate the hydrophobicity of the samples. G1 and G2 did not show any hydrophobic characteristics, while G3 and G4 with a drive-in time of 7 and 9min, respectively, exhibited hydrophobic surfaces. The diode characteristics of sample G1 and G4 is shown in figure 11.4 and 11.5. Sample G1 and G4 show some diode behavior, however, the lack of rectification can be explained by the influence of a Schottky diode between metal and semiconductor. If this is the case the hydrophobicity of sample G4 has not contributed to a better contact between the metal and semiconductor. The variation of the diode behavior of sample G4 compared to G1 must then lie in the different drive-in times.

Comparing sample G1 and C2 fabricated by the same specifications, it is seen

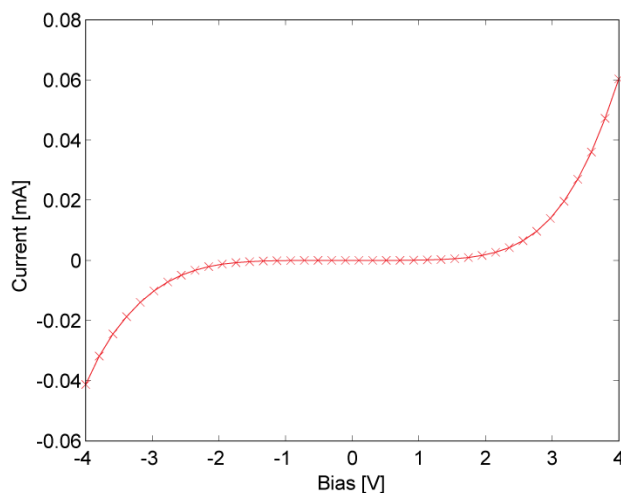


Figure 11.4: Diode characteristic of sample G1.

that the I-V curves show no resemblance. Thus the deviation was assumed to lie in the placement of the samples in the QTF tubes as the placement method was non-consistent.

The drive-in procedure using the QTF was executed by placing the substrates in an inner tube which is slid into the main tube of the furnace. When inserted into the main tube, with a temperature of 1000°C , the inner tube will obtain the tempe-

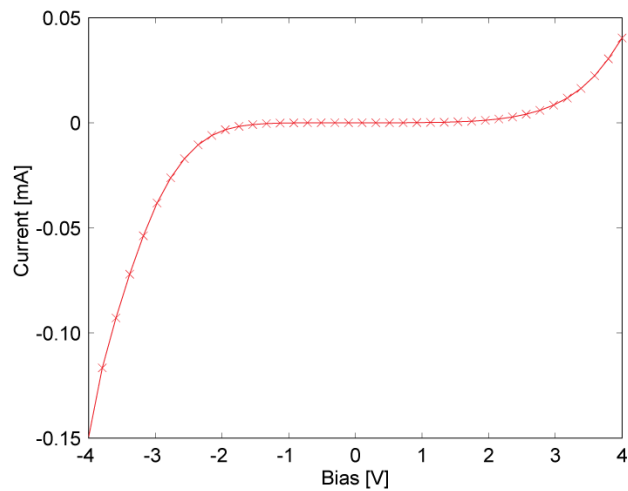


Figure 11.5: Diode characteristic of sample G4.

perature of the surroundings over time and transfer its heat to the substrate. Therefore the temperature of the samples during drive-in was non-controllable and not the prefixed temperature of 1000°C . As a consequence the procedure of the drive-in in the QTF was changed. The inner tube was inserted into the main tube to achieve the desired temperature before drive-in and the substrate was then placed directly into the inner tube to obtain the prefixed temperature of 1000°C .

Samples H1-H3 were fabricated with the altered placement technique by which all samples exhibited hydrophobic surfaces. However, this had no effect on the diode characteristics, which showed either poor diode characteristics or resistor resemblance. To this point front and backside contacts were fabricated using the photolithography method described in section 9.2. The hydrophobicity of the surfaces obtained complicated the spin-on of the photo resist as it did not cover the surface area completely. To resolve this problem a metal mask was fabricated as shown in figure 9.6 which eliminated the use of photo resist and the photolithography method.

Samples J1 and J2 were fabricated with two different phosphorus dopant pastes; a phosphorus spin-on dopant at sample J1 and the screen printing paste used in the A to I series at sample J2. The fabrication specifications were identical for comparing the effect of the two different dopants. An efficiency increase of app. 50% is seen for sample J1 compared to J2 by using the phosphorus spin-on dopant. The diode I-V curves, however, did not resemble diode characteristics. It was seen on sample J2, fabricated with the screen printing method, that an uneven paste thickness was deposited on the wafer surface and thus hydrophilic areas on the surface were present. To achieve a more uniform layer of the phosphorus screen printing paste the spin-on method was utilized as application method.

11.2 Sheet resistance vs. paste thickness

A series of samples with different phosphorus paste thickness were fabricated to examine the influence of increasing paste thickness to the sheet resistance. Phosphorus paste was spun on at various spin velocities onto a p-type silicon substrate and drive-in was executed, cf. the procedure in chapter 9. After oxide removal in HF acid the sheet resistance of the n-doped silicon layer was measured as mentioned in section 10.1. The results are shown in table 11.1.

It is seen from table 11.1 that an increase in paste thickness from 2.7 to 9 μm

Sample	Thickness	Drive-in time	R_{sheet}	Hydrofobicity
1	9.0 μm	1.5min	23.25 Ω/sq	semi-hydrofobic
2	7.0 μm	1.5min	23.57 Ω/sq	semi-hydrofobic
3	5.1 μm	1.5min	21.53 Ω/sq	hydrofobic
4	3.4 μm	1.5min	23.80 Ω/sq	hydrofobic
5	2.7 μm	1.5min	22.44 Ω/sq	hydrofobic
6	9.0 μm	3min	16.77 Ω/sq	hydrofobic
7	7.0 μm	3min	16.95 Ω/sq	hydrofobic
8	5.1 μm	3min	17.09 Ω/sq	hydrofobic
9	3.4 μm	3min	16.95 Ω/sq	hydrofobic
10	2.7 μm	3min	17.59 Ω/sq	hydrofobic

Table 11.1: Measurements of the sheet resistance of samples with different paste thickness and diffusion time.

does not alter the sheet resistance of the n-doped silicon layer. Hence, if the amount of phosphorus paste on the surface is not fully consumed, only the drive-in time and temperature have an influence on the sheet resistance and thus the dopant concentration and junction depth. A decreased drive-in time gives rise to an increased sheet resistance revealing a lowering of dopant concentration or a shallow junction or both combined. This is in accordance with the theory outlined in section 4.1.

11.3 Contact annealing

Generally the output current of the fabricated solar cells was low which results in a low efficiency as displayed in the tables in appendix B. To enhance the electrical connection between the solar cell and the contacts four samples M1, M2, N1, and N2 were fabricated. M1 and N1 together with M2 and N2 were fabricated under same conditions for the purpose of contact annealing the N series. The N series was annealed in a QTF at 400 $^{\circ}\text{C}$ with an inert atmosphere of argon flow for 30min. The diode characteristics of M2 and N2 are shown in figure 11.6 and 11.7, respectively.

It is seen at sample N2 that a smaller bias is required to force a current compared to the I-V curve of sample M2. The annealing procedure has therefore contributed to a better contact between the semiconductor and the metal and thus a lowering of the series resistance has occurred. This is also seen in the improvement in efficiency

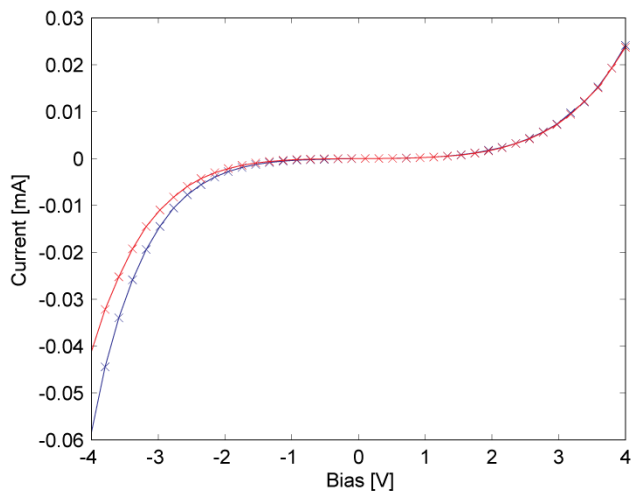


Figure 11.6: Diode characteristic of sample M2.

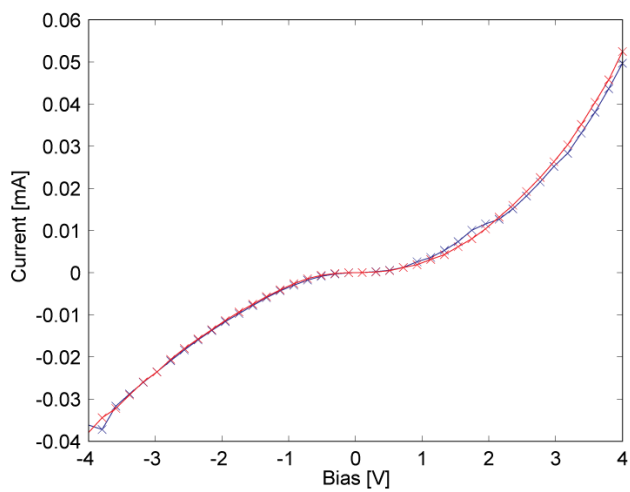


Figure 11.7: Diode characteristic of sample N2, for which contacts have been annealed.

from 0.81% to 2.42%. Though a better contact between the semiconductor and the metal has been achieved a deterioration of the rectification of the diode has occurred. Thus the contact annealing has lowered the shunt resistance. This can be explained by diffusion of remaining aluminum at the edges of the wafer, after polishing with sand paper near the pn-junction region, thus creating metallic defects as the aluminum can have gained better contact similar to the front and backside contacts.

A second scenario could be that the Schottky barrier, formed in the interface between the metal and the semiconductor, has been included as subject of measurement for sample M2. By annealing the contacts the Schottky barrier may have been reduced and thus the diode characteristic of the actual solar cell is more influential.

11.4 RIE-etching

To resolve the consistent issue of an insufficient shunt resistance and a poor acting diode behavior, the contact at the n-doped layer was sought to be completely isolated from the p-doped layer contact by scaling up the dimension of the wafer surface. The distance from the edge of the front contact to the edge of the n-doped layer is hence increased, see figure 11.8.

Furthermore, RIE-etching was utilized to separate the backside contact from

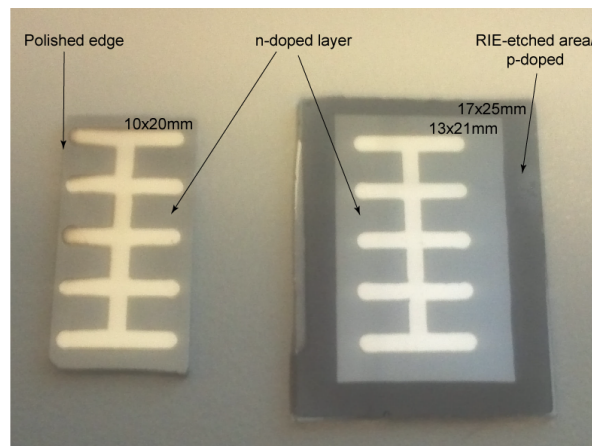


Figure 11.8: Dimensions of the solar cell surface scaled to increase the distance from the edge of the front contact to the edge of the n-doped layer.

the n-doped layer as outlined in section 9.2. These precautions aim to prevent current leakage through the edges to enhance the shunt resistance. Samples O1-O4 were fabricated with spin-on screen printing paste and O5-O8 using regular spin-on dopant. Samples O3-O6 were fabricated using a silicon substrate with a resistivity of 15-20 Ω .cm and O1, O2, O7, and O8 are fabricated using a silicon substrate of 1.8-4.5 Ω .cm. In addition the drive-in time was varied between 2 and 3min. All samples in the O series have been contact annealed in a RTA furnace at 400°C for 5min in a oxygen free atmosphere to avoid oxidation. The diode characteristic of the solar cell (O2) with the highest efficiency using the spin-on application method

with screen printing paste is shown in figure 11.9, where rectifying behavior is observed. The efficiency is calculated to 4.05%, which is several multiples of the gained efficiencies from the samples A-L.

The RIE-etching process is seen to properly prohibit the current from leaking

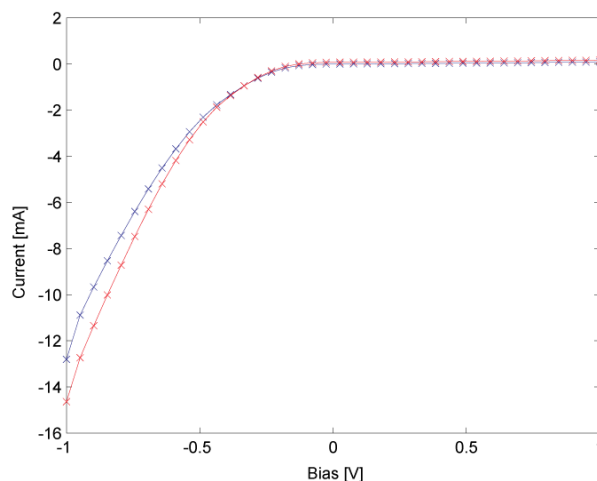


Figure 11.9: Diode characteristic of sample O2.

around the edges and thus rectification is achieved. This property is consistent for all samples O1-O8. The diode characteristic of the solar cell with the highest gained efficiency of 5.1% for sample O8 is depicted in figure 11.10 and furthermore the I-V curve from the efficiency measurement of sample O7 and O8 is depicted in figure 11.11.

Generally a larger current is gained for all solar cells fabricated in the O-series

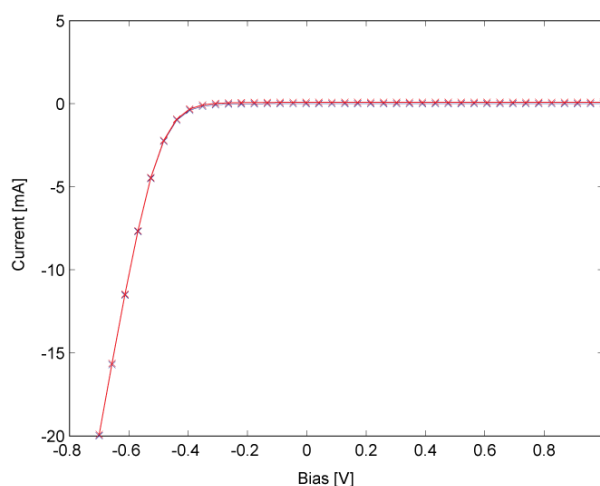
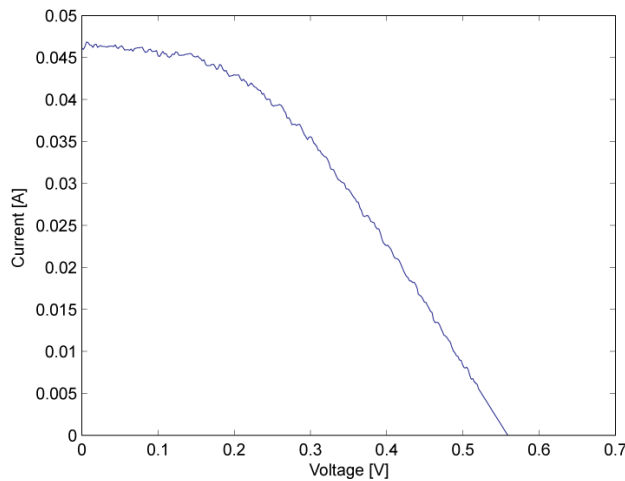


Figure 11.10: Diode characteristic of sample O8.

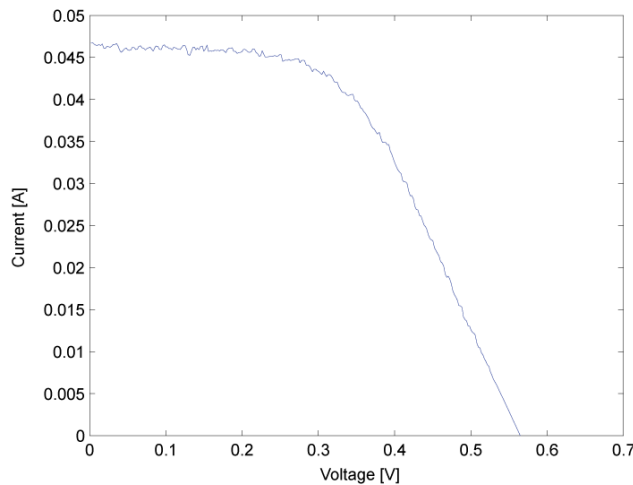
using RIE-etching compared to the A- to L-series. This is a direct consequence of the contact separation, as the charge separated in the pn-junction is less likely to leak through the edges. As discussed in section 8.2.3 the slope of the I-V curve,

before the break towards open circuit voltage, in figure 11.11(b) is given from the shunt resistance. The shunt resistance of sample O8 is calculated to 299Ω and the series resistance given by the slope of the curve towards open circuit voltage, is calculated to be 5.13Ω . The open circuit voltage was measured to 0.56V and the short circuit current to 46.6mA for sample O8.

The wafers fabricated using $15\text{-}20\Omega\cdot\text{cm}$ substrates show a general lower effi-



(a) Sample O7.



(b) Sample O8.

Figure 11.11: I-V characteristic of sample O7 and O8 for measurements obtained by the use of an artificial light source resembling the solar spectrum.

ciency than of the solar cells fabricated using $1.8\text{-}4.5\Omega\cdot\text{cm}$ substrates. This can be correlated with the fact that the concentration of free carriers in this substrate is of a lower value and thus create a weaker built-in electric field within the pn-junction that would lower the separation of charge carriers generated.

Though a proper shunt resistance was obtained for sample O8, the series resistance is sought to be lowered to gain higher currents for voltages closer to the

open circuit value and thereby an increase in efficiency. An enhancement of the metal-semiconductor contact is focused upon together with a manipulation of the pn-junction depth. As the distance from the front contact to the pn-junction is much greater than the distance from the backside contact to the junction, metal atoms are more likely to diffuse from the front contact through the pn-junction for high annealing times and temperatures and thereby short circuit the contacts. This allows for the diffusion of metal atoms from the backside contact at a much larger extend. Therefore the annealing process of the backside contact was conducted before applying the front contact to investigate a possible improvement of the current. Furthermore to alter the pn-junction depth the drive-in time is lowered as more light is absorbed closer to the silicon surface according to section 7.2.1.

Samples P1-P4 have been fabricated similarly to O8, but the backside contact has been annealed at 600°C in a QTF at inert argon flow prior to front contact application and annealing at 400°C. The drive-in time has been varied between 0.5-3min, see table B.2. The I-V characteristics of sample P1 is shown in figure 11.12 and sample P2-P4 are shown in figure 11.13. Sample P1 which has been fabricated at a drive-in time of 0.5min shows poor characteristics of a solar cell, seen by the resemblance of a resistor. This was expected as the pn-junction has established too close to the surface and front contact.

An efficiency increase is seen as the drive-in time increases, which is in coher-

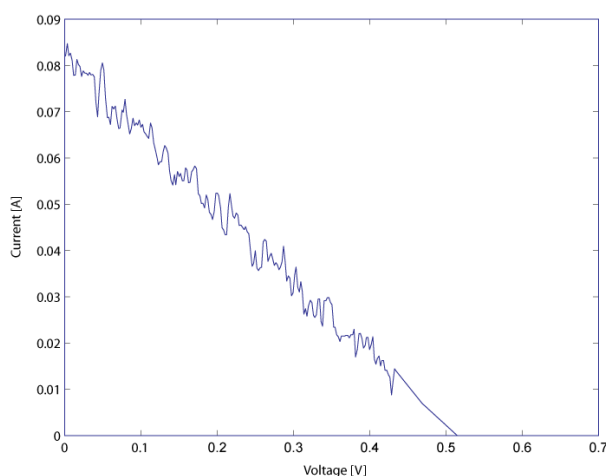
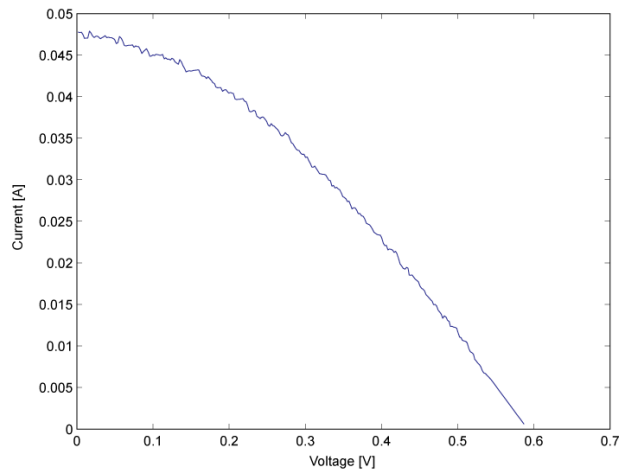


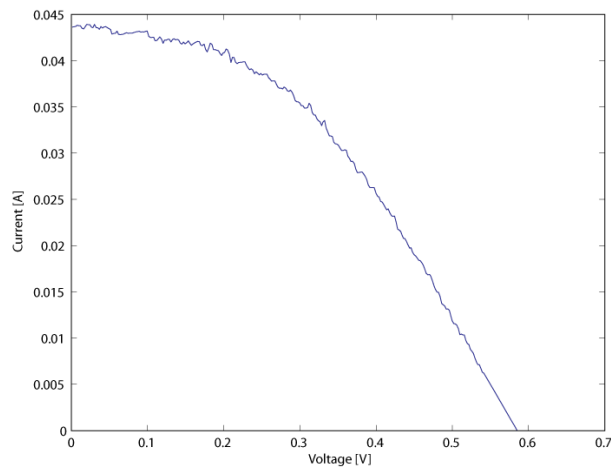
Figure 11.12: I-V characteristic of sample P1 for measurements obtained by the use of an artificial light source resembling the solar spectrum.

ence with the results for O7 and O8. If the I-V curve of sample O8 is compared with sample P4 a slight reduction in the series resistance from 5.12Ω for sample O8 to 5.07Ω for sample P4 is observed. However, the shunt resistance has decreased from 299Ω to 151Ω, respectively. In both the O7-P3 and the O8-P4 comparison a decrease in shunt resistance is observed for the samples with pre-annealed backside contacts. The series resistance was generally not influenced by the pre-annealing of the backside contacts.

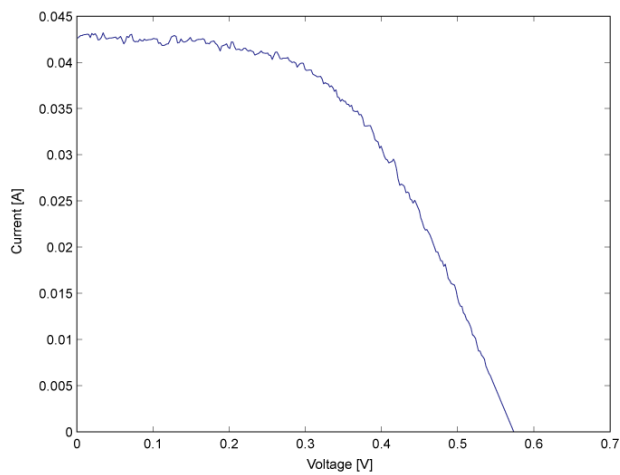
The cell efficiency was not improved due to pre-annealing of the backside contact, on the contrary it was lowered mainly due to a decrease in shunt resistance and



(a) Sample P2.



(b) Sample P3.



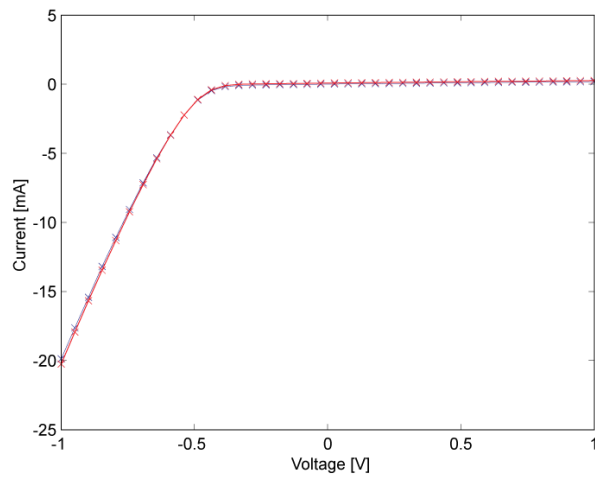
(c) Sample P4.

Figure 11.13: I-V characteristic of sample P2, P3, and P4 with increasing drive-in time, for measurements obtained by the use of an artificial light source resembling the solar spectrum.

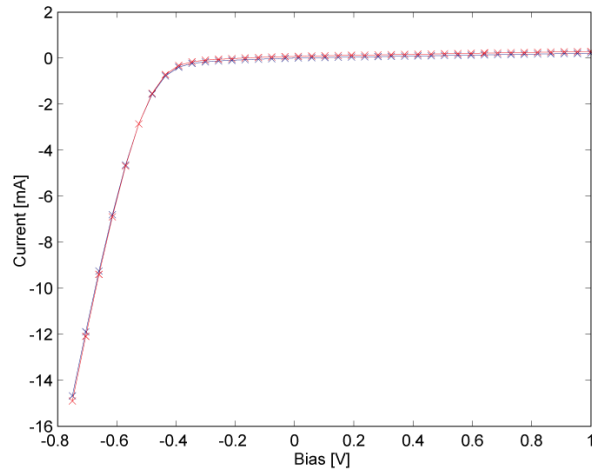
a lower short circuit current. A reason for this decrease in shunt resistance could be that the annealing of the aluminum backside contact has allowed some aluminum to diffuse to the pn-interface at the surface allowing current to leak through the edges despite the physical distance of at least 1mm due to RIE-etching.

To examine the effect of annealing the front contact after backside contact annealing, the diode characteristics of sample P1-P4 were measured prior to and after the contact annealing at 400°C. The diode characteristics prior to and after this annealing process is shown for sample P4 in figure 11.14. As expected the series resistance decreases after annealing, seen by comparing the slope of the I-V curves. This is in contrary to the fact that the isolated backside contact annealing did not exhibit this effect. As the backside contact annealing at 600°C was conducted in a QTF, which has a low cool down rate, the inner tube containing the sample was partly extracted from the QTF after the annealing time had expired, to not over expose the contact. At this position of the inner tube, a flow of argon was still present, though decreased, compared to that prior to extraction. This could have allowed for air to access the sample building up a thin oxide layer. The measurement displayed in figure 11.14(a) is conducted with the front contact deposited onto this oxide thin film. The oxide thin film would have a degrading effect on the contact between metal and semiconductor yielding a relatively high series resistance. However, as the front contact is annealed, metal atoms will diffuse through the oxide thin film and into the n-doped silicon establishing ohmic contact. This will decrease the series resistance as seen in figure 11.14(b).

Basic polycrystalline silicon based solar cells with a total area efficiency of app. 5% has been fabricated without the involvement of anti-reflecting coating. This is a reasonable result considering that commercial high efficiency solar cells have a conversion efficiency of about 22%, as outlined in chapter 1. The RIE-etching process in the fabrication was found to have a significant effect on the shunt resistance of the solar cells fabricated. This was one of the key reasons that an efficiency of 5% was achieved and showed to be a reliable fabrication method. A decrease in the solar cell series resistance was observed for solar cells with front contacts annealed at 400°C for five minutes in a RTA. However, the isolated annealing of the backside contact, at 600°C for five minutes in a QTF, did not exhibit the same positive effect as this resulted in a decrease in shunt resistance. Furthermore the thickness of phosphorus screen printing paste was shown not to affect the measured sheet resistance, and thereby the phosphorus concentration and junction depth.



(a) Diode characteristic of sample P4 before contact annealing.



(b) Diode characteristic of sample P4 after contact annealing.

Figure 11.14: Diode characteristic of sample P4 before and after front and back-side contact annealing. A decrease in series resistance is observed after annealing.

Chapter 12

Perspectives

Though the RIE-etching process proved to be a consistent process of securing a reasonable shunt resistance, the reliability of the entire fabrication method was not established, as a proper conversion efficiency was not achieved until late in the project period. According to this an expansion of the project seems natural. However, several directions are possible.

As described in chapter 1 the addition of metallic nanoparticles to a solar cell surface is considered to have an impact of the efficiency achieved. The metallic nanoparticles exhibit strong resonant absorption due to the excitation of localized surface plasmon (LSP) resonances. The metal to favour depends on the situation. Tin nanoparticles would be of great interest as tin is electrically neutral as a substitutional impurity in silicon if diffused into the crystal lattice. Tin has to be embedded in a SiO₂ film in order not to oxidize. Instead a more inert metal as gold or silver, exhibiting LSP resonances well into the visible regime, can be utilized.

From the surface of the solar cells, fabricated throughout this project, a fraction of the incident light is reflected. This is a loss mechanism for the photogeneration in the solar cell. Consequently, an antireflective coating could be applied to the solar cell surface to absorb some of the lost solar energy.

The ability of manipulating the pn-junction depth is of great importance as it allows for tuning the solar cell to produce electric energy from the absorption of a desired wavelength. This requires, however, the knowledge of the position of the junction. By means of secondary ion mass spectrometry (SIMS) the composition of the surface can be analyzed. This technique has the advantage of being able to detect elements present in the parts per billion range. As the phosphorous impurity concentration lies in the order of 10^{18}cm^{-3} , whereas the concentration of silicon atoms lies in the order of 10^{22}cm^{-3} , the sensitivity of this method is an useful feature.

Chapter 13

Conclusion

The main motive of this thesis is to examine methods of fabricating functional solar cells and means for enhancing their efficiency due to the environmental demanding of greener energy sources such as that from solar cells, as briefly discussed in chapter 1. This lead to the initiating problem statement: "How can a basic solar cell with rectifying diode behavior be fabricated, and how can the specific characteristics of the solar cell be enhanced?" Thus, in order to create a pn-junction within a p-doped silicon substrate, phosphorus was used as n-type dopant. The fabricated solar cells were characterized by measuring their sheet resistance, their diode behavior in the dark and under illumination, and their I-V characteristics when illuminated by an artificial sun. These characterization methods enabled the calculation of the efficiency for each individual cell fabricated.

Initially the dynamics of electron and holes plus the concept of impurities in semiconductor crystal lattices are described in chapter 3 to understand the concept of diffusion of a dopant into a substrate in chapter 4. Furthermore, semiconductor statistics are investigated to describe the pn-junction formation in a semiconducting material in chapter 6 and the metal-semiconductor interface is described for aluminum and silicon. Finally the transmittance of a range of wavelength has been calculated in chapter 7 for silicon, to give an estimate of an optimum absorption depth of the material.

In the fabrication process two methods of applying phosphorus to the silicon substrate, for the formation of a pn-junction, were utilized. Phosphorus screen printing paste was screen printed on using a mesh, shown in figure 9.3. Furthermore a spin-on phosphorus dopant was spun on the silicon substrates, and in addition, the screen print phosphorus dopant was also used in the spin-on method. To enhance the characteristics of the individual solar cells several means were taken into consideration to obtain rectifying diode behavior and to increase the photocurrent, this approach is described chronologically in the discussion in chapter 11.

Solar cells with rectifying diode behavior were obtained for both phosphorus dopants. The RIE-etching process, outlined in section 11.4, used to etch the sides of the solar cells was imperative to gain this behavior. A maximum efficiency of 5% was achieved for a fabricated polycrystallin silicon solar cell using spin-on phosphorus as dopant, sample O8 in table B.2. Using screen printing phosphorus paste

a maximum efficiency was achieved at 4%. An open circuit voltage of 0.56V and a short circuit current of 46.65mA were obtained for the solar cell with an efficiency of 5%. The diode characteristic of sample O8 is shown in figure 11.10 and its I-V characteristic is shown in figure 11.11(b).

Functional solar cells have been fabricated and by improving the fabrication methods their efficiency has been increased. An efficiency of 5% is reasonable, as no antireflective coating has been utilized, and a high efficiency for commercial solar cells lies at app. 22%.

To enhance the efficiency further of the fabricated solar cells anti reflective coating could be placed on the surface to harness more of the incoming radiation. The localized plasmon resonances of metallic nanoparticles could be utilized by introducing it to the surface to enhance the solar cell efficiency via their strong resonant absorption.

Bibliography

- [1] M. Balkanski and R. F. Wallis. *Semiconductor Physics and Applications*. OXFORD University Press, 2007.
- [2] Stephen A. Campbell. *Fabrication Engineering at the Micro- and Nanoscale*. Oxford University Press, 2008.
- [3] Mads Møgelmoose Kjeldsen et al. Tuning the plasmon resonance of metallic tin nanocrystals in si-based materials. *Applied Physics A*, 100(1):7, 2010.
- [4] Thomas W. Krygowski et al. A novel processing technology for high-efficiency silicon solar cells. *Journal of The Electrochemical Society*, 1999.
- [5] Inc. Filmetrics. Refractive index of silicon, si.
- [6] Charles Kittel. *Introduction to Solid State Physics 8th ed.* John Wiley & Sons, Inc., 2005. ISBN 0-471-41526-X.
- [7] Miles V. Klein and Thomas E. Furtak. *Optics*. John Wiley & Sons, 2 edition, 1986. ISBN: 0-471-87297-0.
- [8] Hans Lüth. *Solid Surfaces, Interfaces and Thin Films*. Springer, 5th ed. edition, 2010.
- [9] Jenny Nelson. *The Physics of Solar Cells*. Imperial College Press, 2003.
- [10] Endeas Oy. Quick sun, photovoltaic measurement systems, 2010.
- [11] Maria Berg Badstue Pedersen. Dansk solcelleforening: Husk potentialet i solceller, october 2010.
- [12] Argonne National Laboratory Renée M. Nault. Basic research needs for solar energy utilization. Technical report, U.S. Department of Energy, 2005, September.
- [13] Wikipedia. Kyoto protocol, 2011.
- [14] Wikipedia. World energy consumption, 2011.

Appendix A

Electromagnetic Respons

As electromagnetic radiation interacts with either a solid, a liquid, or a gas the interaction is described using the terms of absorption, dispersion, and scattering. The exposed material is perturbed by the incoming electromagnetic field and the process can involve either electronic states or vibrational states or both simultaneously. This can lead to transitions between states in the material e.g. an electron receives enough energy to excite from valence to the conduction band, as in the case for semi conductors. If the transition rate is calculated it becomes possible to determine the optical properties of consideration. This appendix presents a general formulation of the electromagnetic response of matter and lastly the response of a dielectric.[1, p. 228]

A.1 Maxwell's equations

The four well known equations describe the electrodynamics in the presence of matter and are formulated as follows;

$$\vec{\nabla} \cdot \vec{E} = \frac{\rho}{\epsilon_0}$$
$$\vec{\nabla} \times \vec{E} = -\mu_0 \frac{\partial \vec{H}}{\partial t} \quad (\text{A.1})$$

$$\vec{\nabla} \cdot \vec{H} = 0 \quad (\text{A.2})$$

$$\vec{\nabla} \times \vec{H} = \epsilon_0 \frac{\partial \vec{E}}{\partial t} + \vec{J}, \quad (\text{A.3})$$

where \vec{E} is the electric field, \vec{H} is the magnetic field, ρ is the electric charge density, and \vec{J} is the electric current density. ϵ_0 and μ_0 are the permittivity and the permeability respectively. If the material is magnetic one writes equation (A.1) and (A.2) as

$$\begin{aligned}\vec{\nabla} \times \vec{E} &= -\frac{\partial \vec{B}}{\partial t} \\ \vec{\nabla} \cdot \vec{B} &= 0,\end{aligned}$$

where \vec{B} is the magnetic induction. If the magnetization is introduced as \vec{M} , magnetic dipole moment per unit volume, and the magnetic permeability tensor $\bar{\bar{\mu}}$, the magnetic induction can be expressed as

$$\vec{B} = \mu_0(\vec{H} + \vec{M}) = \mu_0\bar{\bar{\mu}} \cdot \vec{H}. \quad (\text{A.4})$$

In addition the magnetization and magnetic field are related through,

$$\vec{M} = \bar{\bar{\chi}}_m \cdot \vec{H}, \quad (\text{A.5})$$

where $\bar{\bar{\chi}}_m$ is the magnetic susceptibility tensor. It can be deduced from equations (A.4) and (A.5) that $\bar{\bar{\mu}} = I + \bar{\bar{\chi}}_m$ is true. For nonmagnetic materials, $\bar{\bar{\chi}}_m = 0$ and $\vec{B} = \mu_0\vec{H}$.

In order to describe the interaction between the radiation field and an electrically polarizable medium one introduces the polarization vector \vec{P} , defined as the electrical dipole moment per unit volume, and the electrical displacement \vec{D} , which is related to \vec{E} and \vec{P} through

$$\vec{D} = \epsilon_0\vec{E} + \vec{P}. \quad (\text{A.6})$$

When a crystal is pertubated by an electrical field \vec{E} it becomes polarized due to an acquired electrical dipole moment, and in the linear limit, the response is

$$\vec{P} = \epsilon_0\bar{\bar{\chi}} \cdot \vec{E}, \quad (\text{A.7})$$

where $\bar{\bar{\chi}}$ is the dielectric susceptibility tensor. If (A.7) is substituted into (A.6) the displacement vector becomes

$$\vec{D} = \epsilon_0(I + \bar{\bar{\chi}}) \cdot \vec{E}.$$

The dielectric tensor is now introduced as $\bar{\bar{\epsilon}}$ by the relation

$$\bar{\bar{\epsilon}} = I + \bar{\bar{\chi}},$$

Thus the displacement field can be written as

$$\vec{D} = \epsilon_0\bar{\bar{\epsilon}} \cdot \vec{E}.$$

The dielectric tensor yields information about how the dielectric medium response to the presence of an electromagnetic field.

More generally the above mentioned fields are functions of both time t and position \vec{r} . In fact if the field quantities vary in time with a frequency ω the material parameters $\bar{\bar{\chi}}$, $\bar{\bar{\epsilon}}$, and $\bar{\bar{\mu}}$ also in general are functions of ω . However for brevity, it is assumed that the response is local meaning that the fields are evaluated at the same position \vec{r} .

A.1.1 Electromagnetic wave propagation in a conductive medium

The total electric current density, \vec{J}_t of a conducting material is related to the electric field \vec{E} through

$$\vec{J}_t = \tilde{\sigma}\vec{E},$$

assuming linear response due to the applied field. $\tilde{\sigma}$ is here the complex electrical conductivity.

In order to find the total electric current two contributions are needed. Firstly the steady state part due to motion of unbound charges and the latter due to the motion of time-dependent bound charges. The contribution from the bound part is the time derivative of the polarization vector, $\partial\vec{P}/\partial t$, and thus the sum from the two contribution to the current density can be written as

$$\vec{J} = \vec{J}_{cond} + \frac{\partial\vec{P}}{\partial t}. \quad (\text{A.8})$$

Here \vec{J}_{cond} is the current contribution from the unbound charges and is given by $\vec{J}_{cond} = \sigma\vec{E}$.

If equation (A.8) is substituted into equation (A.3) and utilizing equation (A.6) this yields

$$\vec{\nabla} \times \vec{H} = \frac{\partial\vec{D}}{\partial t} + \vec{J}_{cond} = \vec{J}_t. \quad (\text{A.9})$$

As a first approximation, when dealing with the optical properties of semiconductors, the steady current \vec{J}_{cond} from free carriers can be left out. Thus the time-dependent currents can be regarded only for simplicity. The current contribution then becomes

$$\vec{J} = \frac{\partial\vec{P}}{\partial t}, \quad (\text{A.10})$$

and as a consequence the curl of \vec{H} becomes

$$\vec{\nabla} \times \vec{H} = \frac{\partial\vec{D}}{\partial t}. \quad (\text{A.11})$$

In the following equation (A.11) is used instead of equations (A.3) and (A.9), that is, \vec{J}_{cond} is left out as an approximation.

To analyze an electrically neutral solid further another important property can be calculated by taking the divergence of equation (A.6) and utilizing $\vec{\nabla} \cdot \vec{E} = \rho/\epsilon_0$, hence

$$\vec{\nabla} \cdot \vec{D} = \rho + \vec{\nabla} \cdot \vec{P}. \quad (\text{A.12})$$

Now if equation (A.10) is substituted into the equation of continuity,

$$\frac{\partial\rho}{\partial t} + \vec{\nabla} \cdot \vec{J} = 0,$$

this yields

$$\rho = -\vec{\nabla} \cdot \vec{P}. \quad (\text{A.13})$$

Conclusively equation (A.13) is substituted into (A.12) yielding

$$\vec{\nabla} \cdot \vec{D} = 0. \quad (\text{A.14})$$

The derivation of the electrodynamic equations for an electrically neutral polarizable material is thus completed with the approximation of neglecting the steady contribution to the current, \vec{J}_{cond} .

The dispersion relation for an electromagnetic wave propagating in a dielectric medium is sought lastly in the following, assuming that the medium is nonmagnetic. Utilizing Maxwell's equations the procedure is to take the curl of equation (A.1) an utilizing equation (A.11)

$$\begin{aligned} \vec{\nabla} \times \vec{\nabla} \times \vec{E} &= \vec{\nabla} \times -\mu_0 \frac{\partial \vec{H}}{\partial t} \Leftrightarrow \\ &= -\mu_0 \frac{\partial}{\partial t} (\vec{\nabla} \times \vec{H}) \Leftrightarrow \\ &= -\mu_0 \frac{\partial^2 \vec{D}}{\partial t^2} \end{aligned} \quad (\text{A.15})$$

For brevity a linear response in the medium due to the electric field is assumed, thus

$$\vec{D} = \epsilon_0 \epsilon \vec{E}, \quad (\text{A.16})$$

with ϵ being some scalar dielectric constant. Equation (A.15) can hence be rewritten as

$$\vec{\nabla} \times \vec{\nabla} \times \vec{E} = -\frac{\epsilon}{c^2} \frac{\partial^2 \vec{D}}{\partial t^2}, \quad (\text{A.17})$$

where $c = (\mu_0 \epsilon_0)^{-1}$ is the speed of light in vacuum. The double rotor of \vec{E} is rewritten using a vector identity and (A.17) becomes

$$\vec{\nabla} (\vec{\nabla} \cdot \vec{E} - \nabla^2 \vec{E}) = -\frac{\epsilon}{c^2} \frac{\partial^2 \vec{D}}{\partial t^2}. \quad (\text{A.18})$$

Utilizing equations (A.14) and (A.16) the expression in equation (A.18) reduces to the well known wave equation

$$\nabla^2 \vec{E} = \frac{\epsilon}{c^2} \frac{\partial^2 \vec{E}}{\partial t^2}. \quad (\text{A.19})$$

To solve the wave equation a plane wave solution is sought of the form

$$\vec{E}(\vec{r}, t) = \vec{E}_0 e^{i(\vec{k} \cdot \vec{r} - \omega t)}, \quad (\text{A.20})$$

where \vec{E}_0 is the amplitude of the electric field, \vec{k} is the wave vector, and ω is the frequency. Substituting (A.20) into equation (A.19) yields for a nontrivial solution:

$$\begin{aligned}\nabla^2 \vec{E}_0 e^{i(\vec{k}\cdot\vec{r}-\omega t)} &= \frac{\epsilon}{c^2} \frac{\partial^2 \vec{E}_0 e^{i(\vec{k}\cdot\vec{r}-\omega t)}}{\partial t^2} \Leftrightarrow \\ \vec{E}_0 k^2 e^{i(\vec{k}\cdot\vec{r}-\omega t)} &= \vec{E}_0 \frac{\epsilon}{c^2} \omega^2 e^{i(\vec{k}\cdot\vec{r}-\omega t)} \Leftrightarrow \\ c^2 k^2 &= \omega^2 \epsilon(\omega),\end{aligned}\tag{A.21}$$

which is the dispersion relation for electromagnetic waves in the dielectric medium [1, p. 228-231].

Appendix B

Specifics of Fabricated Solar Cells

Sample	Phosphorous	Drive-in	HF	Sheetres.	Efficiency
A1	sosp 1k RPM	Carb. 950°C/1.5min	1%/0.5min		
A2	sosp 1k RPM	Carb. 950°C/3min	1%/0.5min		
A3	sosp 2k RPM	Carb. 950°C/1.5min	1%/0.5min		
A4	sosp 2k RPM	Carb. 950°C/3min	1%/0.5min		
B1	sp	Carb. 950°C/1.5min	1%/0.5min		
B2	sp	Carb. 950°C/3min	1%/0.5min		
B3	sp	Carb. 950°C/1.5min	1%/0.5min		
B4	sp	Carb. 950°C/3min	1%/0.5min		
C1	sp	QTF 1000°C/1.5min*	10%/2min		0.045%
C2	sp	QTF 1000°C/3min*	10%/2min		0.024%
D	sp	QTF 1000°C/3min*	10%/2min	44.01Ω/sq	0.37%
E	Error				
F1	Error				
F2	Error				
G1	sp	QTF 1000°C/3min*	10%/2min	17.4Ω/sq	0.092%
G2	sp	QTF 1000°C/5min*	10%/2min	13.55Ω/sq	0.23%
G3	sp	QTF 1000°C/7min*	10%/2min	12.7Ω/sq	0.144%
G4	sp	QTF 1000°C/9min*	10%/2min	11.24Ω/sq	0.197%
H1	sp	QTF 1000°C/1min	10%/2min	20.53Ω/sq	0.177%
H2	sp	QTF 1000°C/3min	10%/2min	12.1Ω/sq	0.179%
H3	sp	QTF 1000°C/5min	10%/2min	9.6Ω/sq	0.21%
I	sp	QTF 1000°C/3min	10%/2min	13.64Ω/sq	0.33%

Table B.1: Specifications for each single solar cell fabricated. sp: screen print, so: spin-on, sosp: spin-on using phosphorus screen-printing paste, RTA: Rapid Thermal Annealer, QTF: Quartz Tube Furnace. All samples fabricated with phosphorus screen-printing paste have been heated on a hot plate for 15 minutes at 150°C after phosphorus application. Samples fabricated with spin-on phosphorus have been heated for one minute at 200°C. (*) The drive-in temperature of the samples was not 1000°C, as the inner tube was not preheated with the main tube.

Sample	Phosphorous	Annealing	HF	Sheetres.	Efficiency
J1	so-5k rmp	QTF 1000°C/3min	10%/2min	27.55Ω/sq	0.59%
J2	sp	QTF 1000°C/3min	10%/2min	17.9Ω/sq	0.4%
K1	sp	QTF 1050°C/2min	10%/2min	10.7Ω/sq	0.2%
K2	sp	QTF 1050°C/4min	10%/2min	7.75Ω/sq	0.09%
K3	sp	QTF 1050°C/6min	10%/2min	6.3Ω/sq	0.09%
L1	sp	QTF 1000°C/3min	10%/2min	18.76Ω/sq	0.13%
L2	sp	QTF 1000°C/5min	10%/2min	16.63Ω/sq	0.17%
M1	sosp-2k rmp	QTF 1000°C/1.5min	10%/2min	21.48Ω/sq	0.23%
M2	sosp-2k rmp	QTF 1000°C/3min	10%/2min	14.9Ω/sq	0.34%
N1	sosp-2k rmp	QTF 1000°C/1.5min	10%/2min	24.25Ω/sq	0.8%
N2	sosp-2k rmp	QTF 1000°C/3min	10%/2min	15.86Ω/sq	2.42%
O1	sosp-2k rmp	QTF 1000°C/2min	10%/2min	18.9Ω/sq	1.98%
O2	sosp-2k rmp	QTF 1000°C/3min	10%/2min	15.5Ω/sq	4.05%
O3**	sosp-2k rmp	QTF 1000°C/2min	10%/2min	19.94Ω/sq	0.18%
O4**	sosp-2k rmp	QTF 1000°C/3min	10%/2min	15.9Ω/sq	0.52%
O5**	so-2k rmp	QTF 1000°C/2min	10%/2min	22.8Ω/sq	0.60%
O6**	so-2k rmp	QTF 1000°C/3min	10%/2min	20.44Ω/sq	2.52%
O7	so-2k rmp	QTF 1000°C/2min	10%/2min	19.58Ω/sq	3.88%
O8	so-2k rmp	QTF 1000°C/3min	10%/2min	24.56Ω/sq	5.1%
P1***	so-2k rmp	QTF 1000°C/0.5min	10%/2min	434.98Ω/sq	0.43%
P2***	so-2k rmp	QTF 1000°C/1min	10%/2min	39.84Ω/sq	3.62%
P3***	so-2k rmp	QTF 1000°C/2min	10%/2min	21.71Ω/sq	4.01%
P4***	so-2k rmp	QTF 1000°C/3min	10%/2min	16.41Ω/sq	4.65%

Table B.2: Specifications for each single solar cell fabricated. sp: screen print, so: spin-on, sosp: spin-on using phosphorus screen-printing paste, RTA: Rapid Thermal Annealer, QTF: Quartz Tube Furnace. All samples fabricated with phosphorus screen-printing paste have been heated on a hot plate for 15 minutes at 150°C after phosphorus application. Samples fabricated with spin-on phosphorus have been heated for one minute at 200°C. (**) Substrate of resistivity at 15-20Ω/sq was utilized. (***) Backside contact has been annealed at 600°C for 5min prior to front contact application.